5-2014

Chemical Fragmentation and Properties of Bulk Graphite and Inorganic Graphite Analogs Produced for Large-Scale Applications in Polymer Composites

Vikram Kumar Srivastava
University of Tennessee - Knoxville, vsrivast@utk.edu

To the Graduate Council:

I am submitting herewith a dissertation written by Vikram Kumar Srivastava entitled "Chemical Fragmentation and Properties of Bulk Graphite and Inorganic Graphite Analogs Produced for Large-Scale Applications in Polymer Composites." I have examined the final electronic copy of this dissertation for form and content and recommend that it be accepted in partial fulfillment of the requirements for the degree of Doctor of Philosophy, with a major in Chemistry.

Jimmy W. Mays, Major Professor

We have read this dissertation and recommend its acceptance:

Gajanan S. Bhat, Alexei P. Sokolov, George K. Schweitzer

Accepted for the Council:
Dixie L. Thompson

Vice Provost and Dean of the Graduate School

(Original signatures are on file with official student records.)

Chemical Fragmentation and Properties of Bulk Graphite and Inorganic Graphite Analogs Produced for Large-Scale Applications in Polymer Composites

A Dissertation Presented for the
Doctor of Philosophy
Degree
The University of Tennessee, Knoxville

Vikram Kumar Srivastava
May 2014

DEDICATION

This work is dedicated to my father, Dr. Vinai K. Srivastava, Ph.D., my mother Archana Srivastava, and my sisters, Divya Srivastava and Dr. Jaya Srivastava, Ph.D. for their support and encouragement. Also, I appreciate all my friends, teammates, and coworkers who have put up with me through the years.

"It's a small world, but I wouldn't want to paint it." – Steven Wright

ACKNOWLEDGEMENTS

The work presented in this dissertation would not have been possible without the technical guidance provided by both Professor Jimmy W. Mays and Professor Gajanan S. Bhat. I am extremely grateful to Dr. Ronald A. Quinlan and Dr. Alexander L. Agapov for their contributions to this work. I am also grateful for the help provided by other collaborators, Dr. Alexander Kisliuk, Mrs. Beth L. Armstrong, Mr. John J. Henry, Ms. Kimberly Nelson, and Mr. Eddy Duranty. I would also like to thank Professor Alexei P. Sokolov for his help with collaborative efforts. I thank Dr. Josh Fogle and Mr. Thomas Malmgren for their help with this project. I thank Dr. George Schweitzer for his feedback and comments regarding this dissertation. I appreciate the laboratory assistance and helpful discussions with my fellow group members, both past and present. I thank Adam Imel for his helpful discussions and similar skepticism regarding the literature and “amazing” aspects of nanomaterials. I am grateful to Art Pratt, Shannon Marshall, Gail Cox, Sherri Dugger, Beverly Adams Rosenbalm, Jessica VanBrunt, Melissa Walker, Marilyn Ownby, Jill Bodenheimer, Susan McGill, and Rhonda Wallace for their work behind the scenes. Finally, I thank the Office of Naval Research for funding this work (Award # N00014-10-1-0393).

ABSTRACT

The inherent nature of nanomaterials is not well understood, and production of polymer nanocomposites suitable for commercialization is still in its infancy. Polymer nanocomposites have displayed enhanced mechanical, thermal, electrical, and lubricating properties, which are dependent upon nanomaterial characteristics and dispersion. Chemical functionalization of nanomaterials to increase dispersion in various polymer matrices has been shown to further enhance properties. However specific understanding of the chemical and structural properties of modified nanomaterials and commercial scalability is rarely addressed. In this dissertation, we present the chemical fragmentation of 3-D layered hexagonal powders to generate large quantities of exfoliated and edge functionalized materials for dispersion in various polymer matrices.

Commercial precursor powders of 3-D hexagonal layered graphite, multi-layered graphene, molybdenum sulfide, and boron nitride were liquid-exfoliated using ultrasonication under various conditions to prepare large quantities of exfoliated materials. This dissertation focuses on the chemical exfoliation of these materials and the subsequent detailed chemical and structural material characterization. Furthermore understanding of the role of edge oxidation during the exfoliation process was studied, and the effects on the macroscopic properties were determined. Characteristic conductivities of graphite and graphene were greatly decreased, implying chemical and/or physical quenching

of electrons. Solution characteristics were studied and solution blending with polymers was performed to produce composites. Thermal characterization of the composites demonstrated poor interaction between filler and nonpolar polymers like polystyrene (PS) and poly(cyclohexadiene) (PCHD).

Considering the significance of solution characteristics for determining suitable polymer matrices and the effects on properties, a major part of this dissertation focuses on the colloidal behavior of the fragmented materials. Furthermore given the dispersion characteristics of the restacked materials, solution blending was used to generate composites, and the resulting effects on the macroscopic properties are reported. The addition of sodium bisulfite (SBS) during fragmentation of molybdenum disulfide (MoS_2) sheets appeared to generate a multiphase material, possibly from ion intercalation. The photoluminescence and lubricity of fragmented MoS_2 particles in aqueous dispersions and poly(ethylene glycol) (PEG) solutions suggested a means to produce tailored particles, desirable for applications in coatings or slurries.

TABLE OF CONTENTS

LIST OF TABLES

LIST OF FIGURES

INTRODUCTION

Historical Background, Production and Properties of 3-D Graphite and Inorganic Graphite Analogs

Production and Properties of Graphite and Graphene

Since the early 1900s, fundamental investigations were performed in order to determine the properties of three dimensional (3-D) layered hexagonal carbon, known as graphite. Graphite exhibits desirable properties including electrical conductivity (~1-10 S/cm), thermal conductivity (~100-500 W/m·K), and elastic modulus (~500-600 GPa).[1] The manufacturing of artificial graphite, reported in 1908, using silicon carbide highlighted the industrial viability of graphite.[2] A few years later, the detailed colloidal behavior of graphite was reported, demonstrating the characteristics of suspended graphite particles.[3] Further advances demonstrated methods to tailor growth of graphite to produce materials with unique and excellent material properties.[4, 5] The contributions of structural and chemical integrity on the properties of graphite were considered significant given the preferred orientation of synthesized graphite generating “ripples” on the surface.[6] As demand for new, tailored materials continue to rise, graphite has continued to be at the forefront of materials based research.

The monolayer two-dimensional (2-D) form of graphite, known as graphene, is stable at room temperature and has significantly improved electrical conductivity, thermal conductivity (~5,000 W/ m·K) and elastic modulus (≈1 TPa).[7, 8] Strong covalent bonding and van Der Waals interactions between layers in layered graphite sheets has inhibited isolation of monolayer material The

differences in properties between graphene and graphite (Figure 1.1) simply arise from the structural aspects, as increased layering generates an offset AB basal plane stacking order. This leads to increased probability of structural defects. Using chemical vapor deposition (CVD), large-area graphene sheets were prepared synthetically by feeding dilute hydrocarbon gas over a Ni substrate.[9] This method however requires specific equipment and reagents, but progress towards incorporating other carbon feedstocks was made.[10] Quite recently, a simple process was used to produce atomically thinner, few-layered graphene and exhibited behavior characteristic of two-dimensional (2-D) semimetals[11] which spurred further research to produce 2-D monolayer graphene. This isolation of monolayer graphene from bulk graphite[12] was considered monumental, further emphasized by the awarding of the Noble prize to Andre Geim and Konstantin Novoselov for this discovery. Using their "Scotch-tape exfoliation method", they demonstrated the ability to obtain 2-D monolayers of graphene and structural analogs (referred to as "inorganic graphene analogs" [13-15] or "graphene mimics"[16]) from 3-D bulk crystals.[17] However, a limitation of this method arises from the difficulty to produce large quantities of monolayer graphene.[12] As a result, the desired quality and/or quantity of graphene and the corresponding monolayer mimics are dependent upon the applications of the materials.

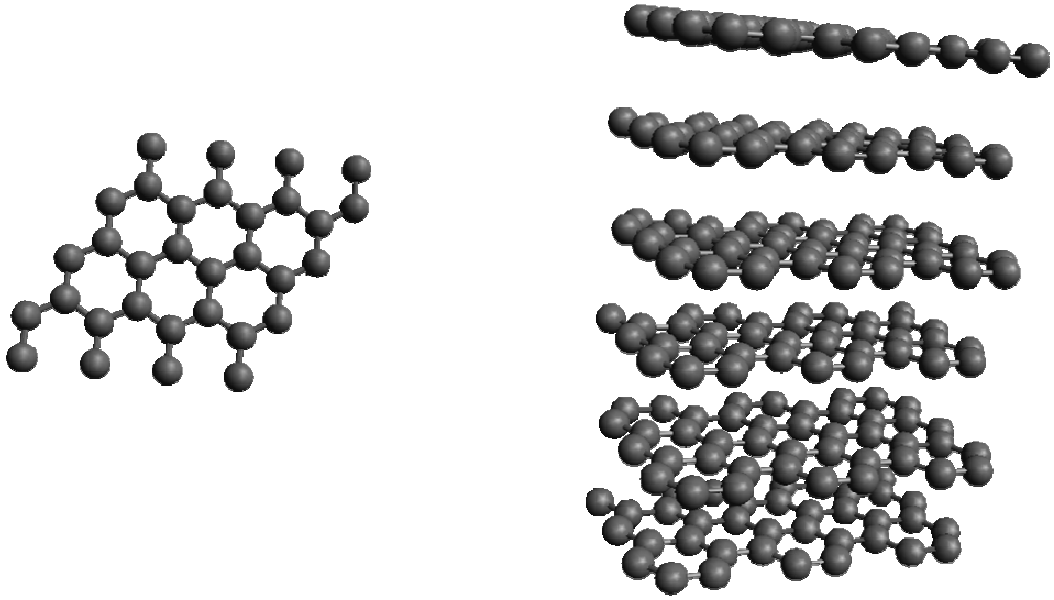

Figure 1. Structures of graphene and (AB) graphite

Production and Properties of Hexagonal Boron Nitride (h-BN) and Monolayer h-BN

Similarly, inorganic graphite analogs (IGAs) have emerged due to the excellent and unique properties of these materials. One such layered sheet IGA, known as hexagonal boron nitride (h-BN) (Figure 1.2), is considered the "white graphene" due to its physical appearance. Interestingly, the properties of nanoscale h-BN differ as it is electrically insulating (band gap ≈5-6 eV) and has superior resistance to chemical or thermal treatments, good lubricity, and successfully strengthened polymer composites and toughened ceramic-matrix composites.[18-21] The synthesis of h-BN, which is not found in nature, was first reported in 1842 by Balmain who using a reaction between molten boric acid and potassium cyanide to form the compound.[22] Analogous to synthetic graphite, the emergence of CVD as the primary technique to produce layered h-BN has increased attempts to isolate the 2-D form. The 2-D nanosheet was first observed for a "nanomesh" of boron nitride produced by the decomposition of borazine on a metallic surface,[23] and later mono- and few-layered sheets were isolated from single hexagonal crystals using a chemical-solution-derived method.[24] The reaction of boric acid and urea to generate h-BN was shown to control the number of layers successfully.[25] Mechanical exfoliation of bulk h-BN using wet-ball milling with benzyl benzoate as the wetting agent[26] produced "peeling" nanosheets and chemical exfoliation using a Lewis base permitted the isolation of 2-D sheets.[27] Currently due to the novelty and excellent resistance to

chemical and thermal treatments, the exploration of layered h-BN is still in its infancy.

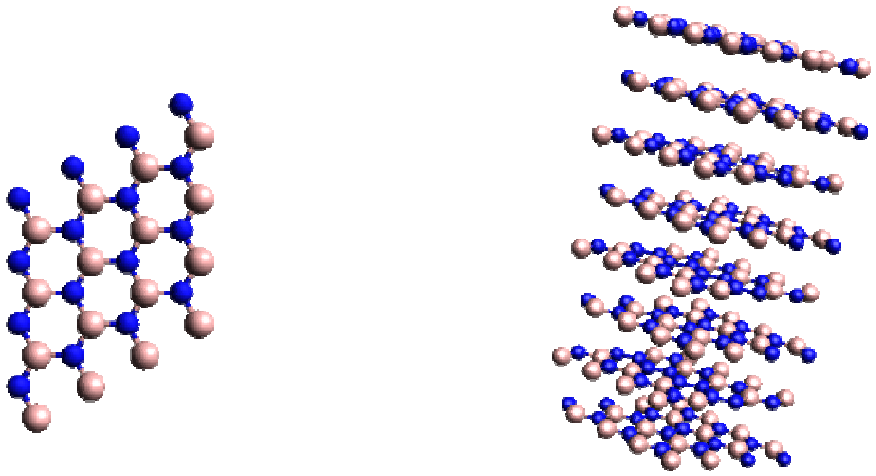

Figure 2. Structures of monolayer h-BN and bulk (AB) h-BN (B: blue, N: pink)

Production and Properties of Hexagonal Molybdenum Disulfide (MoS_2) and Monolayer (2H)-MoS_2

Another class of IGAs, known as transition metal dichalcogenides (TMDs), includes hexagonally layered compounds of disulfides (NbS_2, MoS_2, CdS_2, WS_2, HfS_2, TaS_2…) and their respective diselenides and ditellurides. The observed properties of IGAs are broad given the interactions between the transition metals and the corresponding chalcogenides. One TMD of particular interest is MoS_2 whose hexagonally symmetric crystal structure (Figure 1.3) was elucidated in 1923 by Dickinson and Pauling from naturally occurring molybdenite.[28] In 1966, the isolation of thin sheets using micromechanical cleavage was first reported by Frindt who produced 5-6 layers of MoS_2.[29] One synthetic method to produce MoS_2 reported in 1990 used the decomposition of an ammonium thiomolybdate ($(NH_4)_2[Mo_3S_{13}]$) cluster compound to form catalytic MoS_2.[30] This method was modified and exploited to synthesize 2-D MoS_2 sheets on substrates.[31] Using CVD methods, large-area sheets of layered MoS_2 were grown using deposited sulfur to adsorb on Mo films[32] and utilizing a gas phase reaction between (molybdenum trioxide) MoO_3 and S powders on a SiO_2 substrate.[33] The properties of MoS_2 are diverse, as bulk MoS_2 is an indirect band gap semiconductor (~1.2 eV) whereas monolayer MoS_2 is a direct band gap semiconductor (~1.8-1.9 eV).[13, 14, 34-37] Furthermore, MoS_2 exhibits excellent lubricity and elasticity,[38, 39] ferromagnetic and antiferromagnetic domains,[13, 40] and enhanced mechanical and fire-retardant properties in polymeric composites.[41] In 1989, a simple method to obtain monolayers from bulk

crystalline MoS_2 was investigated using an exfoliation method by soaking in n-butyllithium, and the structure of the restacked MoS_2 determined.[42] Considering the characteristic properties of this TMD, development of facile production and chemical modification protocols to generate tailored MoS_2 sheets would be significant.

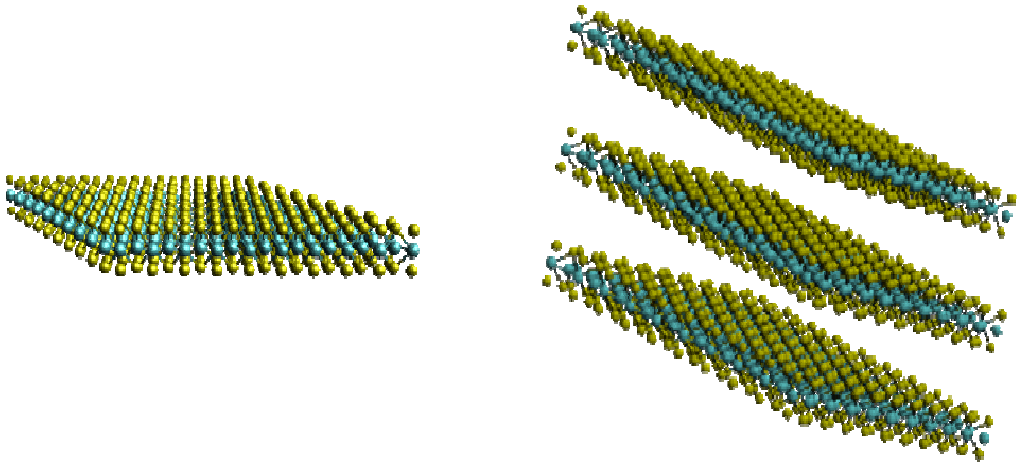

Figure 3. Structures of monolayer MoS_2 and bulk MoS_2 (S: yellow, Mo: teal)

Chemistry of Hexagonally Layered 3-D (2-D) Graphite (Graphene), h-BN, and MoS_2

The first chemical modification of graphite was performed in 1859 by Brodie using oxidation chemistry to produce graphite oxide, later modified by Staudinger, and finally the synthesis of graphite oxide improved by Hummers to by using a quicker, safer oxidation treatment of graphite.[43] The oxidation of graphite allows for the peeling of oxidized layers which consist of monolayer graphene oxide which can be reduced or thermally treated to obtain monolayer graphene. However some drawbacks to this process exist as the Hummers method entails harsh treatment of graphite which is undesirable, and difficulties of the reduction process of graphite oxide were observed by thorough characterization.[44] Numerous other chemical methods to modify graphene and graphite have been reported,[45-48] and broadened the applications of the materials. Various chemical modifications, including particle doping, substitutional doping, non-covalent, and covalent modifications,[46] were performed to tailor the inherent properties of graphene and graphite. Also various methods to perform graphene modification included CVD, particle and polymer deposition, wet chemistry for small molecule and polymer intercalation/grafting, ultrasonication, and microwave irradiation.[46-49] A significant issue, addressed by Quintana and Prato, with these methods involves difficulties in modification or functionalization of graphite to mass produce desirable graphene.[48] Quintana and Prato reported the functionalization of bulk graphene material using a dendrimer and later decorated the functionalized graphene with gold nanoparticles.[45] This

method understandably required very specific reagents to obtain the desired functionalities necessary for decorating with gold nanoparticles.

The chemistry of h-BN has not been explored as thoroughly compared to graphene. Given the relative novelty and excellent chemical resistance of h-BN, methods to chemically functionalize h-BN are mainly theoretical and empirically are limited.[19] However, noncovalent functionalization with a conjugated polymer has been performed to obtain h-BN nanosheets.[24] Another viable (noncovalent) method of functionalization, due to the strong ionic behavior of h-BN, is Lewis acid-base complexation which was performed using octadecylamine (ODA).[27, 50] Few accounts regarding direct covalent functionalization of h-BN have been reported, including hyperbranched polyamide grafting,[51] oxygen radical functionalization,[52] nitrene addition,[53] and controlled surface oxidation on a metallic surface.[54]

Pertinent modification of MoS_2 primarily consists of chemical intercalation,[55] which is commonly performed by soaking crystalline MoS_2 or ultrasonication of MoS_2 powder in n-butyllithium and various to produce an intercalation compound of Li_xMoS_2.[42, 56, 57] Another method, previously applied to WS_2,[58] using $LiBH_4$ was successful in promoting lithium ion intercalation.[59] Lithium and other alkali ions were also incorporated using a simple electrochemical method.[60, 61] Chemistry beyond alkali ion intercalation was explored with organic compounds including polymers which formed organic/MoS_2 and polymer/MoS_2 intercalation compounds respectively.[40, 42, 62-68] Recently, the

surface functionalization of colloidal, exfoliated Li_xMoS_2 with octa(vinyl) polyhedral oligomeric silsesquioxanes was prepared by thiol-ene click chemistry upon addition of azodiisobutyronitrile.[69]

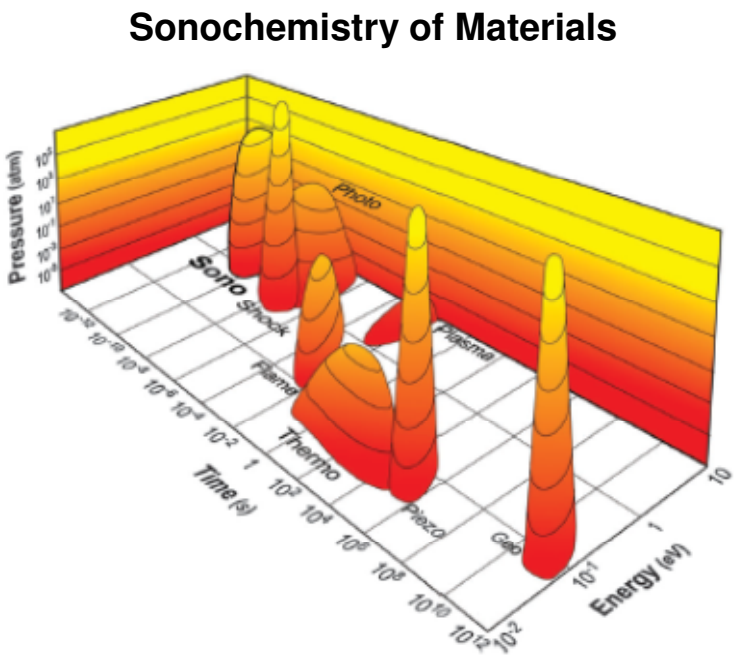

Figure 4. Comparison of chemical behavior using various energy sources from Ref. #75

Many of the methods previously mentioned to chemically exfoliate 3-D hexagonally layered precursors of graphite, h-BN, and MoS_2 incorporated sonication to overcome the van Der Waals forces between the sheets. Sonication propagates sound waves through the liquid media, which produces cavitation bubbles of immense intensity. The hot spots promote quick interactions during acoustic cavitation and have temperatures up to ~5000 ℃ and pressures of ~500 atm.[70]

The fundamental investigation of multibubble cavitation showed that sonication of water in the presence of air generated nitrate ions and hydroxide radicals and to a lesser extent generated photons.[71] This suggested the capability to promote specific chemistry defined by the liquid medium. However the formation of hot spots was determined, using spectroscopic techniques, to be heterogeneous during sonication with an ultrasonic tip-horn sonicator.[72] Comparatively, the lower intensity of sonicator baths (~42 KHz) does not provide significant intensity but are suitable for interactions between liquids and passive, yet still somewhat reactive solids.[73] The reaction times, pressures, and temperatures generated by sonochemical reactions are distinct (**Figure 4**) when compared to other methods. Furthermore bath sonication can provide reactions uniquely different to those in solid-state mechanochemistry,[74] and therefore avoids the limitations from the mechanical "Scotch-tape method" of graphite exfoliation. By applying sonication to synthesize and modify materials, tailoring nanostructures would expand the applications of materials and provide simple chemical routes for synthesis and modification.[75]

The effects of sonication on graphite were first studied for an aqueous dispersion, but focused strictly on the degradation products observed from sonication damage.[76] In 2008, one group reported via sonication a simple liquid exfoliation method of graphite in air using various solvents produced isolated monolayer sheets of graphene.[77] They observed that isolation of sheets by centrifugation limited the edge functionality and oxidation from radicals and

trapped oxygen gas generated during sonication, even at high concentrations of dispersed graphene.[78] Similarly, for graphene isolated from exfoliated graphite in aqueous/surfactant solutions, X-ray Photoelectron Spectroscopy (XPS) indicated low radical generated defects or physisorbed surfactant.[79] Furthermore by relating the solubility parameters of the solvents and surfactants to the extent of graphite exfoliation, optimization to increase yields using sonication were explored.[80] While sonication had been used prior to exfoliate graphitic materials,[81] the simple sonochemical fragmentation introduced by Coleman's group offered a highly viable scalable approach. Also based on the Hansen solubility parameters (HSP) determined by Coleman's group for graphene, successful exfoliation of graphite using highly volatile solvents like $CHCl_3$ and 2-propanol yielded sheets with good dispersion characteristics.[82] Although sonication-assisted exfoliation had been performed in previous work with IGAs including h-BN[83] and MoS_2[84], the isolation, resulting structures and properties, and optimization of exfoliation to obtain monolayer forms was not reported until quite recently.[85] Extended investigation of exfoliation to 2-D sheets of 3-D precursor TMDs in solvents[86] and aqueous/surfactant solutions[87] demonstrated the versatility of TMDs. Efforts were also made to increase yields of large sheets of exfoliated MoS_2 [88] which could be size-selected using centrifugation.

The integration of chemical reagents and sonication has been used to generate nanomaterials and successfully modify macromolecules.[73] However, very little work regarding sonication induced covalent functionalization of

graphite, h-BN, and MoS_2 using various chemical reagents has been reported. Functionalization of graphene using sonochemical exfoliation of graphite was performed to graft polymers onto the sheet edges and surfaces using styrene to generate polystyrene functionalized graphene[89] and sonochemical degradation of poly(vinyl alcohol) (PVA) to generate PVA grafted graphene. [90] For h-BN, water-hydrolysis of monolayer and few-layered h-BN was possible by sonication inducing cutting of h-BN sheets.[91] Currently, no reports of covalent modification via sonication of MoS_2 are available, although just recently highly-dispersible MoS_2 sheets were prepared by ultrasonication in water of a pretreated MoS_2 crystal.[92]

Applications of Hexagonally Layered Graphite and IGAs for Polymer Composites

The applications of the 2-D forms and 3-D bulk materials are broad given their extensive properties. Inherent properties of graphene, and the monolayer forms of h-BN and MoS_2 make them useful materials for various applications. Some of these include electronics, photo- and opto-electronics, dielectrics, capacitors, magnetic devices, high temperature lubricants, chemical sensing and storage, catalysis, and polymer nanocomposites.[7, 16, 25, 37, 38, 46, 93-108] Polymer nanocomposites encompass various composite systems which can display excellent synergistic behavior between the nanoscale material/filler and polymer matrix, which translates to enhanced properties of host polymer. However previously for graphene composites enhancement of properties in host polymers were determined to depend on the dispersion of the nanofiller in polymer[103]

which is dependent upon filler polymer interaction. The interfacial interactions between filler and polymer can be increased by chemical modification of the filler material which is reflected by polymer properties. Previously chemical treatment of graphite to produce expanded graphite increased the glass transition temperature (T_g) of poly(methyl methacrylate) (PMMA) by ~30°C at 0.05 wt.% loading.[99] Layered filler dispersion is not only dependent upon chemical composition but also is influenced by number of layers, size, and structure of the sheets, as ~2-3 micron length graphene sheets were better than nanoscale graphene for mechanically reinforcing PMMA and poly (vinyl alcohol) (PVA) respectively.[109, 110] Addition of exfoliated h-BN to PVA at 0.12 wt.% bettered the modulus and strength by ~40% compared to the pure PVA,[111] and increased solvent stability of exfoliated h-BN was shown using an amine terminated poly(ethylene glycol) polymer solution.[27] Polyaniline intercalated MoS_2 exhibited improved conductivity,[66] which was also reported with various other intercalated conductive polymer composites.[40, 63, 68] Improvement of polymer strength and lubricity was reported for MoS_2 composite systems, including various host polymers of PVA, thermoplastic polyurethane, and high-density polyethylene.[41, 62, 64, 65, 69] Therefore based on desired composite properties, performing either noncovalent or covalent functionalization and controlling the size and structures of the modified fillers to increase the dispersion of the fillers in host polymers could be tailored to produce hybrid composites with improved conductivity, mechanical reinforcement, thermal resistance, and elevated lubricity.

CONCLUSIONS AND PROPOSED EXPERIMENTS

Given the large quantities necessary for industrial composite production, associated costs and simplicity of processing methods must be considered. Previous work from our group explored chemical functionalization of nanotube structures, which requires expensive precursors/chemicals and did not focus on industrial scability for composites.[112-116] As difficulties to exfoliate and chemically modified 2-D and 3-D particles graphite for small-scale applications still exist currently, exploring a cost effective method to produce highly dispersible particles with excellent enhancement of polymer properties is extremely difficult. However given the recent progress using sonication to generate exfoliated and modified layered materials, various methods using this technique could be developed to obtain large quantities.

In this dissertation, sonochemical methods were used to produce fragmented, restacked powders using commercial precursors. The methods were developed yielding near quantitative yields with emphasis on chemical costs and hazards. Changes in chemical composition and structural properties due to fragmentation of the powders were observed to affect the macroscopic properties of the fillers. Furthermore the colloidal behavior of the particles in various solvents and polymers were correlated to reported solubility parameters. In Chapter 1, extensive characterization of damaged graphite and multilayered graphene suggested functionalization of the powders, however DSC analysis of composites demonstrated poor filler interaction with rigid plastics, which has

been observed previously.[117] In Chapter 2, we developed other conditions for fragmentation to enhance particle properties for composite dispersion, and observed characteristic differences in the restacked samples. The diserpersability and photoluminescence of fragmented MoS_2 particles in aqueous dispersions of PEG were analyzed in Chapter 3 to determine the particle/polymer interaction and the application for polymeric coatings.

CHAPTER I
BULK FRAGMENTATION OF COMMERCIAL GRAPHITE AND MULTI-LAYERED GRAPHENE POWDERS USING A LOW-BOILING POINT SOLVENT

Abstract

The need to produce large quantities of graphitic materials displaying excellent conductivity, thermal resistance, and tunable properties for industrial applications has spurred interest in new techniques for exfoliating graphite. In this report, sonication-assisted exfoliation of graphitic precursors in the presence of chloroform is shown to produce chemically and structurally unique fragmented graphitic materials in high yields. These fragmented graphites, referred to as mesographite and mesographene respectively, exhibit unique properties, which depend on the number of layers and exfoliation conditions. Structural characterization of mesographene reveals the presence of nanoscale 2-dimensional graphene layers, and 3-dimensional carbon nanostructures sandwiched between layers, similar to those found in ball-milled and intercalated graphites. The conductivities of mesographite and mesographene are 2,700 and 2,000 S/m, respectively, indicating high conductivity despite flake damage. Optical absorption measurements of mesographite dispersed in various solvents showed significant changes in dispersion characteristics, and also provided insight regarding their macroscopic colloidal behavior. A mechanism for functionalization and formation of capped carbon nanostructures is proposed by integrating the chemical and structural characterization in relation to the various carbon structures observed by electron microscopy. Composites based on common polymers were prepared by solution processing, and changes in

thermal properties indicate improved dispersion of mesographite in polar polymers.

Introduction

Due to the exceptional electronic and thermal properties of graphene, the ability to produce it in large quantities has become a major goal of nanotechnology,[17, 118] with potentially huge impact across multiple scientific disciplines, including conductive inks for flexible displays, graphene-based nanomaterials for clean energy applications, polymer-based nanocomposites for cars, aircraft, and protective garments, and medical devices and systems. Production of graphene from precursor materials has commonly been performed by two routes, micromechanical exfoliation and chemical exfoliation.[8, 11, 17, 44, 99, 119-127] The production of graphene from micromechanical exfoliation, the most utilized method, has limitations such as low yield and production of less monolayered graphene and more thicker flakes.[17] Exploration of different exfoliation techniques to improve graphene production has broadened the scope of graphene related research.[8, 47, 103] Chemical exfoliation is an effective process for obtaining monolayer graphene through oxidative reactions to form graphene oxide, which is subsequently reduced.[8, 44, 99, 123-127] The chemically induced polarity of graphite oxide allows for layers of graphene oxide to be peeled off using solvent for exfoliation. This approach yields pristine graphene, but with a yield of only ~1 wt%.[44] Dispersibility of reduced graphene oxide in a range of solvents has been thoroughly explored, giving rise to fundamental information

regarding these colloidal suspensions.[128, 129] Graphite intercalation compounds (GIC), which have been shown to generate high yields of functionalized graphenes containing only edge defects, can be tailored for excellent dispersibility in various solvents and surfactant/water solutions; however these treatments also require harsh reagents and extensive processing (thermal or chemical) to generate preferred functionality.[47, 130] Mild sonication of bromine-GIC (prepared using commercial precursors and a simple dip-coating method) in water indicates that bromine concentration affects interactions between sheets leading to potential tailoring of graphites and graphenes by size, layers, and chemical composition.[131] Hernandez et al. demonstrated that by employing sonication the exfoliation of graphite in organic solvents yielded few layered and monolayered graphene, displaying only minor structural defects and excellent electrical properties. This group also elucidated the experimental parameters governing solvent exfoliation.[77] Modification of this exfoliation procedure has further expanded our understanding of exfoliation of graphite in various liquid media.[80, 132-135] Aqueous polymer solutions are capable of graphite exfoliation, producing water-dispersible graphenes.[133] Graphite exfoliated by sonication in surfactant/water was shown to affect dispersibility, as chemisorbed surfactant increased resistance to reaggregation of graphene layers.[79, 80, 136]

Further investigation of the colloidal behavior of exfoliated graphites has become an area of great interest.[137] Efforts to generate large quantities of dispersible material have been reported. High concentrations of exfoliated

graphite were obtained using N-methyl-2-pyrrolidinone (NMP), and the sonication and centrifugation process was analyzed to determine exfoliation efficiency and concentration.[78, 138, 139] However extensive sonication times were necessary, and the solutions were not filtered. Exfoliation of graphite in styrene for *in situ* preparation of nanocomposites generated exfoliated graphite with covalently grafted polystyrene in ~10% yield.[89] Isolation by centrifugation generally precludes obtaining large quantities. For certain applications, the ability to obtain both high yields and highly dispersible material is desired as complete exfoliation and rigorous size-selection is unnecessary. In this work, we present a high-yielding approach to produce of graphitic fillers with unique size, shape, and chemical composition. Characterization of both bulk and fractionated materials were measured to observe the effects from sonication induced damage and compared to previous literature on exfoliated graphitic materials. The thermal effects of the macroscopic filler were investigated for various plastic composites, prepared by solution blending filler and polymer and subsequently precipitating in solvent to trap the filler material.

Sonochemical Exfoliation

For the synthesis of exfoliated mesographite and mesographene the corresponding precursor powder (250 mg) was dispersed in solvent (117 mL) in a round bottom flask (250 mL). These solutions were kept in an ice bath during sonication to prevent pyrolysis and solvent evaporation. The solutions were sonicated for 2 hours in air using a 20 KHz Q Sonica sonicator probe tip at a

power of ~90 W and stirred using a Teflon stir bar. During intense stirring, the probe tip was immersed in solvent at a maintained depth of ~1 inch. After sonication, solutions were then filtered using a 0.22 μm PTFE pore size filter. The obtained powders were then dried for 14 hours at 40℃. After drying, the mass of the product was obtained and the material subsequently characterized. To obtain low-damage nanoscale products, we fractionated solutions (sonicated for 30 minutes) by immediately decanting the solution after sonication. Approximately 20 ml was transferred to a centrifuge tube (50 mL) and diluted with 20 mL of fresh solvent. The tubes were then centrifuged at 3000 rpm for 10 minutes. The obtained supernatant was collected (~80%) while not disturbing the pellet at the bottom of the tubes, and the obtained solution filtered using a 0.22 μm PTFE pore size filter. The obtained products were referred to nanographite (from precursor graphite) and nanographene (from 20-30 layer precursor graphene) were vacuum dried at 40℃ for 14 hours. The mass of the products were then measured to determine percentage yield, and the products subsequently characterized.

Preparation of Polymer Composites

Polymer composites were synthesized by solution processing. The obtained MG was dispersed in ~10 mL of chloroform though momentary sonication to produce dilute dispersions (<0.05 mg/mL). While stirring vigorously, specific quantities of polymer were added, and the resulting composite solution stirred briefly. For polystyrene, poly(methylmethacrylate), and

poly(cyclohexadiene) solutions, polymer composites were prepared by precipitation in excess methanol. For poly(4-vinyl pyridine) composite solutions, the polymer composites were precipitated in excess hexane. The composites were then filtered and vacuum dried at 25ºC for 14 hours.

Materials and Methods

Solvents used for experiments were acetone (Fisher, Reagent Grade), chloroform (Fisher, Reagent Grade), carbon tetrachloride (Acros, Extra pure (99%)), N-methyl-2-pyrrolidinone (Acros, Reagent Grade), triethylamine (Fisher, Reagent Grade), acetone (Fisher, Reagent Grade), toluene (Fisher, Reagent Grade), methanol (Fisher, Reagent Grade) and hexane (Fisher, Reagent Grade). All solvents were used as received. Multi-layered (ML) graphene powder (Graphene Supermarket, A-O2, 20-30 layers) and graphite powder (Sigma-Aldrich, < 20µm) were used as received. To obtain nanographite and nanographene, centrifugation was performed with glass tubes using an Eppendorf Centrifuge 5702. Polymers used for composite preparation were polystyrene (Pressure Chemical, 151K), poly(methylmethacrylate) (Pressure Chemical, 121K), , and poly(4-vinylpyridine) (Sigma-Aldrich, 60K), and poly(1,3-cyclohexadiene) (30K), which was prepared using a previously reported method.[140] Thermogravimetric analysis (TGA) was performed using a TA Instruments Q-50 TGA. The sample was heated from 25℃ to 900℃ in the presence of compressed air (Airgas) at a flow rate of 40 mL/min. Maximum degradation values were obtained in TA analysis from maximum peak values of

first derivative curves displaying Δwt.% / Δ*T* (°C). Fourier-Transform Infrared Spectroscopy (FT-IR) was carried out using a Varian 4100 FT-IR performed using KBr (Aldrich, Spectroscopy) as a reference and precursors for background subtraction. Elemental analysis was performed by Galbraith Laboratories (Knoxville, TN). X-Ray Photoelectron Spectroscopy (XPS) was collected using a Physical Electronics model 5400 X-ray photoelectron spectrometer equipped with non-monochromatic Mg K_α (1253.6 eV) and Al K_α (1486.7 eV) X-rays. The data presented was collected using the non-monochromatic Al K_α X-rays. The samples were mounted on the sample puck by placing a small circle of double-sided tape (< 1 mm diameter) on the puck and then pressing the powder down over the puck to cover the tape. A stainless steel mask with a 3 mm diameter hole was then placed over the powder and secured with screws. The samples were placed in the introduction chamber for approximately 15 minutes before being transferred to the analysis chamber. The analysis area was set to 1.1 mm diameter spot size. During data collection, the analysis chamber pressure was approximately 1.0×10^{-9} Torr. Survey spectra were collected at low resolution, which corresponds to analyzer pass energy of 89.45 eV. They were collected in increments 0.5 eV/step and an integration interval of 50 ms/step. The complete spectrum consists of the average of 15 cycles. Multiplex spectra were collected at high resolution corresponding to analyzer pass energy of 22.35 eV with increments of 0.1 eV/step and an integration interval of 20 ms/step. The carbon 1s (C 1s), oxygen 1s (O 1s) and chlorine 2p (Cl 2p) photoemission regions were

collected with a frequency of 1, 10 and 10, respectively, for each cycle. Twenty cycles were averaged to generate the multiplex spectra. Raman analysis was performed on powder samples using a JY-Horiba T64000 spectrometer with an 1800 gr. mm^{-1} grating, 514 nm laser excitation (incident power ~1 mW), and CCD detector. Low-Voltage Transmission Electron Microscopy (LV-TEM) images were obtained using a Low-Voltage Electron Microscope from Delong Instruments at 5 kV. Dilute solutions (< 0.01 mg/mL) from dispersed product in chloroform were centrifuged at 1000 rpm then drop cast on a holey carbon grid. Scanning/Transmission Electron Microscopy (STEM) images were obtained using a Zeiss Auriga STEM operating at 30 keV. Samples from concentrated solutions were drop cast on a holey carbon grid. X-ray Diffraction (XRD) analysis was performed on powder samples in atmospheric conditions using a Panalytical Empyrean diffractometer equipped with a Ge monochromator using Cu-Kα (λ=0.1540 nm) radiation. Samples were analyzed in the range of 2θ= 5°-70° with a step size of 0.02°. Dielectric Spectroscopy was performed on a Novocontrol Alpha-A impedance analyzer. Powder samples were packed with a needle-like piston into a predrilled 0.06 cm in diameter cylindrical hole in a 0.475 cm thick Teflon sheet. A conductive silver paint was applied at the outer edges of the samples in order to minimize the contact resistance effects. Optical measurements (UV-Vis) were performed in the wavelength interval 250-800 nm using a Thermo Scientific Evolution 600 UV-Vis Spectrometer with Optiglass 10 mm cuvettes. Differential Scanning Calorimetry (DSC) measurements were

made using TA Instruments Q1000 DSC with a nitrogen gas purge of 50 mL/min. Samples were pressed into thin films using Carver Laboratories model C heater/press with a pressure of 5 tons and at a temperature corresponding to T_g + 10 ℃. The pressed films were then annealed at T_g + 20℃ for 12 hours. Two cycles were run in the temperature range of 25 ºC to T_g + 40℃ , with the first cycle held at T_g + 40℃ for 2 hours.

Results and Discussion

Ultrasonication has been shown to induce oxidation of and generate radical species from solvents and water.[141-143] Exposure of graphitic material to ultrasound has generated various organic and inorganic byproducts.[76, 81] The chemical compositions of these byproducts were characterized by Atmospheric-Pressure Chemical Ionization Fourier Transform Mass Spectrometry (APCI-FTMS), and primarily consisted of monosubstituted phenyls and phenols. The generation of polycyclic aromatic hydrocarbons from sonication of graphite oxide can produce nanotube structures.[144] In our work, using solvent instead of a reactive monomer, a procedure similar to one previously reported[89] was employed to produce high-yields of fragmented graphenes from multilayered graphene (20-30 layers) and graphite precursors. Chloroform, a volatile and thermodynamically favorable solvent for solution blending of polymers and additives, was chosen as the primary solvent for investigation as it is capable of dispersing graphene up to a concentration of 3.4 μg/mL.[82] For production of large quantities of defect-free graphene, it has been shown that changes in

concentration are dictated by sonication time.[78] Maintaining a constant initial concentration, we focused on short sonication times while also achieving high yield.

Differentiation between products was based on their respective forms (bulk or isolated) and corresponding length scales. Reaction conditions and material properties of fragmented products are presented (**Table 1**).

Table 1. Reaction conditions and characteristics of fragmented graphites and graphenes

Precursor	Solvent	Sonication Time (minutes)	Yield[a)] (%)	T_{max}[b)] (°C)	Weight loss[c)] (wt.%)	UV-Vis$_{ABS}$[d)]	Conductivity[e)] (S/m)
Graphite				**691**	**~0.3**		**3830**
1	**Chloroform**	**30**	**~1.6**	**654**	**~12.8**	**ND[f)]**	**ND**
2[g)]	**Chloroform**	**120**	**~96.0**	**705**	**~1.3**	**0.613**	**2700**
Graphene				**690, (447)**	**~12.9**		**10,000**
3	**Chloroform**	**30**	**~6.4**	**710, (450)**	**~26.6**	**1.013**	**700**
4[g)]	**Chloroform**	**120**	**~98.8**	**704 (432)**	**~16.7**	**1.171**	**2000**
5	**NMP**	**120**	**~18.0**	**636**	**~29.0**	**0.949**	**1480**
6	**Toluene**	**120**	**~0.5**	**ND[f)]**	**ND[f)]**	**ND[f)]**	**ND[f)]**

[a)] Percent yield calculated as weight of final product obtained after filtration divided by weight of precursor. [b)] Determined from as the temperature at which maximum percentage of weight loss occurs; for precursor graphene and graphene products, a second T_{max} was observed. [c)] Change in weight (%) from TGA in the temperature range of 200-500 °C. [d)] Absorbance (arbitrary units, a.u.) measured at λ = 660 nm of dispersed solutions with concentrations of 0.1 mg/ml in chloroform. [e)] Limiting d.c. conductivity determined from dielectric spectroscopy. [f)] ND indicates not determined due to sample limitations. [g)] Products were not centrifuged and filtered as-synthesized.

Sample 1, referred to as nanographite, gave a poor yield as only ~1.6 wt.% was retained. However Sample 3, referred to as nanographene, had an increased yield of ~ 6.4 wt%, roughly 4 times greater. The higher yield of nanographene can be attributed to few-layered and monolayered precursor materials and better solvation, increasing acoustic cavitation of generated solvent bubbles and nebulization of solvent.[73] Despite increasing yield, large quantities of fragmented material were not obtained, for both precursors. In order to increase yields, solutions were subjected to 2 hours of sonication. Sonication of precursor ML-graphene in NMP, Sample 5, provided in a yield of ~18.0 wt% giving the highest-yielding fractionated product. However toluene yielded hardly any fractionated material, indicating toluene as a poor medium for exfoliation, consistent with previously determined dispersion characteristics.[77] Mesographene (Sample 4) was synthesized similarly to all other samples, but it was not centrifuged in order to obtain a larger quantity of material. The entire solution was filtered for analysis, giving a near quantitative yield of ~98.8 wt%. Similarly, processed mesographite (Sample 2) also was not centrifuged and gave a near quantitative yield (~96.0 wt%) of mesographite. The obtained powders were then characterized and compared to precursors. This is necessary as significant differences were observed between fragmented graphenes obtained from different precursor sources.[145]

The presence of oxidative functionality and thermal stability of materials were analyzed using TGA. Decomposition profiles of graphite and graphene

precursors and fragmented products (Samples 1-4), heated in air, are shown (**Appendix A, Figure 12**).The nanographite exhibited a decrease in T_{max} to 654℃, indicating significant generation of functionality and smaller flake size. Mesographite displayed a T_{max} of 705℃, characteristic of an increase in thermal resistance to oxidation. Since graphene and graphite are more thermally stable than their oxidized derivatives, functionality from processing can be observed using TGA.[8, 44, 46, 99, 125, 127] The change in percentage weight loss for each product was calculated in the region of 200-500℃, as it is well understood that any oxidative functionality and/or organic moieties present in the fragmented materials will demonstrate weight loss in this temperature range. For the precursor graphite weight loss was only 0.3%, whereas for mesographite and nanographite, the weight loss increased to 1.3% and 12.8%, respectively. Nanographite exhibited an increase in weight loss of ~12.5% indicating the possible presence of oxidized material or chemisorbed residue. This increase in weight loss is substantially larger than that of mesographite, as its weight loss is likely from sonication creating a small quantity of functionalized nanoscale material. These increases in weight loss follow the trend observed in TGA for the reduction process of graphite oxide.[127] Precursor ML-graphene had two major T_{max} values of 447℃ and 690℃, the first indicative of flake edge oxidation and the second corresponding to total flake oxidation. Both nanographene and mesographene exhibited increases in the higher T_{max}; interestingly mesographene exhibits a decrease in the first observed T_{max} (432℃), probably

due to extensive oxidative damage induced on flake edges and solvent residue absorbed during sonication. For precursor ML-graphene, weight loss from 200-500℃ was 12.9 wt%, possibly from chemisorbed species from the precursor synthesis method. In comparison, mesographene and nanographene showed increases in weight loss of 3.8% and 13.7%, respectively, suggesting significant oxidative functionality or chemisorbed moieties (trapped fragmented carbon) are present in the nanoscale material.

The FT-IR spectra confirmed the presence of functional groups resulting from sonication. FT-IR spectra for mesographite and mesographene, with background subtraction of both respective precursors, were obtained (**Appendix A, Figure 13**). The spectra for both samples are quite similar, indicating that the synthesis method did not greatly affect the generated chemical functionalities. The peaks at ~3420 cm^{-1} and 3350 cm^{-1} indicate the presence of free or bound -O-H groups corresponding, respectively, to either trapped water or hydroxyl groups of graphitic oxides.[146] Strong absorptions at ~ 2750, 2690, 2640, 2560, and 2520 cm^{-1} could be due to either strongly hydrogen-bonded carboxylic acid groups or dimerization of proximal carboxylic acid groups.[147, 148] These peaks are not observed in graphite oxide or graphene oxide prepared by Hummer's method. Surprisingly, a strong absorption at ~1720 cm^{-1}, the band for C=O stretching, is not present in either sample. The absence of this peak is most likely a result of the highly conjugated aromatic structure and internal hydrogen bonding, which can mask this peak.[147] Peaks at ~1580 cm^{-1} decrease in intensity

as compared to their respective precursors, similarly observed from the loss of C=C bonds in graphitic oxides.[146] Peaks of small intensity at ~1400 cm^{-1} and 1360 cm^{-1} are found in graphitic oxides, a feature of -O-H and -C-OH functionalities, respectively.[146] The sonication procedure appears to generate specific functionalities and/or chemisorbed species, which have not been observed as intensely in size-selected nanoscale graphene.[79, 80]

To understand changes in chemical compositions, elemental analysis to determine carbon, hydrogen, and chlorine content of mesographite and mesographene were carried out with precursor ML-graphene (**Table A1**). After converting ML-graphene to mesographene, the percentage of carbon decreased by 4.1%. Considering this decrease and the minimal change in oxygen content after sonication, it appears likely that highly oxidized fragments reacted or could have decomposed during the sonication process and removed by filtration. Hydrogen content increased only slightly as a result of sonication, which was similarly seen for highly reduced graphene oxide.[44, 127] However, there is a substantial increase in chlorine content, as the atomic ratio of carbon to chlorine decreased. Mesographene appears to have nearly ~33 more chlorine atoms per carbon as compared to the precursor material. Radical abstraction of chlorine, from chloroform sonolysis, could account for chlorine functionality along the edges of the graphene. Radical generation during sonication of graphite in styrene is known to initiate bulk polymerization, covalently tethering polymer on edges and surfaces of the fragmented graphene.[89] The presence of ethanol,

added to stabilize chloroform, could also contribute to reactive species generated during sonication.[149, 150] Possible sonolysis of ethanol could account for increases in hydrogen and oxygen content and facilitate functionalization of small sp^2 carbon fragments formed during sonication.

To confirm the presence of covalent surface functionalization, XPS was performed on graphite and mesographite. A summary of elemental concentrations derived from the survey spectra is provided (**Table A2**). The multiplex spectra with sub-peak deconvolution of the C 1s photoemission region (**Appendix A, Figure 14**) for both graphite powder and mesographite powder were obtained, and the fits were established by using single crystal HOPG (SPI, grade 2) as a reference. A satisfactory fit was produced for the graphite powder and mesographite powder by using only the C-C sub-peak and the $\pi \rightarrow \pi^*$ shakeup sub-peak. The O 1s photoemission region for both samples was also measured (**Appendix A, Figure 15**). Mesographite displayed a slight increase in the relative intensity of the high binding energy sub-peak in comparison to the low binding energy sub-peak, suggesting a larger amount of C-O functionalities (though very slight), which has been previously seen for fractionated samples.[77] XPS analysis of this region displays no significant increase of covalently bonded oxygen-containing functionalities generated by sonication. To determine covalently bonded chlorine content, spectra of both precursor and mesographite were obtained **(Figure 5)** containing the survey comparison of the Cl 2p region

for graphite and mesographite and de-convolution of the Cl 2p photoemission region for mesographite.

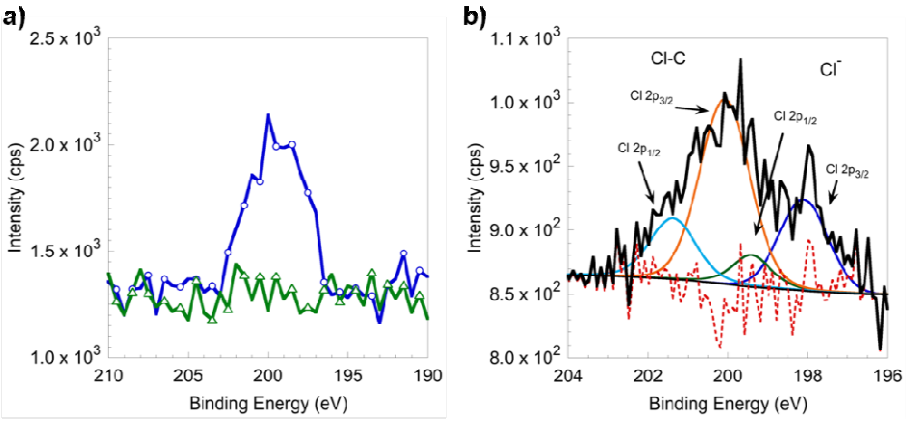

Figure 5. XPS spectra of a) survey spectra comparison of the Cl 2p regions of mesographite and precursor graphite and b) de-convoluted of Cl 2p region of mesographite

The presence of –C-Cl bonds are confirmed, which likely exist at sheet edges, however trapped chloroform could also account for this observation.

Raman spectroscopy was utilized to discern any defects generated after sonication. Using the ratio of the intensities (I_D/I_G) of the disorder band (known as the D band, ~1350 cm^{-1}) and the tangential band (G band, ~1580 cm^{-1}), changes in disorder for sp^2 carbon allotropes can be compared. The observed Raman spectra (**Figure 6**) and changes in Raman peak characteristics for the G band and 2D band (**Table A3**) demonstrate the effects induced disorder of the exfoliation process on the mesoscopic samples.

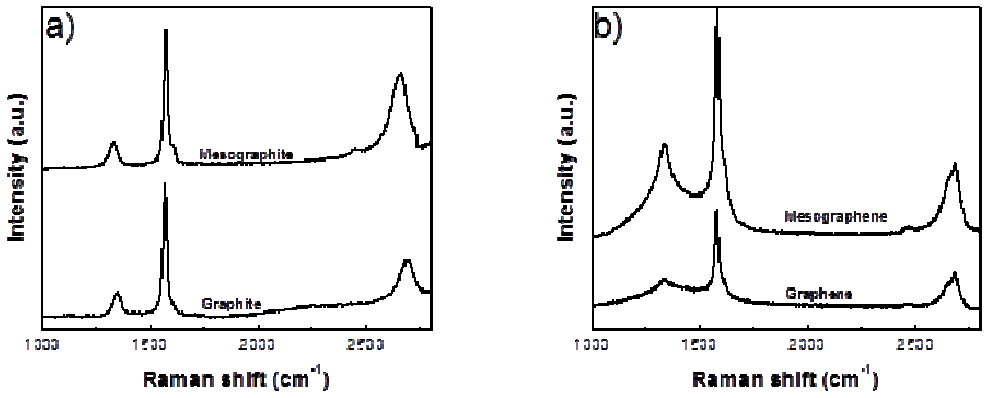

Figure 6. Raman spectra of precursor and mesoscale a) graphites and b) graphenes

For mesographite, the I_D/I_G ratio was measured to be 0.18, very close to the ratio of 0.14 obtained before sonication in chloroform.[82] This is likely a result of large micron length sheets not exhibiting defects seen in nanoscale graphene.[136] For graphene, the measured I_D/I_G ratio was 0.04, indicating little defect in the precursor. The I_D/I_G ratio increased to 0.46 for mesographene, indicating a large increase in the disorder of the sample. In-plane crystallite sizes (L_a) were calculated from the laser line wavelength (C'(λ)) and corresponding I_D/I_G ratios (Table S4 in Appendix A), using the equation:[151, 152]

$$\frac{I_D}{I_G} = C'(\lambda)(L_a)^2 \quad (1)$$

An increase in L_a values after sonication was observed and is further supported by increase in T_{max} seen from TGA.[153] The increase in L_a also indicates that the increase in the I_D/I_G ratio may be simply caused by an increase in sheet edges being measured by the excitation laser spot size, a result of smaller sized

graphene sheets. A shift upfield in the G band of mesographite (3 cm^{-1}) and mesographene (2 cm^{-1}) is characteristic of monolayer graphene. Changes in number of layers present in graphitic material causes shifts to lower frequency of the 2D band peak at ~2700 cm^{-1}. Graphite and mesographite exhibited different peak values for maximum intensity of the 2D band, centered at 2693 and 2661 cm^{-1} respectively. The shift of 31 cm^{-1} can be attributed to the creation of few layer graphene. Previously these changes in the 2D band have been attributed to random stacking, as the expected AB Bernal stacking was not seen.[82] For ML-graphene and mesographene the highest intensity of the 2D band is observed at 2681 cm^{-1}, a feature associated with AB Bernal stacking.[151] Substantial functionality is not observed from TGA, FT-IR, or elemental analysis for mesographene, despite a large increase in the I_D/I_G ratio. The synthesis of MWNTs from graphene by sonication has been shown to affect peak characteristics from Raman measurements.[154] To determine any change in curvature, the full width at half-maximum (FWHM) was determined for the G band and 2D of the precursors and obtained products and differences in values after sonication (**Table A4**). After sonication, mesographite had no change in the G band FWHM value. In contrast, the FWHM value of mesographene's G-band increased by 10 cm^{-1} and the 2D band FWHM increased by 14 cm^{-1}. These changes in FWHM values are similar to the differences observed in FWHM values for scrolled graphene which can form carbon nanoscrolls and nanotube structures.[155]

Low-Voltage TEM (LV-TEM) and Scanning TEM (STEM) analysis were performed to determine any changes in structural characteristics, such as curvature or edge folding. Monolayer and aggregated nanoscale graphenes have previously been observed showing centrifugation conditions can be altered to obtain size-specific material, confirmed by electron microscopy.[156] The as-synthesized mesographene solution was too concentrated to be centrifuged, therefore diluted solutions (< 0.01 mg/mL) were prepared. These solutions were centrifuged before LV-TEM analysis to confirm the production of few layered or monolayered graphene. LV-TEM images from the diluted solutions **(Figure 7)** reveal the presence of nanoscale graphene.

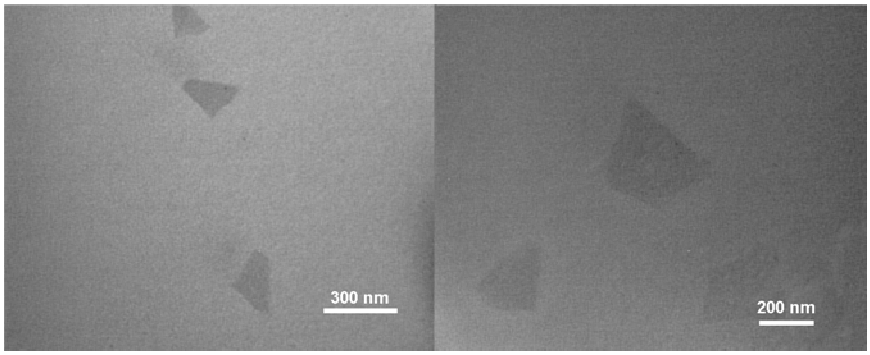

Figure 7. LV-TEM images of mesographene displaying nanolength sheets

Well-defined 2-dimensional sheets are visible with lengths of the order of 100 nanometers, in the range of 200 nm - 400 nm. Scrolled structures are not observed in these images, possibly removed during centrifugation.

Scanning TEM (STEM) was performed on un-centrifuged, concentrated dispersions of mesographene to observe any curved structures. STEM

micrographs (**Figure 8a-d**) indicate the presence of a variety of structures in bulk mesographene.

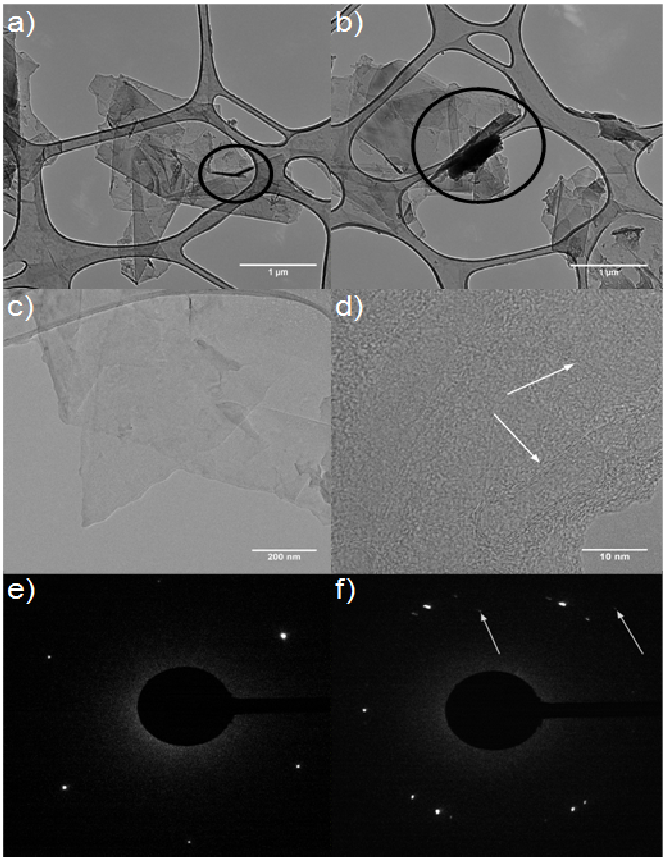

Figure 8. STEM images of a-b) mesographene with regions (black circles) containing curved structures with several layers, c) folded and wrinkled graphene layers, d) various carbon nanostructures trapped between layers (indicated by white arrows), e) SAED pattern from monolayer edge (beam incident along the [001] direction), f) SAED from the edge of aggregated few-layered graphene (beam incident along the [100] direction)

Large sheets with length scales larger than ~1 µm with curved edges can be seen (**Figure 8a-b**). Black circles indicate regions with possible tube-like structures containing several layers of graphene sheets, some greater than 1µm (**Figure 8b**). **Figure 8c** confirms the presence of folding, as large graphene

sheets with folded edges and small fragments of scrolled graphene trapped between layers can be seen. Upon further magnification, carbon nanostructures with tube-like and onion-like geometries (**Figure 8d**), which are indicated by white arrows, appear trapped between planar graphene layers. Using electron microscopy, similarly curved nanostructures were seen in samples of ball-milled graphite, scrolled graphene, and nanotubes made from intercalated graphite.[89, 144, 155, 157-162] The selected area electron diffraction (SAED) pattern **(Figure 8e)** from the sheet edge, confirms preservation of the hexagonal lattice with intense spots characteristic of monolayer graphene.[44, 79, 80, 163, 164] Fluctuation in spot intensities likely to be from wrinkled graphene sheets, which have been observed in monolayer graphene.[121] The SAED pattern of the edge of re-aggregated, few-layered mesographene sheets **(Figure 8f)** confirms rotational faults in the stacking order, suggesting AB Bernal stacking is not present[163] which conflicts with expected stacking concluded from Raman analysis. However sample preparation using solvent has been shown to effect stacking behavior and may account for this discrepancy, but edge domains in CVD synthesized graphene have produced similar SAED patterns.[82, 165] White arrows point to low intensity diffraction spots, which could possibly arise from (002) and (003) spot patterns found in analysis of isolated multi-walled graphitic tubes and graphitic allotropes with a variety of structures prepared by arc-discharge methods.[166, 167] Fragmented carbon and various other carbon structures could account for the

appearance of these spots, which cannot be determined simply by Raman and STEM analysis.

The XRD analysis of the powders provided information for determining changes in d-spacing as a result of sonication. Comparisons to the structural characteristics of graphite and graphitic oxides can be insightful, as thorough exploration to determine oxidation effects on interlayer spacing has been performed.[146] XRD patterns (**Appendix A, Figure 16**) of precursor and products show minor structural changes after processing. Using the Bragg equation, the d-spacing was calculated for each sample; d-spacing was 0.328 nm for precursor graphite and increased to 0.334 nm for mesographite. This change can be attributed to the exfoliation of graphite likely from edge functionality and intercalation. Precursor ML-graphene exhibited a d-spacing of 0.334 nm and for mesographene the d-spacing was determined to be 0.333 nm. From the Scherrer equation (adjusting FWHM values due to instrument line broadening), the average stacking height (L_c) of nanoscale (< 200 nm) materials can be calculated. Several groups have reported values for pristine graphites of various particle sizes, modified graphites, exfoliated graphites, and graphene.[89, 99, 124, 126, 146, 153, 157, 168-171] For our precursor graphite and graphene, L_c was found to be 10.0 and 7.3 nm, respectively. These values increased for mesographite and mesographene to 15.8 and 12.1 nm, respectively, as an increase in the crystallite size is observed. As graphite is oxidized, a decrease in crystallite size was observed resulting from surface oxidation.[146, 172] Thus we assume our

mesoscopic materials are likely only edge functionalized and that sonication removed any distortions on the surface. Using L_a values determined from Raman analysis and our determined L_c values, crystallite surface areas for the powders were determined. Consideration of these values must be taken qualitatively, as using XRD analysis to confirm the presence of structural curvature is difficult because distortions in graphitic samples directly affect the diffraction angles and FWHM values measured experimentally.[167, 168] Substantial increases in surface area are observed in both samples, likely due to loss of amorphous carbon. However these increases could be a result of curvature induced at edges, creating linked structures, thus increasing both lateral and stacking heights after processing.

The effect of the sonication procedure on conductivity, which can be greatly altered by changes in the chemical functionality and structural properties for graphitic materials, was analyzed using dielectric spectroscopy. Conductivity of the samples was measured by scanning different frequencies at room temperature, and calculated according to the following equation:

$$\sigma = l/ZA \quad (2)$$

where σ is conductivity (S/cm), l is the length of sample cylinder (cm), A is the cross section area of the sample cylinder (cm^2), and Z is the measured sample impedance (Ω). Conductivity measurements for all samples (**Appendix A, Figure 17**), including precursors, show a loss of conductivity resulting from sonication. The conductivity values are in good agreement with literature data for

electrical conductance of compacted graphite, especially if one takes into account that conductivity was measured along the compaction direction.[173, 174] The self-assembly of the fragmented mesoscopic products could account for variations in conductivity similar to the changes observed for deposited macroscopic thin films.[175] For isolated nanoscale products, nanographene and Sample 5 (NMP), the respective observed conductivities were less than that of mesographene. This decrease in conductivity has been reported for even slightly oxidized species, as sonication creates defect edges that further decrease conductivity. Compared to previously reported conductivities of chemically produced graphenes, both mesographene and mesographite exhibit similar values.[157] The conductivity of mesographene (Sample 4) is roughly 3 times greater than the conductivity of less-damaged nanographene (Sample 3), having a decrease in conductivity being a likely result of compaction causing increase in inter-junction sites for nanographene.

Also the mesoscopic products could potentially have conductivity affected by factors other than oxidation, as induced curvature and/or orientation between inter-junction sites caused by compaction. In a carbon nanotube and graphite interface, the orientation and structural characteristics of the materials were seen to affect conductivity.[176] Given that wrinkled functionalized sheets and capped carbon nanostructures are observed in the mesoscopic product, conductivity may decrease significantly due to the presence of curved species present on flake edges, creating poor inter-sheet junctions. Low conductivity has been observed

in graphene/graphite films and graphite (95 wt.%)/SWNTs (5 wt.%) and attributed to re-aggreagation effects after sonication, possibly generating unfavorable junction sites which increased resistivity of the films.[77, 177] Preservation of conductivity by improving contact between junction and interface sites requires further examination of self-assembly properties. By simple manipulation of synthesis conditions and/or post-processing methods, material resistance could be decreased.

Initially to understand solvent dispersion characteristics, experimental observations from carbon nanotube dispersions provided a starting point in determining graphene dispersibility.[134] To determine solvent stability of our mesoscopic samples, optical measurements of mesographene dispersions in both NMP and chloroform were analyzed in the UV-visible light range (**Appendix A, Figure 18**). Similarly, measurements to determine the absorption coefficients for mesographite in NMP and chloroform were performed as a comparison (**Appendix A, Figure 19**). Previous work has indicated that sonicated exfoliated graphite powder can be dispersed in NMP up to a concentration of 20 mg/mL, but centrifuged samples can be dispersed at concentrations of 63 mg/mL.[138] During sedimentation of inorganic nanowires, the concentration of dispersed material in solvent was approximated, and further expanded to graphene, using the equation,[78, 82, 138, 178]

$$C(t) = C_0 + (C_T - C_0)e^{-t/\tau} \quad (3)$$

which is defined by the stable dispersion concentration (C_0) and the initial concentration (C_T). For previously studied chloroform dispersions, a C_0/C_T ratio in the range of 0.67-0.96 was found for extensive time frames (11-19 hours).[82] For the mesographene sample, the stability was measured for specific concentrations (0.1 mg/mL) over a time frame of 6 hours to determine stability in short time for processing applications. The observed ratio was $C_0/C_T = 0.21$ indicating that the solution is not particularly stable, as large flakes sediment out fairly quickly. For mesographene, dispersed in NMP, the ratio was determined to be $C_0/C_T = 0.57$, meaning that large flakes are more readily stabilized in NMP and remain dispersed longer, which can be explained by different solvents having been shown to produce size-selected flakes with differing distributions in flake size and layers.[78, 82] For mesographene synthesized in NMP (Sample 5), dispersion of the product in chloroform gave an absorbance value (0.947 a.u.), slightly lower than the value (1.171 a.u.) from dispersed mesographene synthesized in chloroform. This difference indicates that solvent choice for exfoliation, which can affect nanoscale material properties, may not be observed when measuring the stability of mesoscopic solutions. Further exploration of the effect on these solution properties from the presence of nanoscale material is needed.

Absorption coefficients for dispersions in NMP and chloroform were determined at a specific wavelength for mesographene and mesographite (Figure A8), $\lambda = 660$ nm, to compare with reported values. Previously the

absorption coefficient, α, for size-selected flakes in NMP was determined, using Beer-Lambert's Law, giving α = 2460 mL mg^{-1} m^{-1},[77] and was later amended to incorporate variations in experimental conditions and reported as an invariant average value of α = 3620 mL mg^{-1} m^{-1}.[78] For mesographite and mesographene dispersed in NMP, the absorption coefficient values were α = 597 mL mg^{-1} m^{-1} and α = 1309 mL mg^{-1} m^{-1} respectively. Our values are lower, and while changes in experimental conditions can cause variability in these values, the difference in our values can be explained simply by the presence of larger flakes, which were not removed by centrifuging the solutions.[78] Absorption coefficients were also calculated for dispersions in chloroform with values of α = 610 mL mg^{-1} m^{-1} and α = 1173 mL mg^{-1} m^{-1} for mesographite and mesographene, respectively. Experimental α values for mesographite in both NMP and chloroform are quite similar ($\Delta\alpha \approx 13$ mL mg^{-1} m^{-1}), supporting previous reports that a single α value can be used for every solvent which is good for graphite dispersion.[77, 78, 80] The absorption coefficient for mesographene, for both NMP and chloroform, changed significantly ($\Delta\alpha \approx 136$ mL mg^{-1} m^{-1}) and suggesting much better dispersion in NMP.

The ability to disperse graphene in single solvent, surfactant/aqueous, and polymer/solvent systems requires overcoming the weak inter-sheet van der Waals forces. These dispersion systems have been experimentally explored extensively, and the governing solubility parameters for dispersion were thoroughly investigated.[77, 79, 80, 82, 132, 133, 135, 136, 179] The necessary solubility

parameters were determined, as the Hildebrand solubility parameter of δ_T ~ 23 $MPa^{1/2}$ and Hansen solubility parameters of δ_D ~ 18 $MPa^{1/2}$, δ_P ~ 9.3 $MPa^{1/2}$, and δ_H ~ 7.7 $MPa^{1/2}$ are reported for graphene. Hansen solubility parameters for the materials used in this study are provided (Table A6) and solvents listed in order by decreasing graphene dispersibility.[80, 82] Solvents chosen for dispersion were carbon tetrachloride, chloroform, acetone, NMP, toluene, and triethylamine (TEA). Mesographene products were dispersed using momentary sonication as no visible large particulates were observed, displayed in (**Figure 9**).

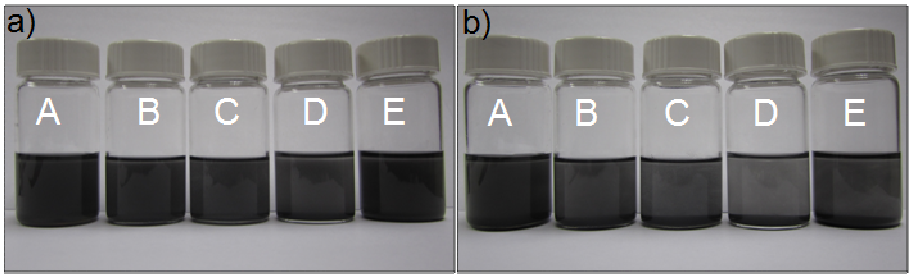

Figure 9. Mesographene dispersed at a concentration of 0.1 mg/mL in A) NMP, B) Chloroform, C) Carbon Tetrachloride, D) Acetone, E) Toluene shown a) initially, and b) after 1 hour

The dispersions of mesographene are visibly less transparent in comparison to dispersed mesographite solutions (**Appendix A, Figure 20**). The larger lateral starting size of graphite, as well as the 3-D behavior, confirmed the observed rapid sedimentation of mesographite compared to mesographene.

Optical measurements of mesographene and mesographite dispersions were performed using solvents with variable Hansen parameters (**Appendix A, Figure 21)**. The measured absorbance at λ = 660 nm, including the absorbance

ratios between both products, are given (**Table A7**). Two major factors for increased solvent dispersibility are: i) defect generation along flake edges due to sonication and ii) decrease in flake size during fragmentation. For the range of δ_D values assigned to graphene (15-21 $MPa^{1/2}$), all solvents have δ_D values which fall within the accepted range of dispersing graphene. Interestingly δ_P and δ_H values for carbon tetrachloride (δ_P = 0 $MPa^{1/2}$, δ_H = 0.6 $MPa^{1/2}$), toluene (δ_P = 1.4 $MPa^{1/2}$) and triethylamine (δ_P = 0.4 $MPa^{1/2}$, δ_H = 1.0 $MPa^{1/2}$) do not fall in the acceptable range of solvents capable of dispersing graphene, yet based on our results demonstrate good dispersibility. This suggests that the range of δ_D values for graphene dispersibility govern solvent dispersibility, consistent with other experimental results.[82] Differences in dispersibility between the mesoscopic products can be accounted for by the fragmentation of graphite creating chemical species primarily consisting of benzene, toluene, xylenes, and phenolic compounds[76], which we assume may have been trapped upon re-aggregation of product during filtration. The formation of decomposition and impurities was suggested to increase dispersibility in “poor” solvents, and upon addition of amphiphilic block copolymers, the stability between organic and aqueous phases was shown to be easily manipulated.[180] Hence these species could account for the improvement in dispersibility of mesographene in both acetone and toluene and the possible increase in π-π interactions, hydrogen bonding interactions, and/or presence of chemisorbed species.

Considering both chemical characterization and structural analysis, the presence of hetero-structures can be understood by understanding the associated chemistry of the sonication process. Sonochemical degradation of chlorinated solvents can generate various radical species, including chlorine radicals and even HCl while water has been known to form both hydrogen radicals and hydroxyl radicals.[141, 143] High-voltage (300 kV) high dosage electron irradiation of carbon soot for prolonged exposure times (≥10 minutes) has been reported to form curled and closed structures for graphitic samples.[181] Sonication of graphene oxide under strongly acidic conditions has been shown to produce carbon nanotubes, explained by acid induced condensation of sonication-induced formation of polyaromatic hydrocarbons.[144] Based on this information, a mechanism for the sonochemically induced functionalized and capped nanostructures in mesographene (**Figure 10**).

The initial introduction of chemical functionality from sonication occurs at flake edges (**Figure 10a**) and creates wrinkled 2-dimensional sheets with oxidized and chlorinated species. These wrinkled functionalized sheets upon further sonication (**Figure 10b**), which creates high temperatures and pressures ideal for fusing reactive fragments, can form closed 3-dimensional nanostructures in the presence of a strong acids, such as HCl. While this scheme provides a potential explanation for our observations, further experimentation is needed to confirm details of this process.

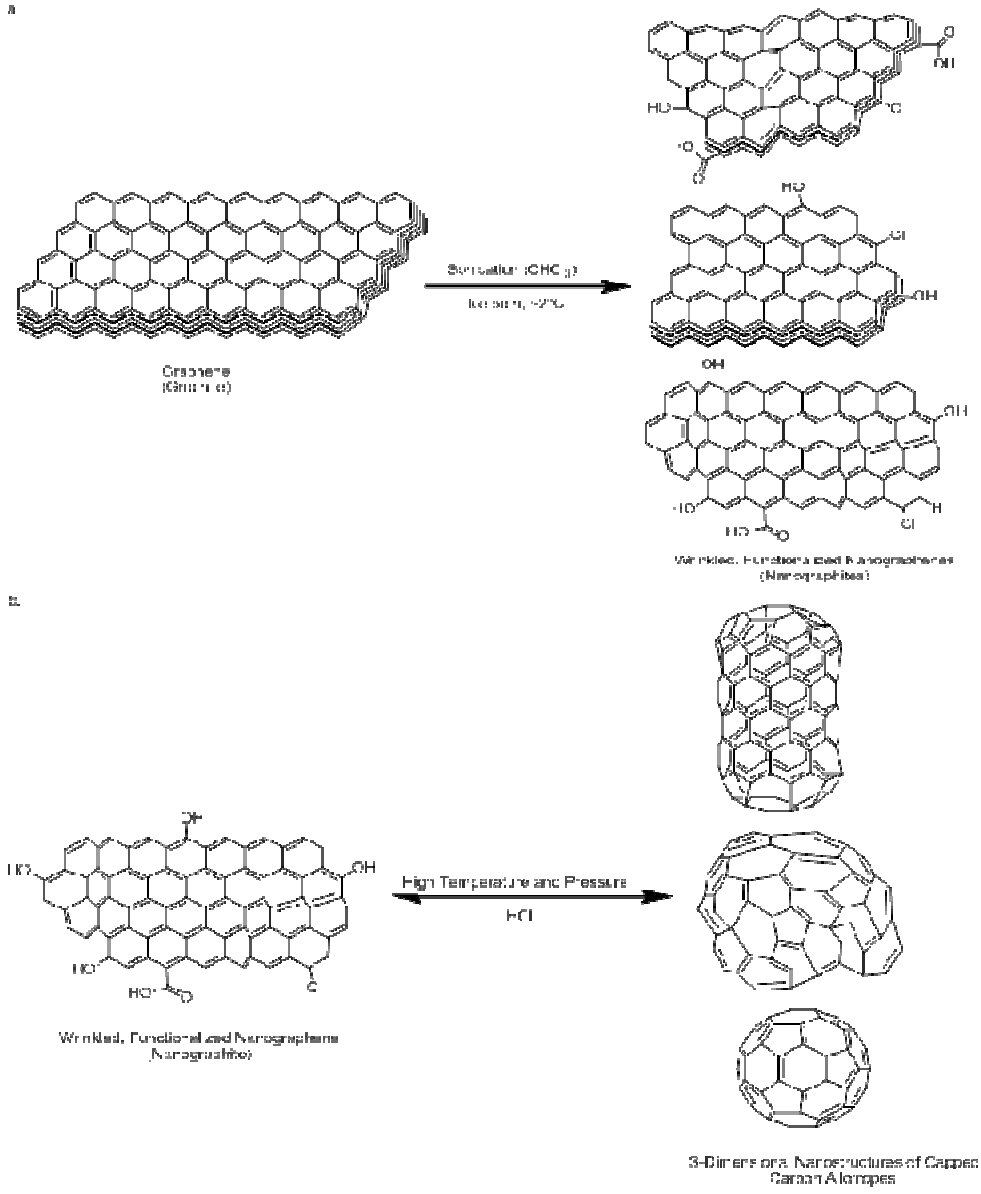

Figure 10. Postulated synthesis of carbon nanostructures in a two-step process generated during sonication by a) initial generation of curved and wrinkled functionalized layered and monolayer graphene and b) curved closed nanostructures formed by few-layered and monolayer sheets form various structures

Extensive research regarding polymer nanocomposites containing graphene, graphene oxide, and modified graphite has shown changes in polymer characteristics, including increases for thermal conductivity, electrical conductivity, mechanical properties, thermocalorimetric transitions, and gas permeability.[8, 98, 103, 182] Highly porous functionalized graphene sheets have been shown to increase the glass transition temperature (T_g) of poly(methyl methacrylate) by 30 °C.[99] To observe the effect on various polymer systems, we used both polar and non-polar polymers consisting of polystyrene (PS), poly(methyl methacrylate) (PMMA), poly(cyclohexadiene) (PCHD), and poly(4-vinylpyridine) (P(4-VP)). Mesographite was used due to low precursor cost and primarily layered structure. Thermal properties of polymer composites containing mesographite were measured using (DSC) and the glass transition temperature (T_g) recorded and compared to the respective neat polymer (**Figure 11**).

For polymer composites containing various percentages of mesographite as filler, a maximum in T_g was observed for all matrices containing 0.05 wt.% mesographite. The lack of smooth transitions in the T_g values as filler percentage is increased indicate likely aggregation of the filler during the "annealing" process of the 1st heating cycle. Therefore the percolation threshold for thermal reinforcement is either at 0.05 wt.% or lower. The largest increases in T_g values were noted for composites consisting of 0.05 wt.% in PMMA (ΔT_g = + 14 °C) and 0.05 wt.% in P(4-VP) (ΔT_g = + 5 °C). Upon addition of mesographite to non-polar

polymers only slight increases in T_g were observed, for 0.05 wt.% in PS (ΔT_g = + 2 ℃) and 0.05 wt.% in PCHD (ΔT_g = + 3 ℃). The low observed increases in T_g for the PS composites is not surprising, as for even covalently grafted graphite oxide increasing the molecular weight (from ~21k to ~81k) of PS decreased thermal confinement of polymer chains, lowering the increase in T_g values.[175] We expect that molecular weight as well as polydispersity can greatly affect the dispersibility characteristics during any thermal treatments, which can be manipulated by annealing conditions. Furthermore, solution-blended polymer nanocomposites consisting of low volume percentages of fragmented graphite sheets and polycarbonate (containing Bisphenol A)[117] displayed decreases in T_g, characteristic of poor interactions between the filler surface and polymer similar to our observations.

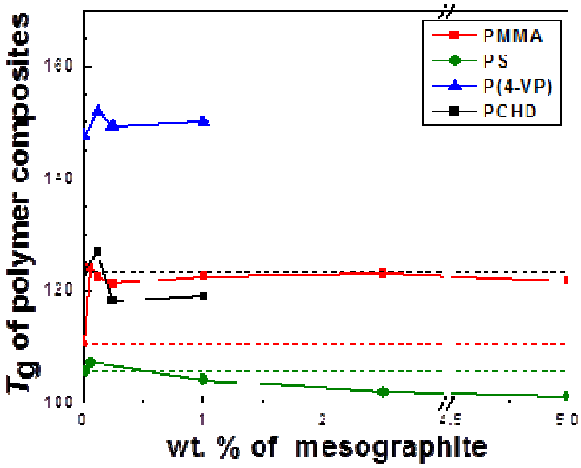

Figure 11. Plot of T_g values of neat polymers and solution processed composites as weight percentage of mesographite is increased (T_g of corresponding neat polymers are indicated by dashed lines)

Conclusions

Starting from commercial precursors, we employed a sonication-assisted exfoliation process to obtain large quantities of fragmented graphitic materials. Variations in chemical composition and induced sheet edge damage to the conjugated graphitic network were observed from Raman specroscopy, FT-IR, elemental analysis and XPS spectra. LV-TEM and STEM images of mesographene show the presence of heterostructures and fragemented sheets of nanoscale and micron lengths. High conductivity was observed for all the fragmented samples, and the excellent re-dispersion of the obtained macroscopic products was exploited as a simple route for polymer nanocomposite preparation. Thermal analysis of polymer composites containing mesographite showed that polymer chain mobility was enhanced in non-polar systems and inhibited in polar matrices. This method for sonication-assisted exfoliation of graphite could be further developed to create tunable and dispersible graphene-based materials in large quantities in order to facilitate their commercial application.

Appendix A

Bulk Fragmentation of Commercial Graphite and Multi-Layered Graphene Powders Using a Low-Boiling Point Solvent

Thermogravimetric Analysis (TGA)

To compare the thermal stability of these materials, maximum degradation temperatures were obtained, corresponding to maximum weight loss. Precursor graphite has a T_{max} of 691 ℃ (**Figure 12**), significantly less than reported values for graphite powder (< 20 μm), probably due to edge and surface oxidation.[153]

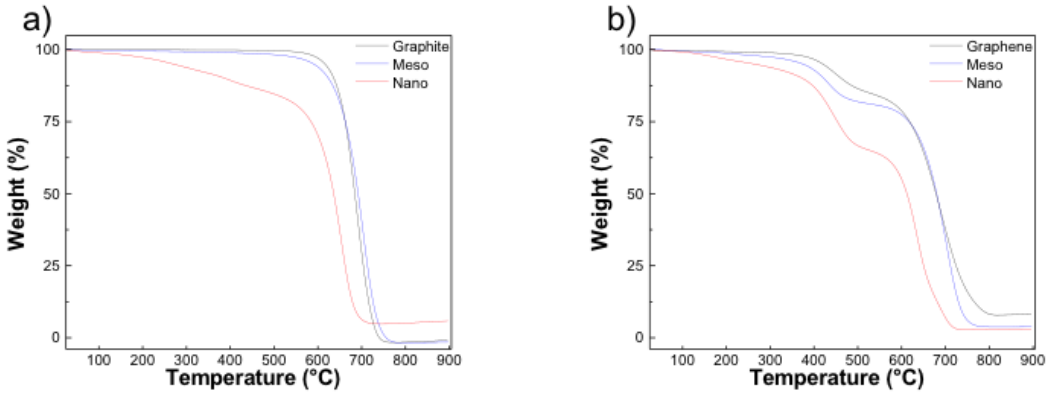

Figure 12. Decomposition profiles of a) graphite (black), mesographite (blue), and nanographite (red), b) graphene (black), mesographene (blue), and nanographene (red) heated in air

Nanographene exhibits a T_{max} of 710 ℃, ~20 ℃ greater than that of graphene, which could be indicative of nonintercalated/functionalized few layered and monolayered graphene, which has been attributed to enhancements in thermal

resistance.[183] Comparing weight losses of nanographene products synthesized in a different solvent, sonication in NMP (Sample 5) increased weight loss by 2.4%. This suggests that increased functionality may depend on solvent selection, but residual NMP could account for this increase as NMP has low volatility.[80]

FT-IR Analysis

FT-IR spectra of both mesographene and mesographite were measured in atmospheric conditions with precursor background subtraction in **Figure 13**.

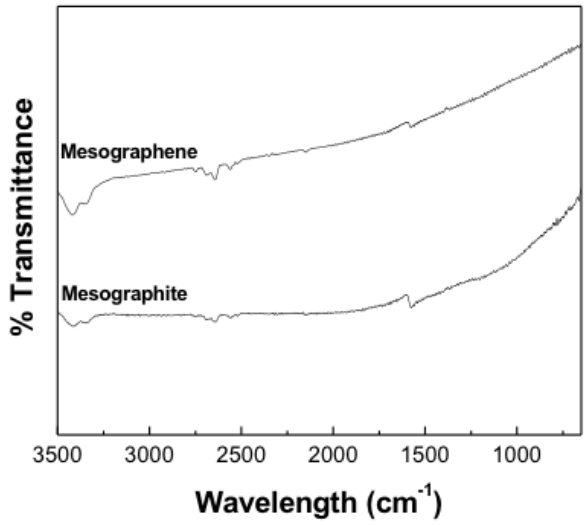

Figure 13. FT-IR spectra of mesographite (lower) and mesographene (upper) (after precursor background subtraction)

Elemental Analysis

Relative weight percentages obtained from elemental analysis and calculated atomic ratios are shown in Table A1.

Table A1: Elemental analysis of as-received ML-graphene and mesoscopic products

Sample	C [wt%]	O [wt%]	C/O [a)]	H [wt%]	Cl [wt%]	C/Cl [a)]
ML-Graphene	93.36	2.86	43.52	<0.5	<0.05	>5516.02
Mesographene	89.26	2.44	48.78	0.67	1.58	166.89
Mesographite	85.62	<0.5	>228.32	0.11	0.20	1264.68

[a)] The atomic ratios were calculated relative to measured percentages.

XPS Analysis

Survey spectra for both samples displays high intensity of the carbon signal, as expected. The small peak near the oxygen photoemission region observed in both spectra is attributed to the carbon ghost line. This peak is a result of small magnesium impurities in the aluminum anode and the very intense carbon signal. The offset of the signal is exactly 233 eV from the carbon 1s signal, confirming the presence of ghost lines. Peak positions were determined by referencing the C-C line to 284.4 eV (the known value for graphite) and shifting the entire spectra. The C 1s photoemission spectrum for graphite and mesographite were collected, and the C 1s line was fit with an asymmetric line shape, while the $\pi \rightarrow \pi^*$ shakeup was fit assuming a Gaussian shape, shown in **Figure 14**.

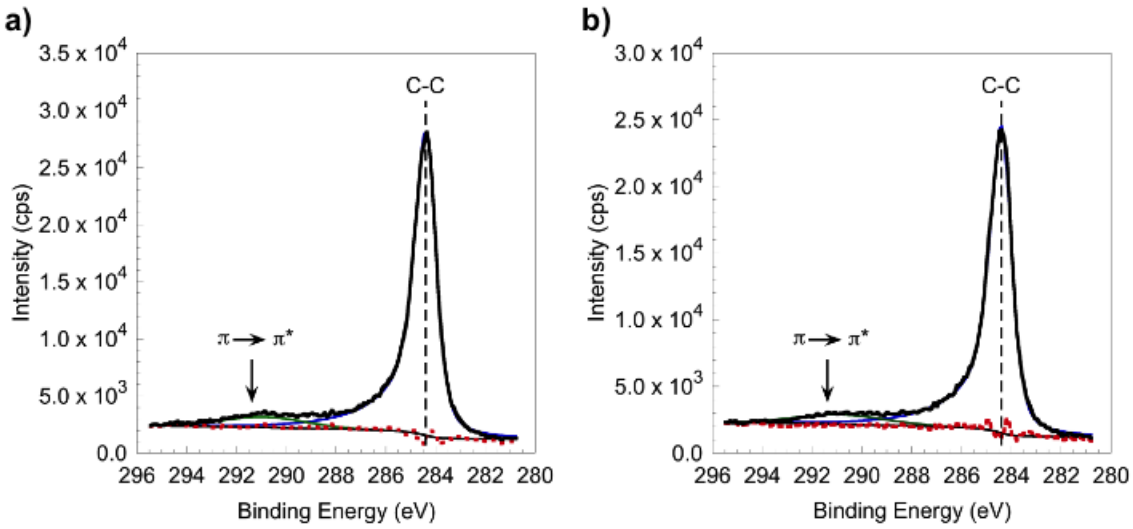

Figure 14. XPS measurements of C1s regions for a) graphite, b) mesographite

The shakeup was determined to be shifted approximately 6.5 eV higher than the C 1s line. This separation value and area ratio was kept for the sub-peak deconvolution of the graphite powder sample and the mesographite powder sample. The full width at half maximum (FWHM) for the C 1s line of the HOPG sample was 0.8 eV. A satisfactory fit was produced for the graphite powder and mesographite powder by using only the C-C sub-peak and the shakeup sub-peak. A very slight broadening of the C-C feature was observed (FWHM 1.0) and attempts to add a defect sub-peak or C-O bonding sub-peaks resulted in poorer fits. Because of the very low O/C ratio (< 0.035) and the tail structure of the C-C line, it is entirely plausible to assume that peak shifts, associated with C-O and C-Cl bonding, are consumed by the high binding energy side of the C-C line. For

both samples, the O1s photoemission regions were found, along with peak de-convolutions, in **Figure 15**.

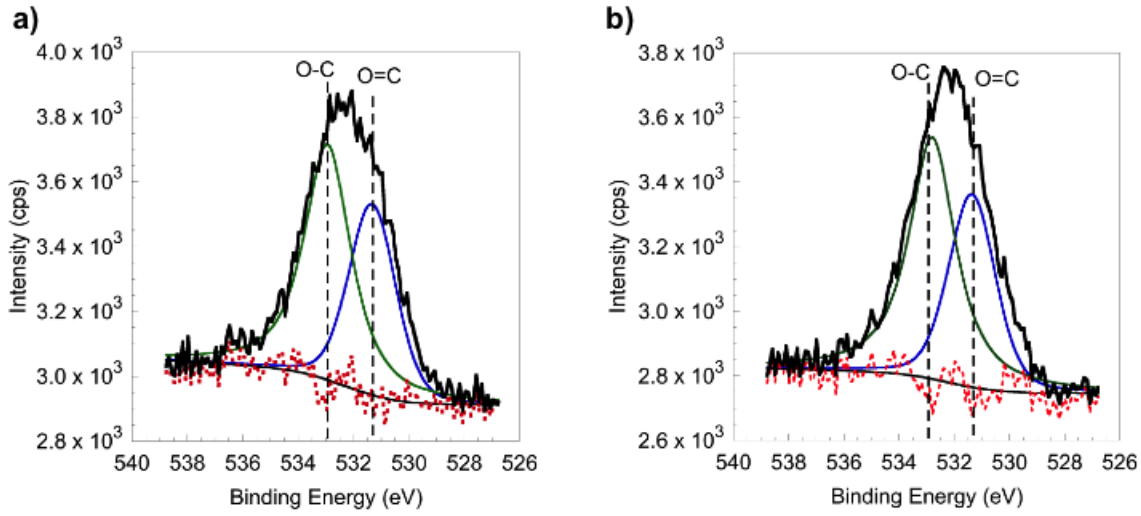

Figure 15. XPS spectra of O1s regions of a) graphite, b) mesographite with sub-peak deconvolution

The lower binding energy sub-peak is associated with oxygen doubly bound to carbon (O=C), possibly in an aromatic arrangement, and the high binding energy sub-peak is associated with oxygen singly bound to carbon (O-C).[184] The atom percentages of carbon, oxygen, and chlorine in graphite and mesographite, determined using both survey and multiplex measurements, are displayed in **Table A2**. The measured elemental compositions of the surfaces of the samples are similar to the values obtained from elemental analysis.

Table A2: XPS atomic percentages from Survey and Multiplex measurements for Graphite and Mesographite

Sample	Measurement	Carbon [at. %]	Oxygen [at. %]	Chlorine [at. %]
Graphite	Survey	97.1	2.9	0
	Multiplex	97.5	2.5	n/a
Mesographite	Survey	96.4	3.2	0.4
	Multiplex	96.6	3.0	0.4

Raman Spectroscopy

Table A3: Raman characteristics of precursors and mesoscopic products

Sample	G band			2D band		
	Position [cm^{-1}]	FWHM[a)] [cm^{-1}]	ΔFWHM [cm^{-1}]	Position [cm^{-1}]	FWHM[a)] [cm^{-1}]	ΔFWHM [cm^{-1}]
ML-Graphene	1578	29	10	2681	63	14
Mesographene	1580	39		2681	77	
Graphite	1567	20	0	2692	115	(-)20
Mesographite	1570	20		2661	95	

[a)] These values were calculated using single Lorentzian fits.

X-Ray Diffraction (XRD)

XRD patterns of powder samples are displayed in **Figure 16**. All samples displayed the signature [002] peak at 2θ= ~26.6°, corresponding to the interlayer distance (d-spacing) of ~0.335 nm between crystalline graphite sheets.[146]

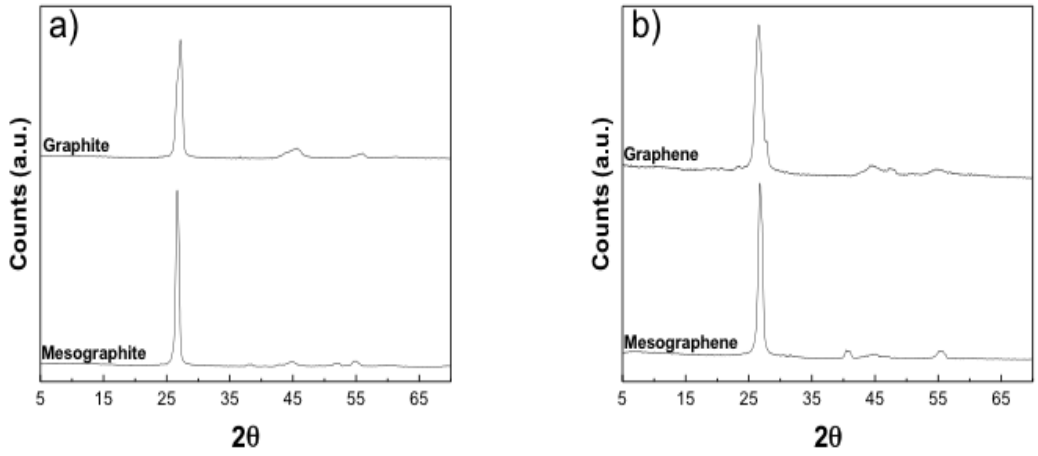

Figure 16. Powder XRD patterns of a) graphite and mesographite, b) graphene and mesographene

Determination of Crystallite Sizes

Using both L_a values obtained from Raman analysis and L_c values determined from XRD, crystallite size can be approximated, assuming the crystallites consist of hexagonally prismatic structure (Table A4). The equation used for determination of L_a was applied for a laser line wavelength of 514 nm.[152]

Table A4: Sample I_D/I_G ratios, corresponding experimental in-plane crystallite sizes (L_a) and surface area of crystallites

Sample	I_D/I_G Ratio	L_a [a)] (nm)	Surface Area [b)] (nm^2)
Graphite	0.14	5.0	158
Mesographite	0.18	5.7	278
Graphene	0.04	2.7	61
Mesographene	0.46	9.1	349

[a)] Determined using Eq. 1, where $C'_{(514\ nm)} \approx 0.0055$, [b)] Determined using the formula for the surface area of a hexagonal prism.

Dielectric Spectroscopy

Dielectric spectroscopy measurements were performed on the compacted powders by scanning the frequency range of 10^0-10^6 Hz (**Figure 17**).

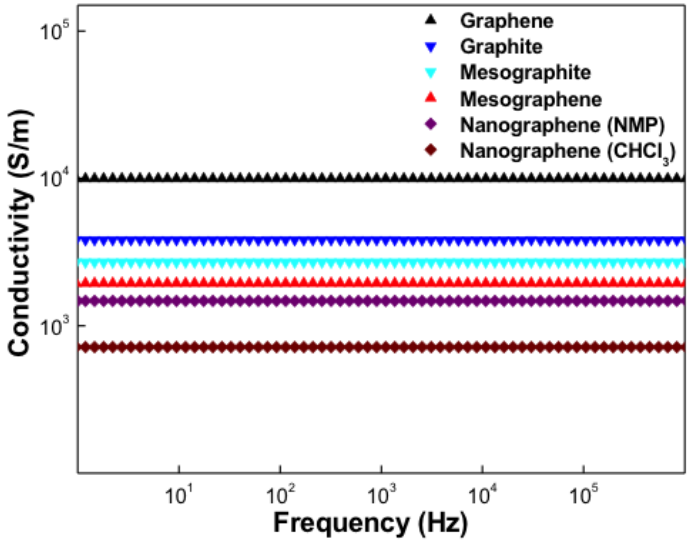

Figure 17. Conductivities of compacted powder samples

Optical Absorbance Measurements of Dispersions

Results of optical measurements to determine the stability of solutions of mesographene dispersed in NMP and $CHCl_3$, measured at λ = 660 nm, are displayed in **Figure 18**.

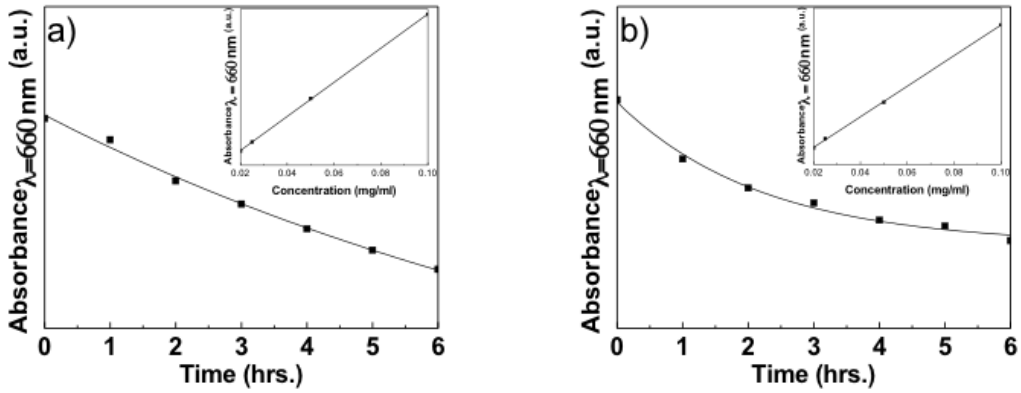

Figure 18. Stability curves of mesographene solutions at concentrations of 0.1 mg/mL in a) NMP (inset: linear absorbance at λ= 660nm for diluted solutions) and b) $CHCl_3$ (inset: linear absorbance at λ= 660nm for diluted solutions)

Determination of the molar absorptivity coefficient for mesographite dispersed in NMP and $CHCl_3$ was performed using the Beer-Lambert Law with absorbance values at λ= 660nm for various concentrations (**Figure 19**).

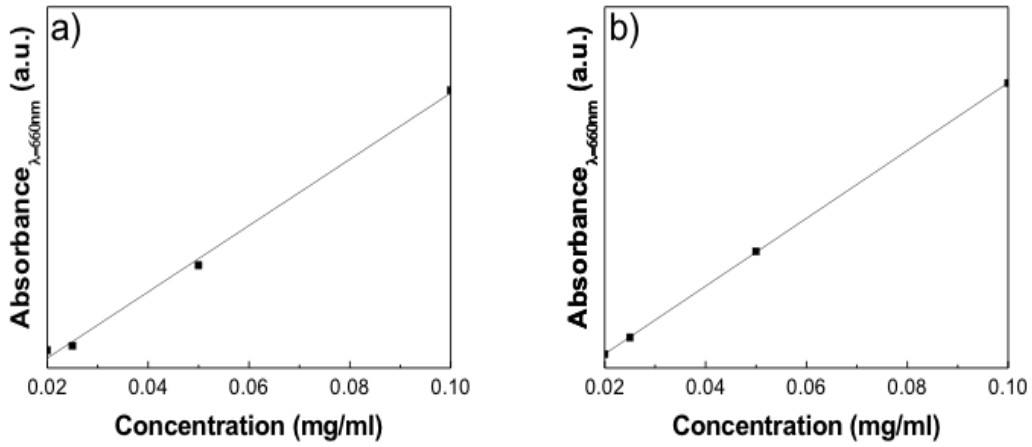

Figure 19. Plots of absorbance for λ = 660 nm vs. concentration (mg/mL) for mesographite dispersed in a) NMP and b) $CHCl_3$, upon dilution

The Hansen solubility parameters for solvents selected for this work are reported in Table A5. Recently, theoretical modeling applied to one and two-dimensional solutes was reported, giving a simple representation of the role of solubility parameters on miscibility, and concluding that δ_D and δ_P are the main governing parameters.[185] The effects of δ_H on miscibility are very specific to the chemical makeup of the dispersed material and the solvent, which complicates correlations between theoretical and empirical findings.

Table A5: Hansen solubility parameters for selected solvents and graphene

Solvent/Material	δ_D [MPa$^{1/2}$]	δ_P [MPa$^{1/2}$]	δ_H [MPa$^{1/2}$]
NMP	18	12.3	7.2
Chloroform	17.8	3.1	5.7
Acetone	15.5	10.4	7
Toluene	18	1.4	2
TEA	17.8	0.4	1.0
Carbon Tetrachloride	17.8	0	0.6
Graphene [a)]	18 (15-21)	9.3 (3-17)	7.7 (2-18)

[a)] Values in parentheses correspond to the acceptable range for solvents capable of graphene dispersion.

Photographs of vials containing mesographite dispersed in various solvents were taken at initial dispersion (**Figure 20a**) and one hour after being dispersed (**Figure 20b**).

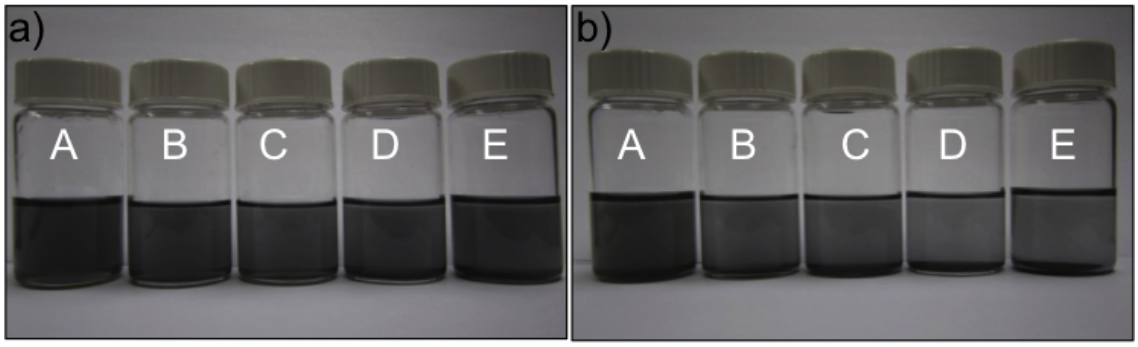

Figure 20. Photograph of vials containing mesographite dispersed at a concentration of 0.1 mg/mL in various solvents: A) NMP, B) Chloroform, C) Carbon Tetrachloride, D) Acetone, E) Toluene shown a) initially and b) 1 hour later

The optical absorbance spectra of both products dispersed in various solvents at similar concentrations are shown in **Figure 21**.

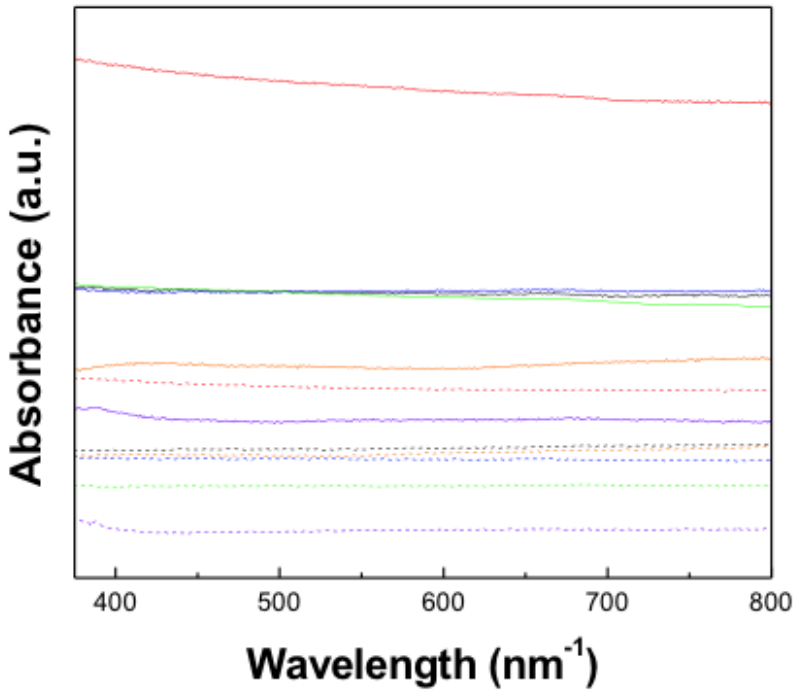

Figure 21. Absorbance spectra of a) mesographite (dashed), b) mesographene (solid), dispersed at equal concentrations (0.1 mg/mL) in various solvents: NMP (red), $CHCl_3$ (black), CCl_4 (orange), Toluene (blue), Acetone (green), and TEA (purple)

Despite being synthesized from different precursors, qualitative comparisons between the dispersibility of both mesoscopic products can be made. Dispersed mesographene exhibits higher absorbance in all solvents, likely a result of smaller flake size, higher purity, and more defect sites however structures observed by microscopy may also contribute to increased absorbance. Values for absorbance at λ = 660 nm for both samples in different solvents are shown in Table A6.

Table A6: Comparison of absorbance at λ= 660 nm for mesographene and mesographite in different solvents

Solvent	Mesographene[a)] [a.u.]	Mesographite[a)] [a.u.]	$A_{graphene}/A_{graphite}$ [b)]
NMP	1.146	0.629	1.8
Acetone	0.789	0.462	1.7
Toluene	0.805	0.508	1.6
TEA	0.578	0.385	1.5
Chloroform	0.797	0.528	1.5
Carbon Tetrachloride	0.673	0.522	1.3

[a)] Experimental values determined from optical measurements. [b)] Absorbance ratio at λ = 660 nm.

As expected, for both mesographene and mesographite, NMP was shown to be the most effective solvent for dispersibility. Noticeably, mesographene dispersions do not follow the trends observed for exfoliated graphite, as both acetone and toluene dispersions exhibit higher $A_{graphene}/A_{graphite}$ ratios compared to chlorinated solvents. Determining the ratio between the absorption coefficient values for mesographene and mesographite respectively, we found $\alpha_{graphene} / \alpha_{graphite} \approx 2$.

CHAPTER II
MACROSCOPIC PROPERTIES OF RESTACKED, REDOX-LIQUID EXFOLIATED GRAPHITE AND GRAPHITE MIMICS PRODUCED IN BULK QUANTITIES

A version of this chapter was submitted by Srivastava, V.K. *et. al.*:
Srivastava, V.K., et al. *Advanced Functional Materials*, **2014 (Accepted)**

The article was compiled and written by V.K. Srivastava. The reported synthesis and characterization was performed by V.K. Srivastava, except for XPS, Dielectric, and BET analysis.

Abstract

The excellent properties exhibited by monolayer graphene have spurred the development of exfoliation techniques using bulk graphite to produce large quantities of pristine monolayer sheets. Development of simple chemistry to exfoliate and intercalate graphite and graphite mimics in large quantities is required for numerous applications. To determine the macroscopic behavior of restacked, exfoliated bulk materials, a systematic approach is presented using a simple, redox-liquid sonication process to obtain large quantities of 2-D and 3-D hexagonally layered graphite, molybdenum disulfide, and boron nitride. The chemical compositions and self-assembly of the bulk 2-D and 3-D products were analyzed to correlate with measured macroscopic properties. Characterization by thermogravimetric analysis shows when MoS_2 is sonicated with sodium bisulfite, the obtained product retains roughly 54.0 wt.%, whereas MoS_2 sonicated without antioxidant retains only 15.2 wt.%. Results from Raman spectroscopy and x-ray diffraction and images from electron microscopy indicate the presence of distorted phases of different polymorphs, suggesting the formation of a Na_xMoS_2 compound and apparent nanotube structures in the bulk, restacked MoS_2. Using simple chemical methods, the ability to generate tailored multidimensional layered materials with unique macroscopic properties is critical for numerous

applications including electrical devices, reinforced polymer composites, lithium–ion capacitors, and chemical sensing.

Introduction

The discovery of single layer two-dimensional (2-D) atomic crystals of graphene by the simple Scotch-tape exfoliation method[17] has expanded the frontier of materials research and device applications.[12] Furthermore, the production of inorganic "graphene mimics"[16], including transition metal dichalcogenides and boron nitride, have recently received significant attention in the scientific community.[56, 94, 186] Graphene and the corresponding mimics exhibit excellent properties, including electrical, mechanical, magnetic, thermal, sensing, and lubricating behaviors, which have broadened the scope of research for viable chemical and physical methods to tailor material properties for these applications.[12, 14, 16, 18, 19, 25, 38, 45, 48, 56, 57, 93, 96, 101, 102, 107, 135, 187-190] A significant challenge has been producing large quantities of desired 2-D materials suitable for use in a broad range of applications. Only recently has ball milling emerged for producing large quantities of exfoliated and functionalized graphenes, but this exfoliation process requires complex equipment and conditions for reactions.[191, 192] A simple liquid exfoliation route to obtain monolayer graphene was developed to overcome the van Der Waals interactions in the layered precursor[77], and the governing parameters for exfoliation for the various liquids and graphene were explored.[80, 134] The extension of this exfoliation method to MoS_2[193] and BN[83] powders was recently reported[85], and both the utility and scope of this method

further pursued.[27, 86, 91, 190] However, despite the utility of sonication-assisted exfoliation, the addition of chemical reagents to generate new, unique materials has only just recently been explored with graphite as the inclusion of antioxidants produced nanotube structures[154] and large, pristine graphene sheets.[194] However only small quantities were generated and both processes required non-ideal reaction conditions (high solvent toxicity, exfoliation pre-treatment, intense sonication conditions, difficulty in reagent/solvent removal, etc.), thus requiring improvement of this exfoliation technique for scaling up the process and achieving changes in macroscopic properties.

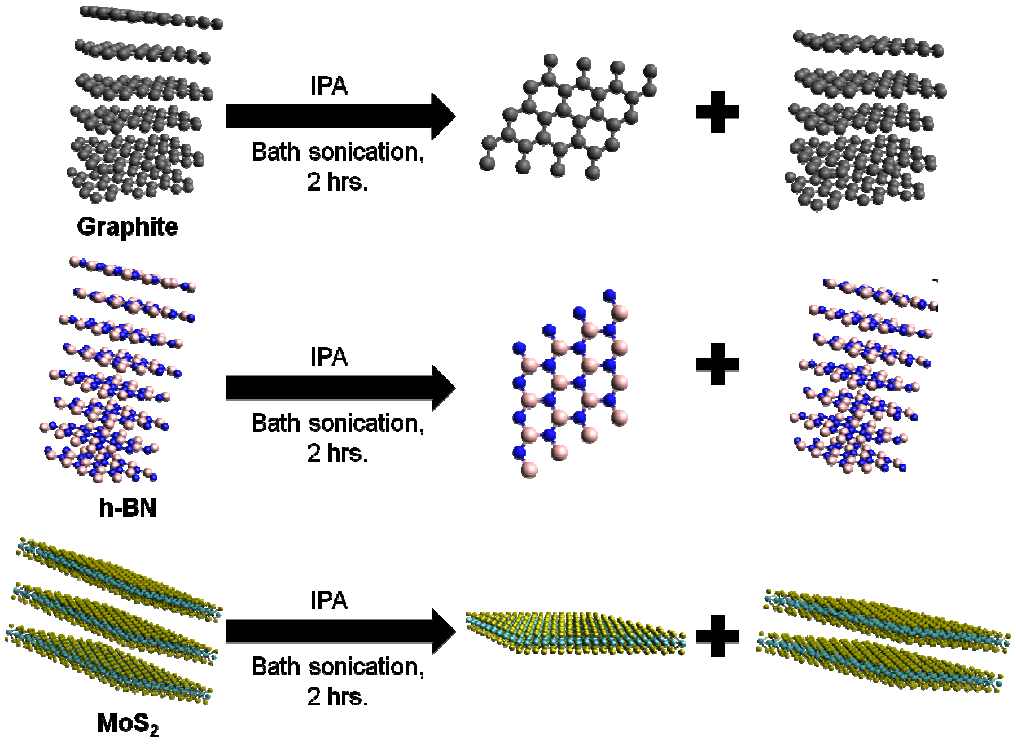

Figure 22. Proposed schematic of sonochemically produced 2-D and 3-D layered compounds in bulk samples

In this work, we present a facile, redox-liquid exfoliation method which produces high-yields of various 2-D and 3-D nanostructures using various antioxidants by mild sonication of 3-D precursor powders of graphite, molybdenum disulfide, and boron nitride in isopropanol (IPA). Extensive characterization was performed on the dried, restacked samples to d. To minimize errors in measurements, which were shown to greatly depend on sample preparation and handling,[86] homogenization of the samples after sonication was performed. Based on previous reports, the results of our exfoliation processes can be understood (**Figure 22**) using a chemical scheme.

Information including exfoliation conditions and antioxidant nature and concentrations are included (**Table B1**). Using various chemical exfoliation methods to chemically tune properties is still not yet understood thoroughly. Furthermore the effects of atmospheric oxygen on chemical and structural traits of these materials have not been systematically studied which can help facilitate the production of tailored materials. Investigating the effects of chemical and structural compositions of bulk quantities to observe macroscopic behavior could further broaden the utility of these materials for further chemistry and applications.

Results and Discussion

We prepared the 2-D and 3-D layered materials in high-yields using a simple sonication liquid- and redox-liquid exfoliation procedure. As edge

oxidation from sonication was determined to produce graphene from graphite[77], antioxidants were used (redox-liquid exfoliation) to minimize this affect. Previously the addition of antioxidant and a radical scavenger to pretreated exfoliated graphene generated, upon isolation, MWNTs[154] and large, pristine graphite sheets.[194] However, due to low yields the properties of these structures were not investigated further. As changing the dimensionality and scaling of these materials can greatly affect their respective electronic, mechanical, and lubricating properties[12], we analyzed the thermal, chemical, structural, and electrical behavior of the bulk exfoliated samples consisting of 2-D and 3-D layered materials.

Previously, large quantities of intercalated and exfoliated 2-D MoS_2 were produced using sodium napthalenide[92], however this method required an expansion treatment with hydrazine hydrate as a preliminary reduction treatment. Using a method to attempt to simplify the reduction and intercalation process of MoS_2, the bulk sample was analyzed to determine the influence of redox-liquid exfoliation on larger quantities of MoS_2 mono- and multilayered sheets. Samples were physical mixed prior to analysis to promote homogenization. Thermal treatment of the precursor and exfoliated products was used to determine absorbed organics and changes in thermal resistance to oxidation. Thermogravimetric analysis (TGA) plots of the precursor and exfoliated MoS_2 samples (**Figure 23a**) demonstrated susceptibility to thermal oxidation in air.

The measured temperature at maximum weight loss, T_{max}, and residual weight percentages were obtained from the TGA curves (Table B1). For the control sample MS1, two minor thermal degradations (T_{min1} and T_{min2}) were observed at 475 °C and 382 °C respectively, likely a result of thermal oxidation. The TGA plot of MoS_2 exfoliated in the presence of sodium bisulfite, referred to as sample MS2, displayed enhanced thermal resistance to oxidation as initial oxidative degradation occurred at T_{min1} and T_{min2} values of 496 °C and 395 °C respectively. MoS_2 powder retained 3.0 wt.% upon oxidative degradation, but samples MS1, MS2, and MS3 retained residual weights of 15.2 wt.%, 54.0 wt.%, and 17.8 wt.% respectively, demonstrating decreased susceptibility to thermal oxidation. Comparatively, sample MS2 displayed significantly better resistance to thermal oxidation compared to the other samples.

TGA coupled with mass spectrometry (TGA-MS) measurements were performed in inert conditions (N_2) of the precursors along with corresponding ion (mass/charge) currents to observe evolved CO_2 (m/z=44) during the heating process from absorbed organic residues. Ultra-high purity N_2 gas was used to minimize the presence of absorbed or trapped O_2 gas to prevent oxidative combustion. TGA-MS plots (**Figure 23b**) of the exfoliated MoS_2 samples demonstrate the differences in thermal behavior. Ion current values and normalized ion current ratios were tabulated for comparison (**Table B2**). Precursor MoS_2 displayed a weight loss of 4.4 wt.%, indicative of some residual

impurities in the material. This may be caused by absorbed hydrocarbon/gaseous species or from oxidized edges or surface chemistry.

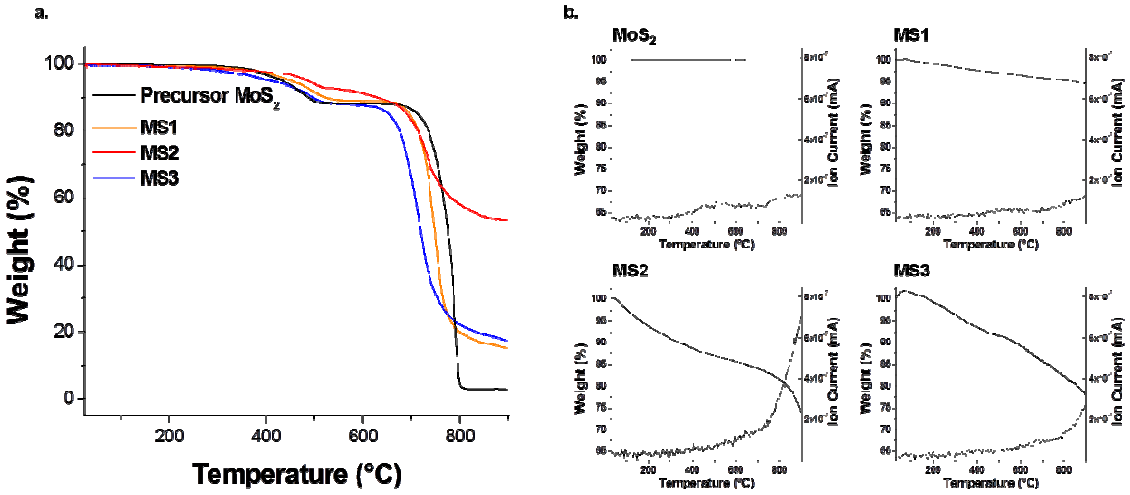

Figure 23. Results from thermal analysis a) TGA plot of precursor and exfoliated MoS_2 products (air); b) TGA-MS plots and measured ion currents (m/z=44) of precursor and exfoliated samples

Sample MS1 displays a loss of 5.3 wt.%, indicating retention of little organic/water residue, however much less than absorbed surfactant retained on exfoliated MoS_2 nanosheets.[87] This is further supported by the value for the normalized ratio of ion current signals between both samples, (0.96), indicating that both samples produced roughly the same concentration of evolved CO_2 gas. Contrastingly, samples MS2 and MS3 exhibited significant losses of 26.2 wt.% and 21.9 wt.%, respectively. Interestingly, observing the evolved CO_2 gas signal ratios, substantially higher levels of evolved CO_2 were observed for both samples as compared to the precursor and sample MS1. While increased trapped CO_2 gas may contribute to these increases, the significant formation of CO_2 gas

occurs in the temperature range of 700 °C – 900 °C. This increase could be from trapped gas or small organic molecules, but likely reflect the presence of a large oxygen containing species such as polymer. Significantly, for sample MS2, the released CO_2 gas increased by nearly 5 times compared to precursor MoS_2. As nanoscale MoS_2 has been shown to photo-oxidize alcohols[195], introduction of sodium bisulfite could possibly inducing the polymerization of the gaseous, oxidized isopropanol, similar to the behavior of sodium bisulfite in redox polymerization.[196] Recently, using isopropanol as a gaseous organic precursor, a technique referred to as plasma-enhanced chemical vapor deposition (PECVD) was used to make polymer films, formed as colliding electrons generating free radicals.[197] Similarly, sonication generates radical species, which could include the oxidizing H_2O_2 species observed in the degradation of *tert*-butanol[198]. In the presence of TEMPO, radical species could be stabilized which accounts for the calculated normalized ion current ratio of 1.87 obtained for sample MS3. TEMPO has been shown effective in trapping initiated radicals and would compete against oxygen for radical recombination reactivity.[199] Therefore we suggest that for samples MS2 and MS3, sonication could have possibly induce a “controlled” radical polymerization process, which has even been observed from simple pyrolysis of isopropanol.[200] Also previously exfoliated MoS_2 was found to display characteristic catalytic dehydrogenating behavior, due to dissolved oxygen gas likely generating edge oxidation.[201] Therefore as sample MS3 was exfoliated with TEMPO, isopropanol may be oxidized to aldehydes or ketones/carboxylic acids

similar to the catalytic oxidation of alcohols by TEMPO and a dehydrogenating metal catalyst, such as $RuCl_2(PPh_3)_3$, in the presence of O_2.[202] Therefore the conditions used to exfoliate sample MS3 may enhance the catalytic behavior of MoS_2.

Surface and edge chemistry can be greatly affected by the exfoliation process, and the precursors and exfoliated products were analyzed by X-ray photoelectron spectroscopy (XPS) to determine surface functionalities. Results from XPS measurements on exfoliated MoS_2 products (**Figure 24**) display signature peaks for Mo^{4+} assigned to the 2H-MoS_2 structure. Atomic percentages from multiplex measurements attributed to surface compositions were also determined (Table B3). The peaks of the Mo $3d_{5/2}$ and Mo $3d_{3/2}$ were seen at ~229.8 and ~233.0 eV, respectively, for all samples, slightly upshifted from reported results.[203] The characteristic S $2p_{3/2}$ and S $2p_{1/2}$ peaks also can be seen for each sample at ~162.6 and ~163.8 eV, respectively. The apparent lack of 1T-MoS_2 species in each sample were observed, in agreement with previously reported results.[33] The S 2p peak at ~167 eV corresponding to SO_3^{2-} and SO_4^{2-} ions was not seen for sample MS2, confirming no residual bisulfite. Measurements of C1s and O1s spectra indicated the presence of organic moieties in the exfoliated MoS_2 products. MS1 exhibited three C1s sub-peaks at ~285.0, ~286.3, and ~289.1 eV which represent likely adventitious carbon, C-OH or C-O-C, and C(=O)OH or O-C-O functionalities, respectively. The O1s spectra contained a sub-peak at ~531.3 eV which could be from C=O functionality or

possibly the presence of MoO_2 which has previously demonstrated an O1s sub-peak at 530.7eV.[204] For samples MS2, the C1s peaks indicate the possible presence of a surface film composed primarily of carbon species. However, the O1s peak was found to contain two sub-peaks at ~531.9 and ~533.5 eV attributed to various C-O species. Expectedly, sample MS3 exhibited C1s peaks (~285.0, ~286.5, and ~289.2 eV) and O1s peaks (~531.6 and ~ 533.3 eV) at the similar peak values seen for MS2. Qualitatively comparing the differences between the peak values of MS2 and MS3, the changes likely arise from lower concentration of oxidized carbon species in MS3.

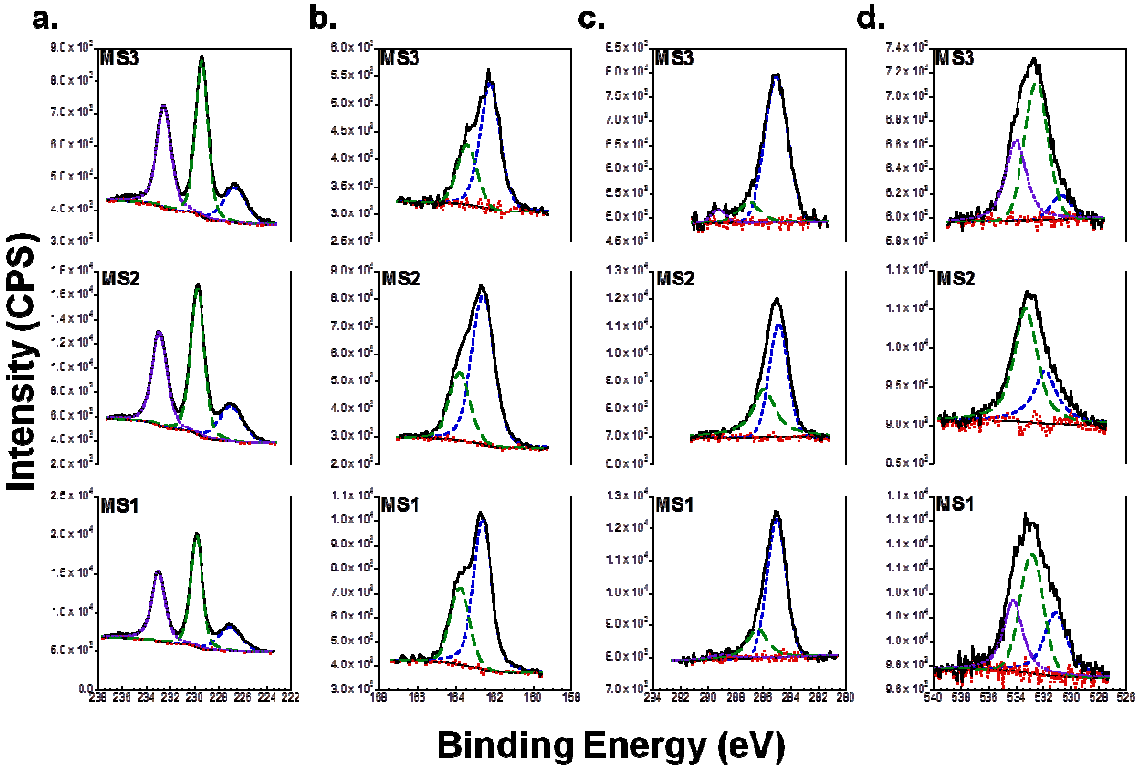

Figure 24. XPS plots of a) Mo3d, b) S2p, c) C1s, and d) O1s signature peaks for the exfoliated MoS_2 samples

The ATR-FTIR spectrum of precursor MoS_2 (**Appendix B, Figure 34**) powder is similar to that of dried MoS_2.[41] After sonication, the exfoliated sample MS1 displays similar peaks, slightly more intense than those of the precursor powder. A new peak of broad intensity is observed at 1732 cm^{-1} representing –C=O stretching expected from oxidation of isopropanol to acetone during pyrolysis.[200] The broad peak at 941 cm^{-1} corresponds to terminal –Mo=O bonding[205] due to potential oxidation. This is further supported by the sharply intense peaks at 730 cm^{-1} and 717 cm^{-1} characteristic of –Mo-O vibrations.[206] A similar spectrum was observed for sample MS3 indicating the presence of –Mo=O and –Mo-O bonding. For MS2, new peaks are seen at ~2949 cm^{-1}, ~2867 cm^{-1}, ~1376 cm^{-1}, ~997 cm^{-1}, and ~973 cm^{-1}, and the peaks previously assigned to surface oxidation are not observed. The -C-O stretching peak appears at ~1166 cm^{-1} and is more easily observed compared to samples MS1 and MS3. The peaks at ~2949 cm^{-1} and ~2867 cm^{-1} indicate new –C-H stretches, and the sharp peak at 1457 cm^{-1} indicates a single $–CH_3$ stretch. The high intensity peak at ~1376 cm^{-1} likely is from sulfonic/sulfate species generated from thermal degradation of sodium bisulfite.

Raman spectroscopy was performed on the samples to determine structural changes and the number of layers of the aggregates (**Appendix B, Figure 35**). Noticeably, precursor MoS_2 exhibited A_{1g} and E^1_{2g} modes (corresponding full-width at half maximum (FWHM) values are given in parentheses) of 406 cm^{-1} (5.2 cm^{-1}) and 381 cm^{-1} (5.3 cm^{-1}) respectively,

corresponding to the wavenumbers seen previously in bulk crystalline MoS_2.[207] Phonon confinement from small sheet sizes or defects in structure could account for precursors displaying various values for the A_{1g} and E^1_{2g} modes and their respective peak broadenings.[208] After exfoliation, both modes were observed to have shifted downfield, and the corresponding FWHM values changed as well. For sample MS1, the A_{1g} and E^1_{2g} modes were seen at 403 cm^{-1} (6.2 cm^{-1}) and 377 cm^{-1} (5.0 cm^{-1}), suggesting a decrease in layers (based on the increase in the FWHM value of the A_{1g} mode), previously observed for sonication-assisted exfoliated samples.[85] Raman analysis of sample MS2 exhibited A_{1g} and E^1_{2g} modes at 404 cm^{-1} (6.6 cm^{-1}) and 378 cm^{-1} (5.8 cm^{-1}) respectively, while sample MS3 showed A_{1g} and E^1_{2g} modes at 404 cm^{-1} (6.2 cm^{-1}) and 377 cm^{-1} (5.4 cm^{-1}), respectively. Sample MS2, displayed a peak of significant intensity at 283 cm^{-1}, characteristic of the E_{1g} mode of MoS_2 which is considered forbidden in Raman backscattering if the sample surface is perpendicular to the c-axis.[208] Considering that this peak only arises if the laser light is p-polarized[209], we believe the observed E_{1g} mode results from the incident light scattering parallel to edges of sheets or c-axis oriented sheets. Also observed in the Raman spectra of MS2 was a broad peak at ~330 cm^{-1} previously reported for exfoliated monolayer MoS_2[210]. This corresponds to the Raman active J_3 peak in 1T-MoS_2 (not observed in 2H-MoS_2) which was present in the Raman spectrum of exfoliated lithium intercalated MoS_2 sheets.[203] The appearance of this peak suggested that

sodium ions are intercalated between the MoS_2 layers forming the 1T-MoS_2 structure.

The powder X-ray diffraction (XRD) pattern of MoS_2 has been known to display various peaks based on sample purity, structure, processing (heating), exposure to air, and other factors.[211-214] However, a peak of high intensity should be visible, assigned to the (002) peak of 2H-MoS_2.[214] The (002) Bragg peak should be observed in bulk MoS_2 at $2\theta \approx 14.8°$, which can be used to determine d-spacing along the c-axis. Interestingly, the obtained XRD pattern of precursor MoS_2 powder (**Appendix B, Figure 36**) does not show this characteristic peak. To determine if water or any other contaminants affected the measurement, the precursor was vacuum-dried at 200 ℃ for 14 hours but still did not display the characteristic (002) peak. The presence of sample impurities and structural heterogeneity of the precursor could account for the observed for the lack of the (002) peak and suggests highly disordered or amorphous material. However for both the precursor and dried precursor, broad peaks centered at $2\theta \approx 47°$ were observed likely due to trapped water between layers.[214] The characteristic (002) peak was observed for sample MS1 at $2\theta \approx 14.52°$, corresponding to a d-spacing along the c-axis of ~0.609 nm, slightly less than the spacing of pristine MoS_2.[203] This decrease could arise from removal of impurities and trapped water after exfoliation. Samples MS2 and MS3 displayed (002) peaks at $2\theta = 14.36°$ and $2\theta = 14.39°$, respectively. From these peaks, the d-spacings calculated for MS2 and MS3 were ~0.616 nm and ~0.615 nm, respectively, indicative of better

exfoliation. The FWHM values for the (002) peaks of MS1, MS2, and MS3 were found to be 0.38°, 0.24°, and 0.20° respectively (± 0.01°). We assume the lower FWHM values for MS2 and MS3 (in comparison to MS1) arise from either distortions from the presence of MoS_2 polymorphs or increased crystallite size.[211] MS1 displays a broad peak (doublet) at $2\theta \approx 28°$-29°, possibly from water[214] or from molybdenum oxides.[204] Interestingly a peak at $2\theta \approx 36.2°$ (d-spacing = 0.248 nm) is also present which could be from the hydroxylated MoO_xH_y phase[204] and/or the presence of molybdenum (IV) dioxide (MoO_2).[215, 216] Also visible in the XRD pattern are the (100), (103), (105), and (110) peaks and various other 2H-MoS_2 reflections.[42] The presence and intensity of these peaks are distinguishable from those observed for the 3R-MoS_2 structure[212], which are observed in the XRD patterns. Sample MS1 displays the (100), (103), (105), and (110) peaks of the 2H-MoS_2 structure of much higher intensity compared to samples MS2 and MS3. Previously this has been characteristic of better rotational ordering[214], but structural variation would also affect signal intensities. Furthermore MS2 displays the lowest peak intensities and corresponding FWHM values were assigned to the 2H-MoS_2 structure, which potentially could result from sample heterogeneity due to the presence of the rhombohedral (3R-MoS_2) polymorph structure. The (103) peak of the 2H-MoS_2 polymorph appears as a doublet of low intensity, which could be assigned to the (104) and (105) peaks of the 3R-MoS_2 polytype.[212] The presence of these peaks could arise from stacking disorder from inorganic fullerene (IF-MoS_2) or nanotube (INT-MoS_2) structures, but chemical

intercalation of sodium ions would also distort the hexagonal structure of layered MoS_2 to form 3R-MoS_2 polymorphs.[92] Therefore the structural behavior observed by XRD must be further correlated to electron microscopy.

Further observations to changes in structure were obtained using high resolution-transmission electron microscopy (HR-TEM) micrographs and selected area diffraction (SAED) patterns of MS1, MS2, and MS3 (**Figure 25**). A caveat of TEM analysis is the consideration of knock-on damage from electron irradiation of the samples. At specific operating voltages, knock-on damage can occur, thus creating topological defects and structural distortions which has recently garnered interest as a route for engineering new materials.[217] Defects generated by knock-on damage differed significantly between samples. HR-TEM images of MS1 exhibit transparent regions and layered sheets containing numerous layers, but interestingly the SAED pattern for MS1 indicates distortions in the hexagonally structured crystallinity[218], similar to the SAED pattern of G1 (Figure B9c, Supporting Information) and possibly resulting from amorphous material at folded edge boundaries.[219] For MS2, ripples are observed in the aggregated sheets similar to those seen in monolayer samples[219] and edges appear to contain tube-like structures as suggested from XRD. The corresponding SAED pattern displays bright intensity spots characteristic of rotationally stacked aggregates demonstrating highly ordered hexagonal crystalline domains, as seen in exfoliated few layer or monolayer MoS_2.[87, 203] The HR-TEM images of MS3 display ordered crystalline layers similarly seen for G3

(Figure B9g-h, Supporting Information), however the SAED pattern displays no hexagonal symmetry of the (001) diffraction spots but displays high intensity (110) spots indicative significant stacking faults along the edges of the layered sheets.[218] The corresponding SAED patterns clearly display the differences in the stacking order of flake aggregates.

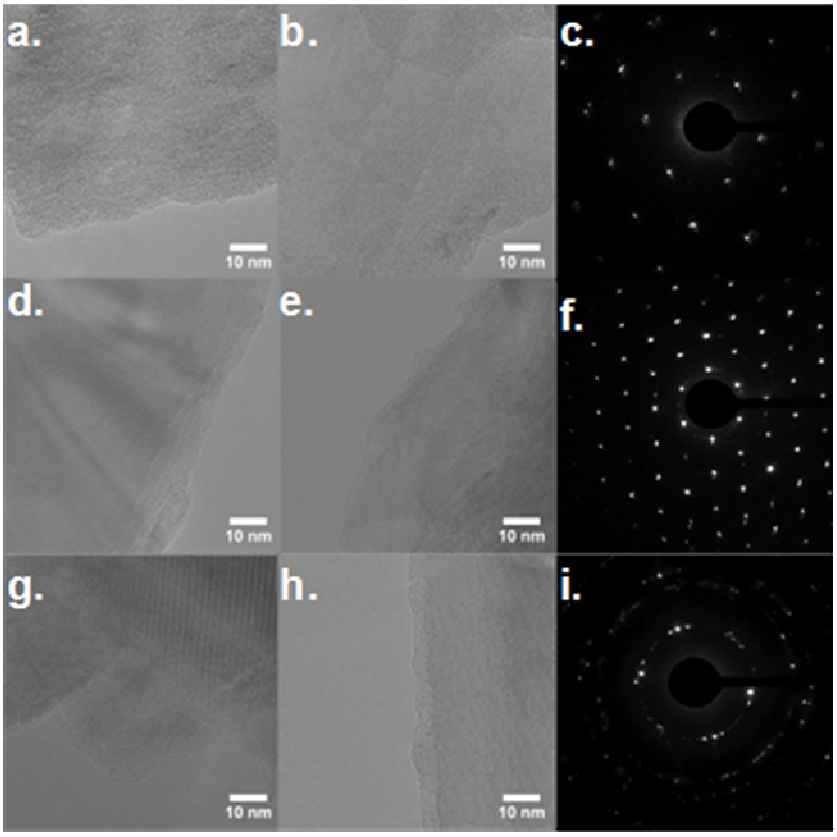

Figure 25. HR-TEM micrographs of a-b) MS1 (c: SAED pattern), d-e) MS2 (f: SAED pattern), and g-h) MS3 (i: SAED pattern)

Scanning electron microscopy (SEM) images of the exfoliated MoS_2 products (**Figure 26**) display large-scale variations in flake size and structure. The images were obtained from solutions of dispersed exfoliated MoS_2 products

of similar concentrations drop cast onto carbon grids. Fragmented sheets containing numerous layers are visible, all of which display lateral lengths (*<l>*) of *<l>* ≤ 2µm. A majority (~85%) appeared to have lateral lengths corresponding to *<l>* ≤ 1.5µm, indicative of the edge fragmentation process accounting for any nanoscale sheets. Each sample contains nanometer length fragments on the surfaces, although much smaller fragments are seen in sample MS2. Images of samples MS2 and MS3 exhibited less amorphous and more highly defined sheets as compared to those of sample MS1. The image of MS2 (**Figure 26c**) contains a multilayered sheet with folded layers and highly defined sheet edges. Overall, between samples, no major difference was observed for the number of layers of each crystalline sheet, but edge characteristics do appear to differ between the samples.

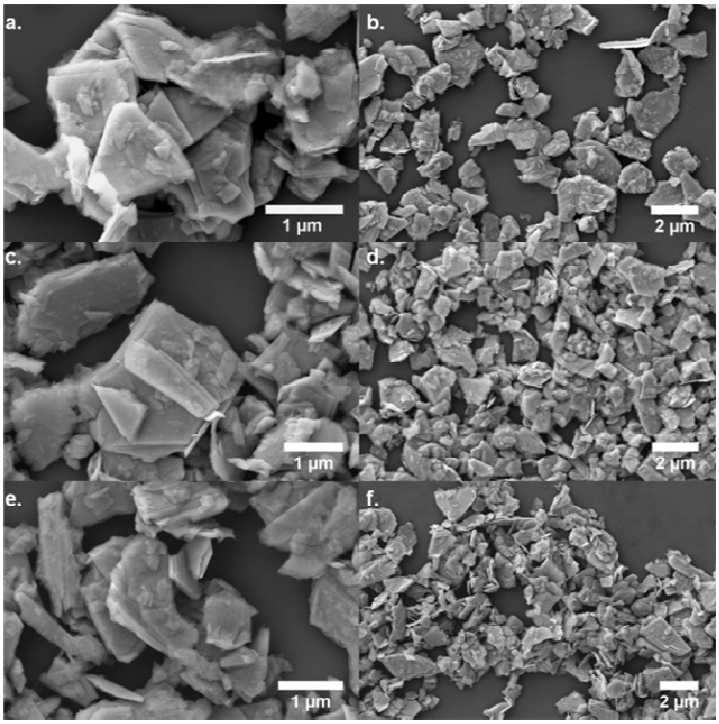

Figure 26. SEM images of exfoliated MoS_2 products: a-b) MS1, c-d) MS2, and e-f) MS3

A majority (~85%) appeared to have lateral lengths corresponding to $\langle l \rangle \leq$ 1.5µm, indicative of the edge fragmentation process accounting for any nanoscale sheets. Each sample contains nanometer length fragments on the surfaces, although much smaller fragments are seen in sample MS2. Images of samples MS2 and MS3 exhibited less amorphous and more highly defined sheets as compared to those of sample MS1. The image of MS2 (**Figure 26c**) contains a multilayered sheet with folded layers and highly defined sheet edges. Overall, between samples, no major difference was observed for the number of

layers of each crystalline sheet, but edge characteristics do appear to differ between the samples.

The dispersion characteristics of materials provide critical information regarding favorable solvating conditions and particle/liquid interactions. Optical absorbance (UV-Vis) measurements (**Figure 27**) of solutions were performed to compare differences in dispersability. The molar absorptivity coefficient, α_λ, was calculated using Beer-Lambert's law for diluted dispersions of samples G1, MS1, and BN1 in isopropanol (Table S4, Supporting Information). However these values should not be considered intrinsic to these materials, as variations in dispersed flake size can greatly affect the α_λ values,[86] and therefore considered a qualitative value. The α_λ values were determined at specific wavelengths, λ = 660 nm for G1, λ = 672 nm for MS1, and λ = 300 nm for BN1 to compare with previous reports.[85] Also molar absorptivity coefficients at 660 nm, $\boldsymbol{\alpha_{660nm}}$ (ml / (mg*m)), were calculated using Beer-Lambert's law for diluted dispersions of MS1 and BN1 in isopropanol**.** Since the precursor powder sizes are comparable (BN < MoS_2 < EG), as expected, we observed the inverse relationship regarding the molar absorptivity coefficients (α_{G1} (434) < α_{MS1} (1116) < α_{BN1} (1162)).

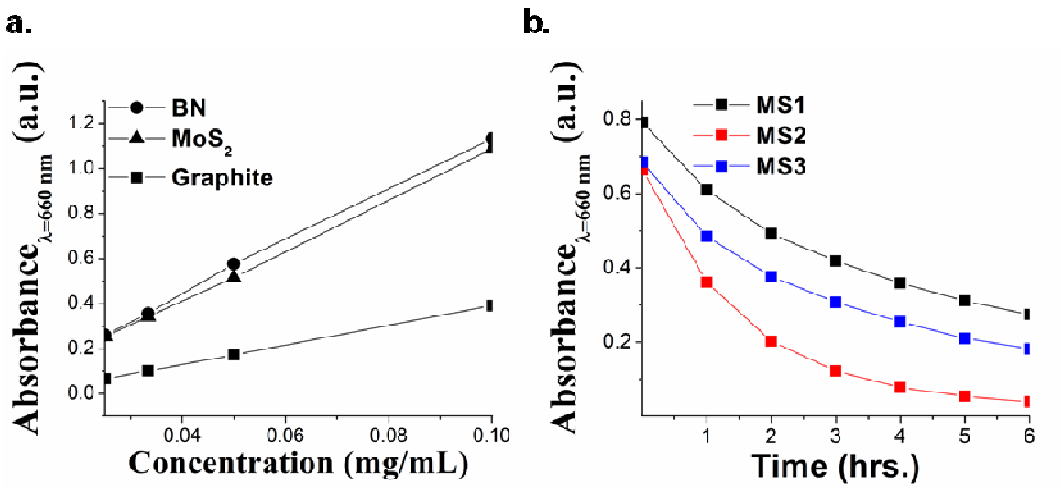

Figure 27. Optical absorbance for λ = 660 nm of a) Beer-Lambert plots for determining molar absorptivity coefficients in IPA and b) stability of exfoliated MoS_2 samples in $CHCl_3$

A significant difference between the exfoliated MoS_2 samples is noticeable when dispersed in chloroform (**Figure 27b**), as sample MS2 demonstrates significantly poorer stability compared to MS1 and MS3. Considering results from other characterization methods and the corresponding Hansen solubility parameters (Table S5, Supporting Information), decreased dispersion in $CHCl_3$ of sample MS2, which appears chemically more pristine but also appears to have some physisorbed ionized organic species, is not surprising. Another possible result may be enhanced ionic characteristic due to possible intercalation of sodium ions. Thus we believe the differences in polarity between the intercalated/exfoliated samples are even observable on the macroscale, resulting from synergistic chemical differences on the exfoliated (2-D) nanoscale sheets and bulk, intercalated samples.

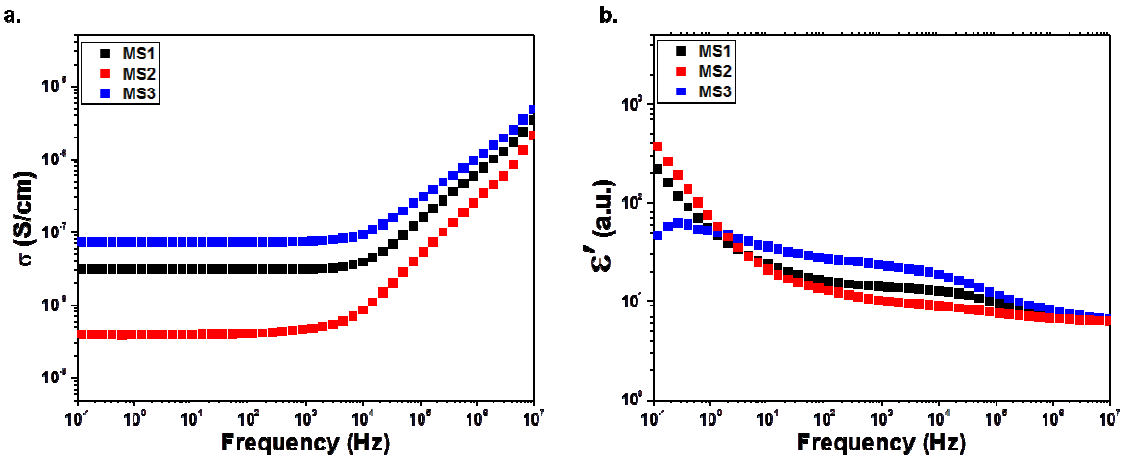

Figure 28. Dielectric measurements of a) D.C. conductivity, b) relative permittivity of the compacted exfoliated MoS_2 powders

D.C. conductivities and relative permittivities (**Figure 28**) of the macroscopic exfoliated MoS2 samples all displayed conductivities > 10-9 S/cm. Their respective conductivities are comparable to the measured conductivity of $3.6*10^{-7}$ S/cm obtained from monolayer/few-layer free standing MoS_2 films.[85] Sample MS3 exhibits the highest conductivity suggesting that the physisorbed species increased the semiconducting behavior, possibly from residual TEMPO generating a more highly polarized powder, which further may be highly oxidized. MS2 comparatively appears to be insulating, with lower conductivity (~ one order less) than both MS1 and MS3. Poor contact between layer edges from wrinkling/folding as seen by SEM (similar to sample G2), or carbon oligomer/polymer films would contribute to decreases in conductivity.

This lower conductivity could result from decreased presence of oxidative edge functionality reflected by the significantly larger dielectric constant of MoO_3

compared to the constant of MoS_2.[220] The relative static permittivity (dielectric constant) of each sample was ~ 6 a.u. which falls within the range of room temperature resistivity values for various MoS_2 samples.[221] The real part of the dielectric permittivity contains a step in the range of 10^4-10^5 Hz for all samples. Sample MS2 clearly has the smallest decrease in polarization whereas the biggest decrease occurs for sample MS3. We attribute this process to a Maxwell-Wagner-Sillars (MWS) polarization effect that arises due to sample heterogeneity, with a larger step usually indicating increased sample in-homogeneity.[222] As revealed by TGA-MS, XPS, and ATR-FTIR the presence of some amorphous polymeric residue in sample MS2 likely contributes to changes in the properties of the bulk powders. The weakness of MWS process for this sample probably comes from the fact that inclusions in this sample mostly consist of amorphous carbon/oxygen and hydrocarbon species (as concluded from TGA-MS, XPS, and ATR-FTIR data). This polymeric hydrocarbon and oxygen species is for the most part insulating and polar, similar to MoS_2 itself. As a result, there is not significant electric contrast between inclusions and MoS_2 sheets in sample MS2 leading to weak MWS polarization. On the other hand, the MS3 sample was exfoliated in the presence of TEMPO, which could have become trapped between layers, or even physisorbed to sheet edges.

This could enhance the MWS process due to increased dielectric contrast between the radical species and the exfoliated MoS_2. Various other factors could contribute to the MWS process due to the oxidation of isopropanol producing

carbonyl moieties such as aldehydes, ketones, and carboxylic acids.[202] Despite enhancing dispersion in polar solvents, the presence of these physisorbed polar moieties would inhibit conductivity.

Conclusions

Previous work has demonstrated the difficulties to obtain monolayer nanosheets exhibiting excellent properties from larger sized 3-D layered precursors. Using sonochemistry to perform redox-liquid exfoliation, we produced large quantities of graphite, molybdenum disulfide, and boron nitride consisting of 2-D and 3-D layered sheets and investigated the self-assembly of these materials. The characterization of the products also provided insight regarding chemical compositions and structures resulting from using specific precursors and reagents. For example, enhanced resistance to thermal oxidation of macroscopic redox-exfoliated MoS_2 was observed by simple *in situ* sonication with sodium bisulfite. Furthermore from Raman Spectroscopy and TEM images, the crystalline structure consisted of the 1T-MoS_2 polymorph likely resulting from intercalated sodium forming the Na_xMoS_2 compound. The simple production of chemically tailored nano- and microscale materials in large quantities could be exploited to generate novel materials of desired lengths and dimensions suitable for mechanical reinforcement, high-temperature, electronic, and dielectric applications.

Experimental Methods

Liquid-Redox Exfoliation of Bulk Precursors

The precursor powders of graphite (Sigma-Aldrich, synthetic < 20μm), h-BN (Sigma-Aldrich,< 1μm), and MoS_2 (Sigma-Aldrich,< 2μm) were used as received. The antioxidants 2,6-di-tert-butyl-4-methylphenol (Sigma-Aldrich, ≥99%), sodium bisulfite (Acros Organics, Analytical Grade), and 2,2,6,6-tetramethylpiperidine 1-oxyl (Sigma-Aldrich, 98%) and solvents 2-propanol (Fisher Scientific, Certified ACS Reagent Grade Plus ≥99.5 %) and chloroform (Fisher Scientific, Certified ACS Reagent Grade ≥99.8 %) were used without further purification. Solutions were made by adding of each respective precursor powder (10 mg) to glass vials containing fresh 2-propanol (10 ml). Antioxidant solutions were prepared by adding of 2,6-di-tert-butyl-4-methylphenol (1 mg) or of sodium bisulfite (10 mg), or of 2,2,6,6-tetramethylpiperidine 1-oxyl (10 mg), followed by vigorous stirring for 5 minutes prior to sonication. Subsequently, solutions were sonicated using a Fisher Scientific FS20H bath sonicator (~70W, 42 KHz) for 2 hours, while maintaining a constant water level and temperature ≤ 30 ℃. Due to larger quantities required for dielectric measurements and BET analysis, solutions containing 200 mg of precursor powders were made at similar concentrations as previously described. These solutions were sonicated using a Fisher Scientific F110 bath sonicator (~100W, 42 KHz) for 2 hours while maintaining a constant water level and temperature ≤ 30 ℃. After sonication, the solutions were then washed extensively with excess methanol. The solutions

were then filtered using a 0.22 micron filter (PVDF), and the obtained products dried for 14 hours under vacuum. The dried powders were then collected and analyzed.

Characterization Methods

TGA was performed using a TA Instruments Q-50 TGA (±2.0 wt.%). Samples were heated from 25ºC to 900ºC in the presence of compressed air (Airgas) at a flow rate of 40 mL/min. TGA-MS measurements were performed using a TA Instruments Discovery TGA-MS (± 0.1wt.%). Samples were dried with ultrahigh purity (UHP) N_2 (Airgas) for 15 minutes then subsequently heated from 25ºC to 900ºC in the presence of UHP N_2 (Airgas) at a flow rate of 40 mL/min. Ionization was performed using an electrospray source, and the masses of evolved gases measured from 1-300 amu using a Faraday cup detector. ATR-FTIR was carried out using a ThermoScientific Nicolet iS10 FT-IR Spectrometer equipped with a Smart iTR accessory. The XPS data were collected using a Physical Electronics model 5400 X-ray photoelectron spectrometer equipped with non-monochromatic Mg K_α (1253.6 eV) and Al K_α (1486.7 eV) X-rays. The data presented here were collected using the non-monochromatic Al K_α X-rays. The samples were mounted on the sample puck by placing a small circle of double-sided tape (< 1 mm diameter) on the puck and then pressing the powder down over the puck to cover the tape. A molybdenum mask with a 3 mm diameter hole was then placed over the powder and secured with screws. The samples were placed in the introduction chamber for approximately 15 minutes and then

transferred to the analysis chamber. The analysis area was set to 1.1 mm diameter spot size. During data collection, the analysis chamber pressure was approximately 1.0 x 10^{-9} Torr. Survey spectra were collected at low resolution, which corresponds to analyzer pass energy of 89.45 eV. They were collected in increments 0.5 eV/step and an integration interval of 50 ms/step. The complete spectrum consists of the average of 15 cycles. Multiplex spectra were collected at high resolution corresponding to analyzer pass energy of 22.35 eV with increments of 0.1 eV/step and an integration interval of 20 ms/step. Raman analysis was performed on powder samples using a JY-Horiba T64000 spectrometer using a 514 nm laser excitation (incident power ~0.5 mW), and a CCD detector. The instrument was calibrated using microcrystalline silicon (± 0.7cm^{-1}). Wide-angle powder XRD analysis was performed on powder samples in atmospheric conditions using a Panalytical Empyrean diffractometer equipped with a Ge monochromator using Cu-Kα (λ=0.1542 nm) radiation and a PIXcel^{3D} detector (±0.01°). Graphite and MoS_2 products were analyzed in the range of 2θ= 5°-70° (step size of 0.02°), and BN products analyzed in the range of 2θ = 15°-80° (step size of 0.02°). HR-TEM images were obtained using a Zeiss Libra 200 MC TEM/STEM operating at an accelerating voltage of 200 kV. SEM images were obtained using a Zeiss Auriga FIB-SEM operating at an electron accelerating voltage of 30 keV and ion accelerating voltage of 5 kV. For HR-TEM and FIB-SEM analysis, samples were prepared by casting a drop from IPA dispersions onto silicon wafers and subsequently allowing solvent to evaporate.

Dielectric Spectroscopy was performed on a Novocontrol Alpha-A impedance analyzer. Powder samples were pressed similarly until compaction, and the dielectric properties (accuracy of ±5-10%) measured at room temperature with an applied external voltage of 1V. Nitrogen adsorption analysis was performed on a Micromeritics Tristar 3000 at 77 K. Prior to measurement the samples were degassed at 200 ℃ under flowing nitrogen overnight. For BET analysis, the specific surface area was calculated using the Brunauer-Emmett-Teller (BET) equation utilizing the adsorption branch (±0.01 m^2/g). The pore size distribution plot was derived from the adsorption branch of the isotherms using the Barrett-Joyner-Halenda (BJH) method. Optical measurements were performed in the wavelength interval of 250-800 nm (±2 nm) with a Thermo Scientific Evolution 600 UV-Vis Spectrometer using Spectrosil Far UV Quartz 10 mm cuvettes (Starna Cells Inc.).

Appendix B

Macroscopic Properties of Restacked, Redox-Liquid Exfoliated Graphite and Graphite Mimics Produced in Bulk Quantities

1.TGA

Table B1: Sample information and corresponding values obtained from TGA analysis

Sample	Antioxidant[a)]	Δ wt.%[b)]	T_{max} [T_{min1}, T_{min2}…][c)] (°C)	Residue[d)] (wt. %)
Graphite (precursor)	--	--	691	1.1
G1		-0.7	670	9.1
G2	BHT	-1.8	700	3.4
G3	TEMPO	-1.6	704	5.9
MoS_2 (precursor)	--	-10.6	789 [475, 382]	3.0
MS 1		-9.5	752 [497, 390]	15.2
MS 2	SBS	-7.0	729 [496, 395]	54.0
MS 3	TEMPO	-9.6	718 [487, 392]	17.8
BN (precursor)	--	N/A	N/A	104.2
BN1				94.0
BN2	BHT			101.5
BN3	TEMPO			111.3

[a)] For all reactions, the concentrations of SBS and TEMPO in isopropanol were each 1.0 mg/ml, and the concentration of BHT in isopropanol was 0.1 mg/ml. [b)] Change in weight loss (Δ wt.%, ± 2.0wt.%) is reported in the temperature range of 200-400°C. [c)] Temperature of maximum degradation (T_{max}) obtained from the TGA plots. MoS_2 displayed two minor degradation steps denoted as T_{min1} and T_{min2}. For the BN samples, no T_{max} was observed. [d)] Residual wt.% after the heating process.

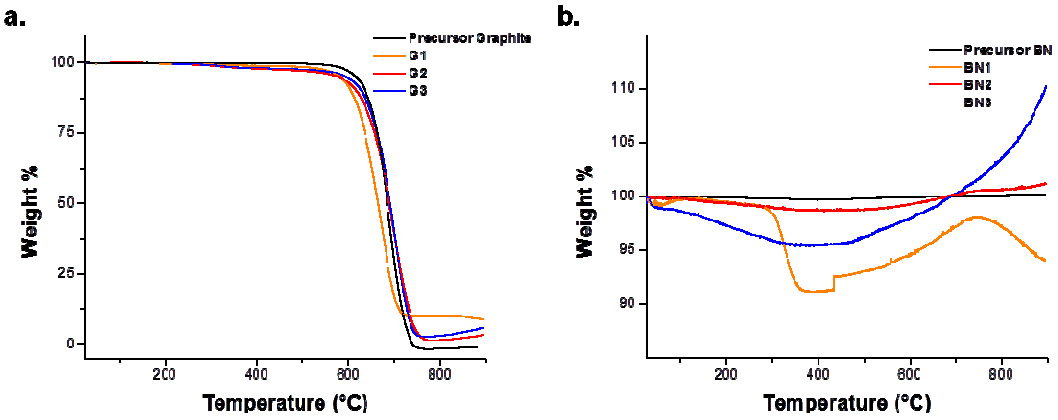

Figure 29. TGA plots (air) of a) precursor and exfoliated graphite products and b) precursor and exfoliated h-BN products

Sample information and corresponding results obtained from TGA analysis are provided in **Table B1**. TGA plots of precursor graphite and exfoliated graphite products (**Figure 29a**) and of precursor boron nitride (h-BN) and exfoliated h-BN products (**Figure 29b**) were obtained. The T_{max} values for G2 and G3 are significantly higher than those reported for natural graphites of average particle sizes ranging from 2-40 µm[153] and similar to the value found for ~1-2 µm synthetic graphite powder (Sigma).[223] Contrastingly, h-BN displays significant resistance to thermal oxidation. BN resistance to oxidation has been determined experimentally[224], and exposure of h-BN to atomic oxygen at extremely high temperature and pressure has shown to generate B_2O_3 forming B-O bonds thus decreasing the presence of B-N bonds.[54]

2. TGA-MS

Table B2: Tabulated results from TGA-MS analysis including weight loss and ion current for m/z = 44

Sample	Δ wt.%[a)]	$IC_{900\,°C}$[b)]	$IC_{Normalized}$[c)]
Graphite[d)]	2.3	4.73×10^{-7}	N/A
G1	8.1	2.92×10^{-7}	0.61
G2	5.3	3.59×10^{-7}	0.76
G3	6.3	2.13×10^{-7}	0.45
MoS_2[d]	4.4	1.38×10^{-7}	N/A
MS1	5.3	1.32×10^{-7}	0.96
MS2	26.2	6.89×10^{-7}	4.99
MS3	21.9	2.58×10^{-7}	1.87
BN[d]	0.0	$< 10^{-15}$	N/A
BN1	1.7	1.60×10^{-7}	
BN2	1.9	2.17×10^{-7}	
BN3	1.4	6.63×10^{-8}	

[a)] Change in weight measured as the difference between initial and residual weights (error = ± 0.1wt.%). [b)] Ion current measured for m/z= 44. [c)] Ratio of the measured ion current for m/z=44 of the exfoliated samples to the precursor powders. [d)] Denotes precursor powder.

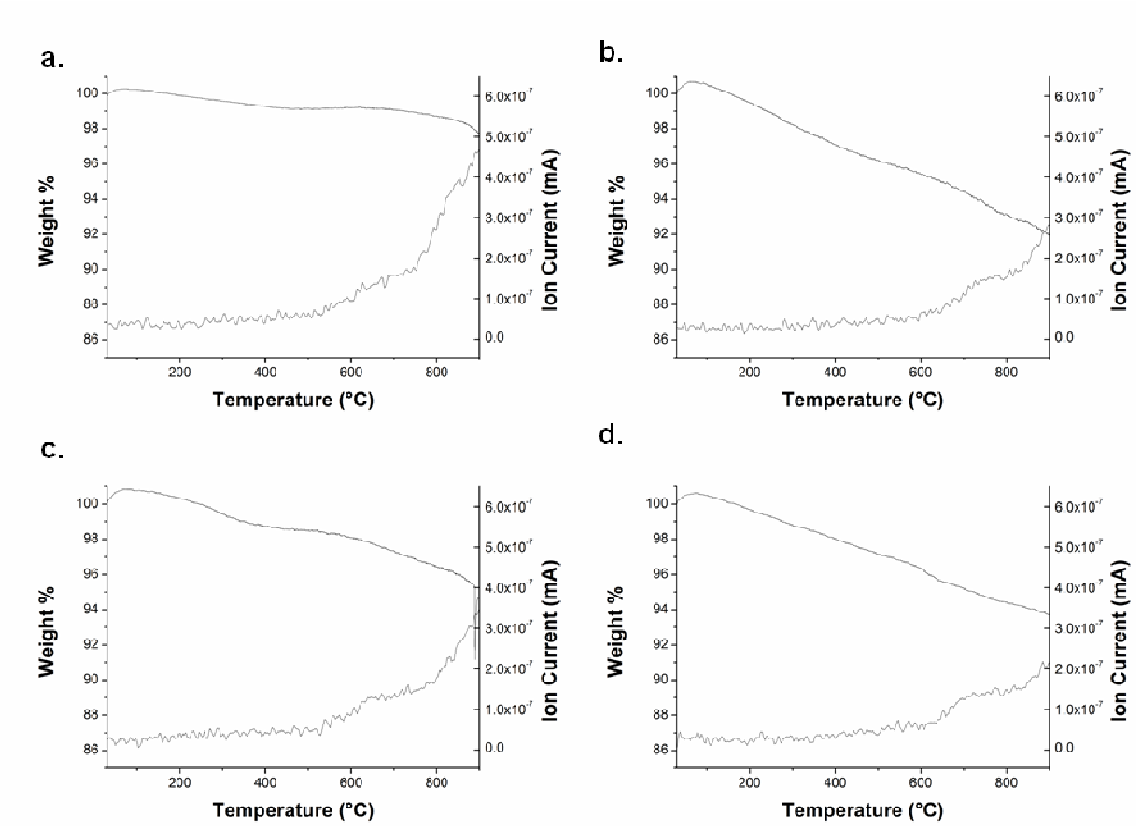

Figure 30. TGA-MS plots showing respective ion currents (m/z=44) of a) precursor graphite, b) G1, b) G2, and c) G3

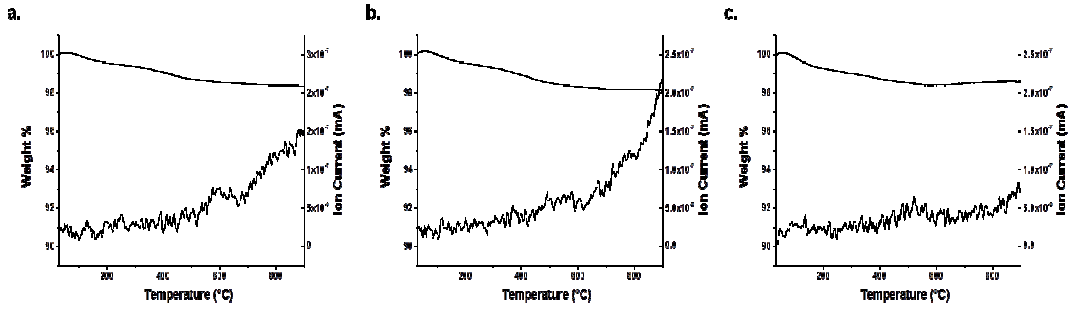

Figure 31. TGA-MS plots showing respective ion currents (m/z=44) for a) BN1, b) BN2, and c) BN3

Data from TGA-MS measurements are shown in **Table B2** and corresponding weight losses were calculated to observe any changes from residue or functionality introduced by sonication. The TGA-MS plots measured for precursor and exfoliated graphites and h-BN samples are shown in **Figure 30** and **Figure 31** respectively. Precursor BN did not display any weight loss or any major evolution of CO_2 gas.

3. XPS

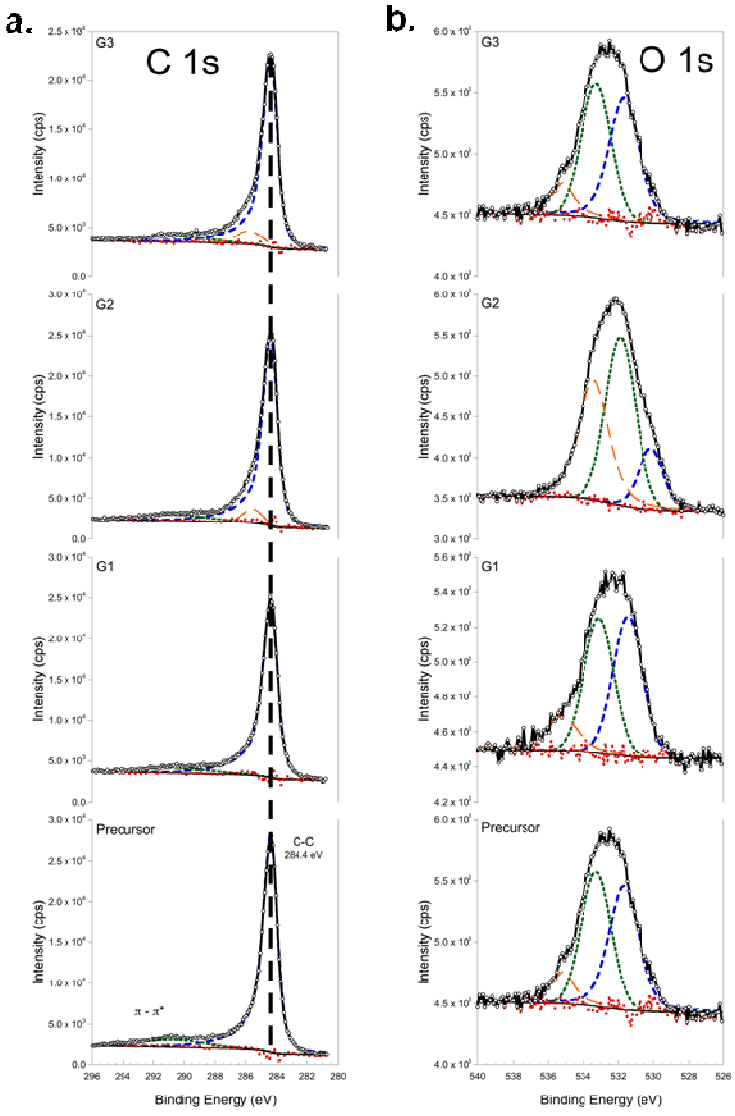

Figure 32. XPS plots of precursor and exfoliated graphite samples corresponding to a) C1s and b) O1s peaks

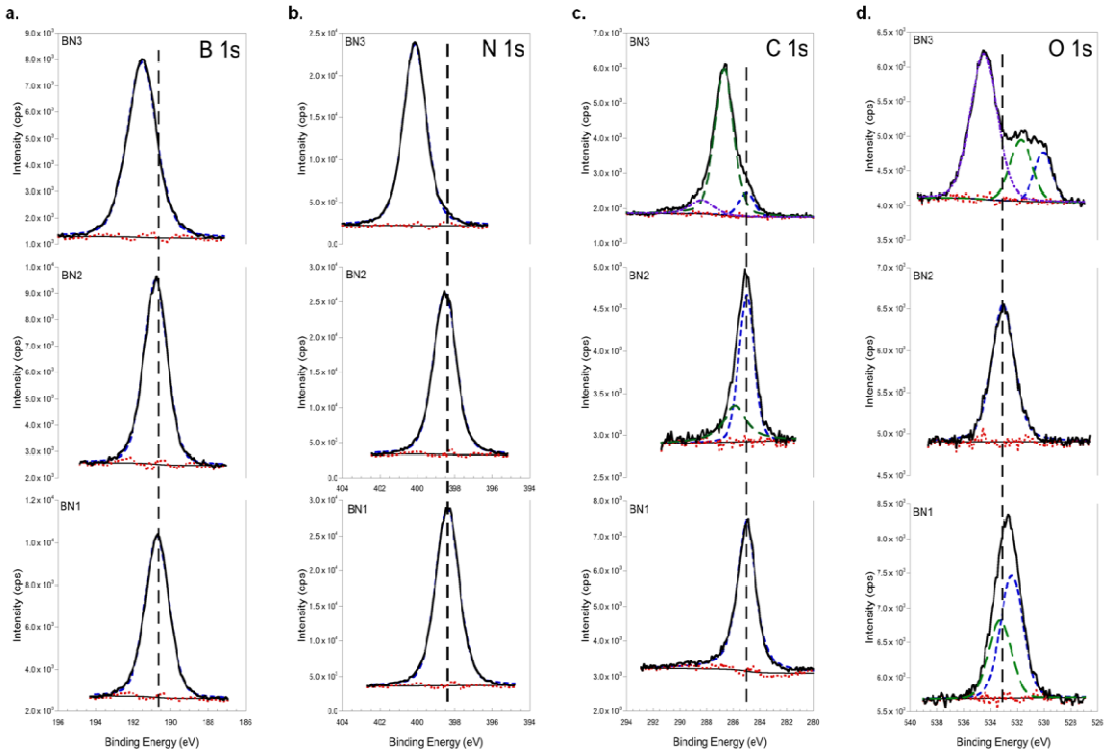

Figure 33. XPS plots of exfoliated BN samples corresponding to a) B1s, b) N1s, c) C1s, and d) O1s peaks

Table B3: Summary of elemental concentrations (in atomic percent)[a], which were derived from multiplex spectra

Sample	At.% C	At.% O	At.% B	At.% N	At.% Mo	At.% S
G1	96.1	3.9	N/A			
G2	92.0	8.0				
G3	94.3	5.7				
MS1	44.2	10.2	N/A		17.6	27.9
MS2	50.9	9.9			15.0	24.2
MS3	49.6	9.7			16.5	24.2
BN1	13.5	4.4	41.8	40.4	N/A	
BN2	12.7	3.5	43.2	40.7		
BN3	17.3	6.0	39.1	37.7		

[a] Atomic percentages of sample surface obtained from multiplex measurements.

For deconvolution of the C 1s peak, samples were fit using parameters established with freshly cleaved HOGP (SPI – Grade 2). Values are reported after calibration of the C-C (sp^2) peak to 284.4 eV. If a satisfactory fit could not be obtained using the C=C/C-C (aromatic/graphite) peak at 284.4 eV and the $\pi \rightarrow \pi^*$ shake-up at 290.6 eV then another sub-peak was introduced. A similar fitting procedure has been established previously.[225]

4. ATR-FTIR

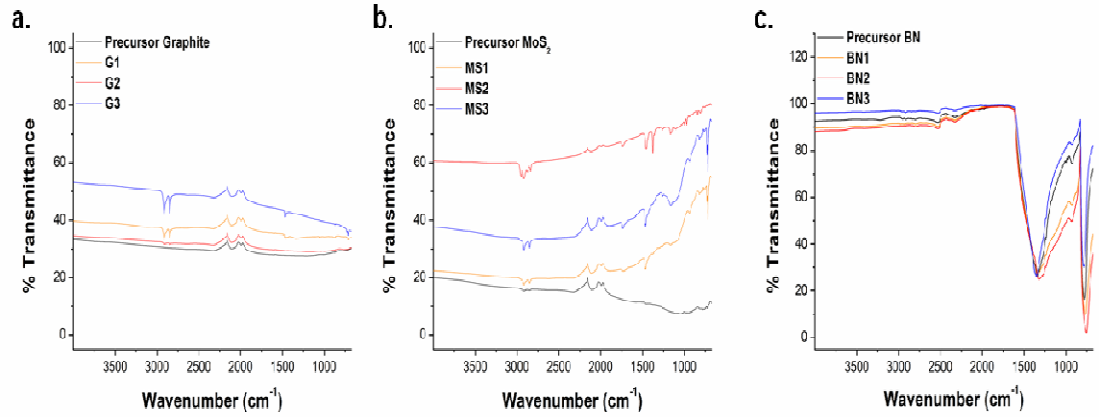

Figure 34. ATR-FTIR spectra of precursor and restacked a) graphites, b) MoS_2 samples, and c) BN samples

5. Raman Spectroscopy

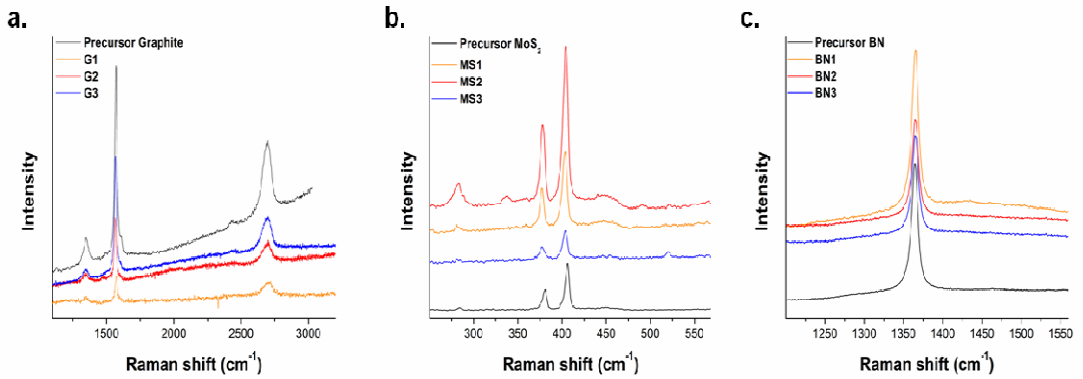

Figure 35. Raman spectra of precursor and restacked a) graphite, b) MoS_2 and c) h-BN samples

6. Powder XRD

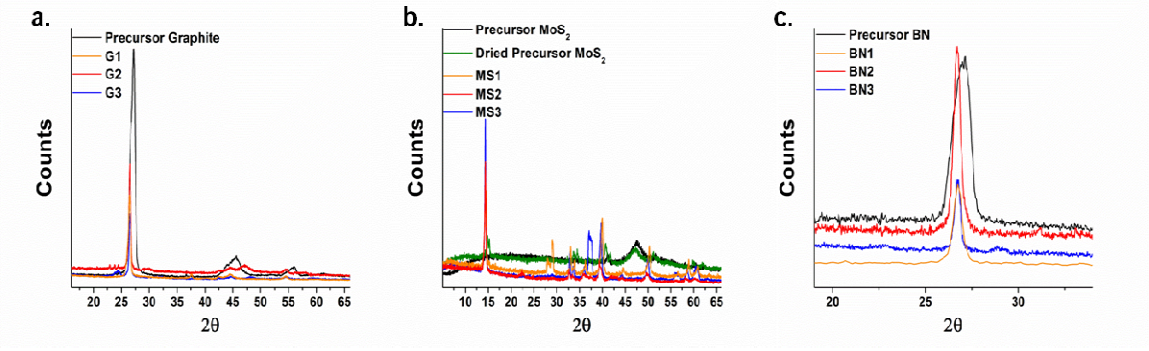

Figure 36. XRD patterns of a) graphite, b) MoS2 and c) h-BN samples

7. HR-TEM

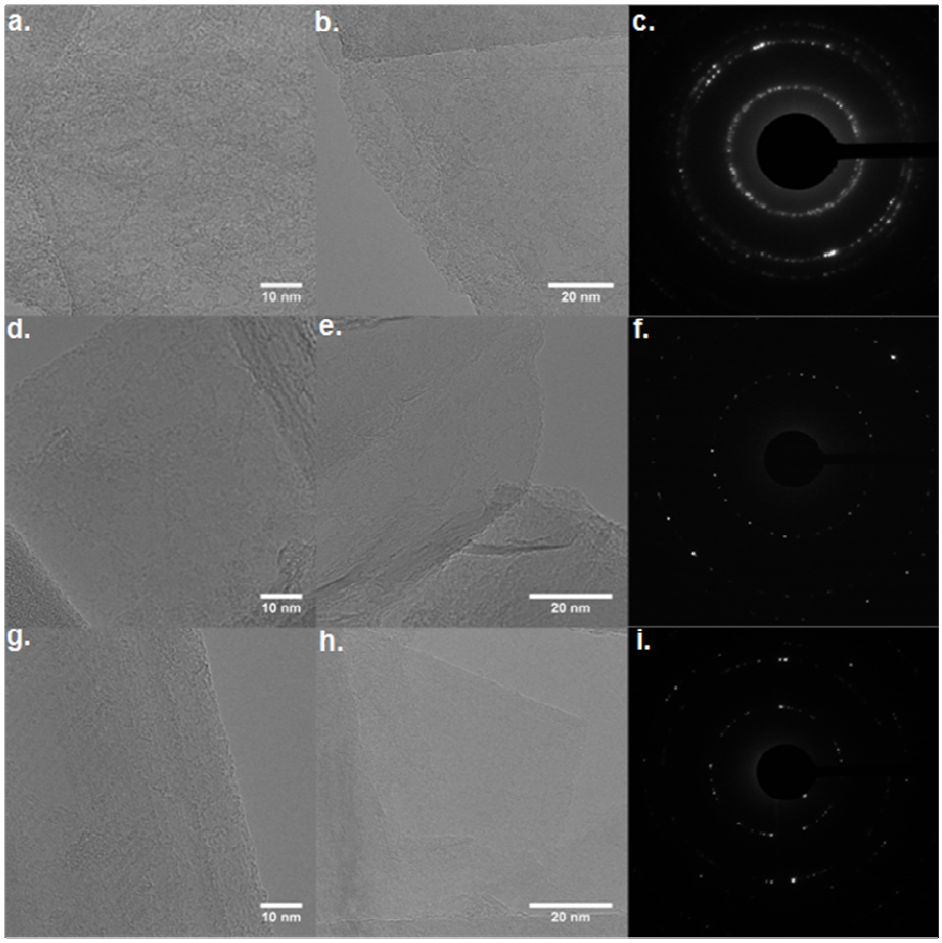

Figure 37. HR-TEM micrographs of a-b) G1 (c: SAED pattern), d-e) G2 (f: SAED pattern), and g-h) G3 (i: SAED pattern)

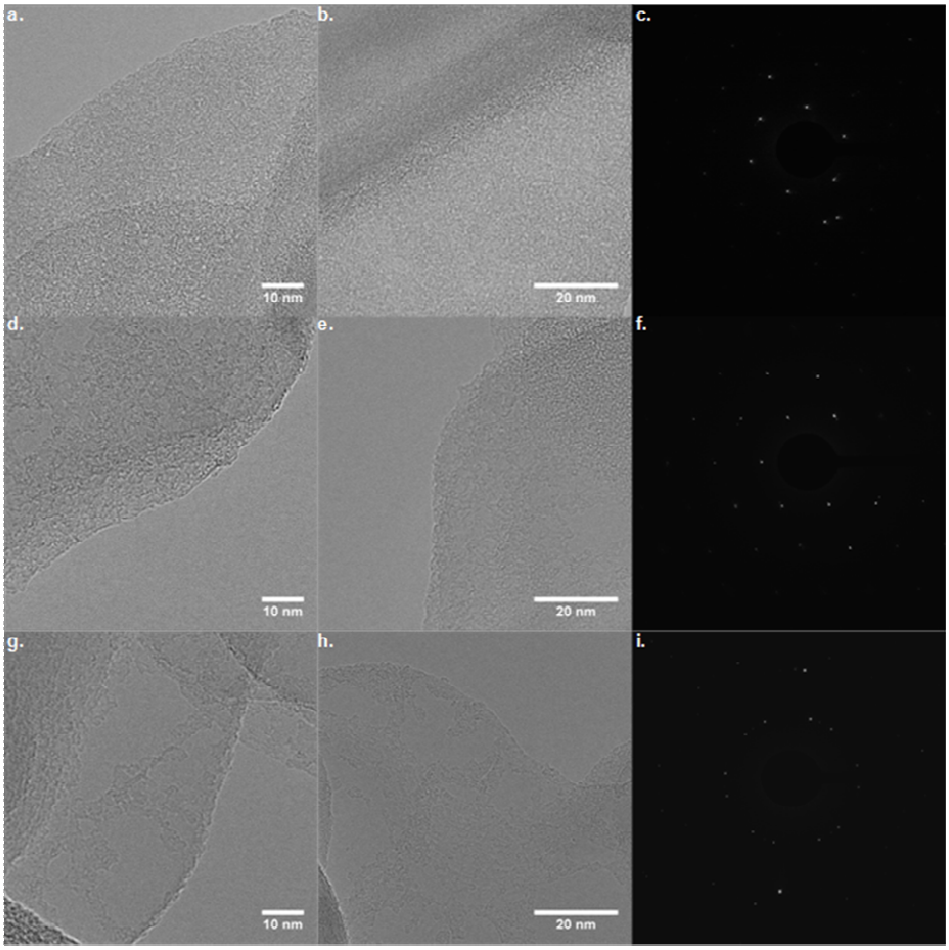

Figure 38. HR-TEM micrographs of a-b) BN1 (c: SAED pattern), d-e) BN2 (f: SAED pattern), and g-h) BN3 (i: SAED pattern)

8. SEM

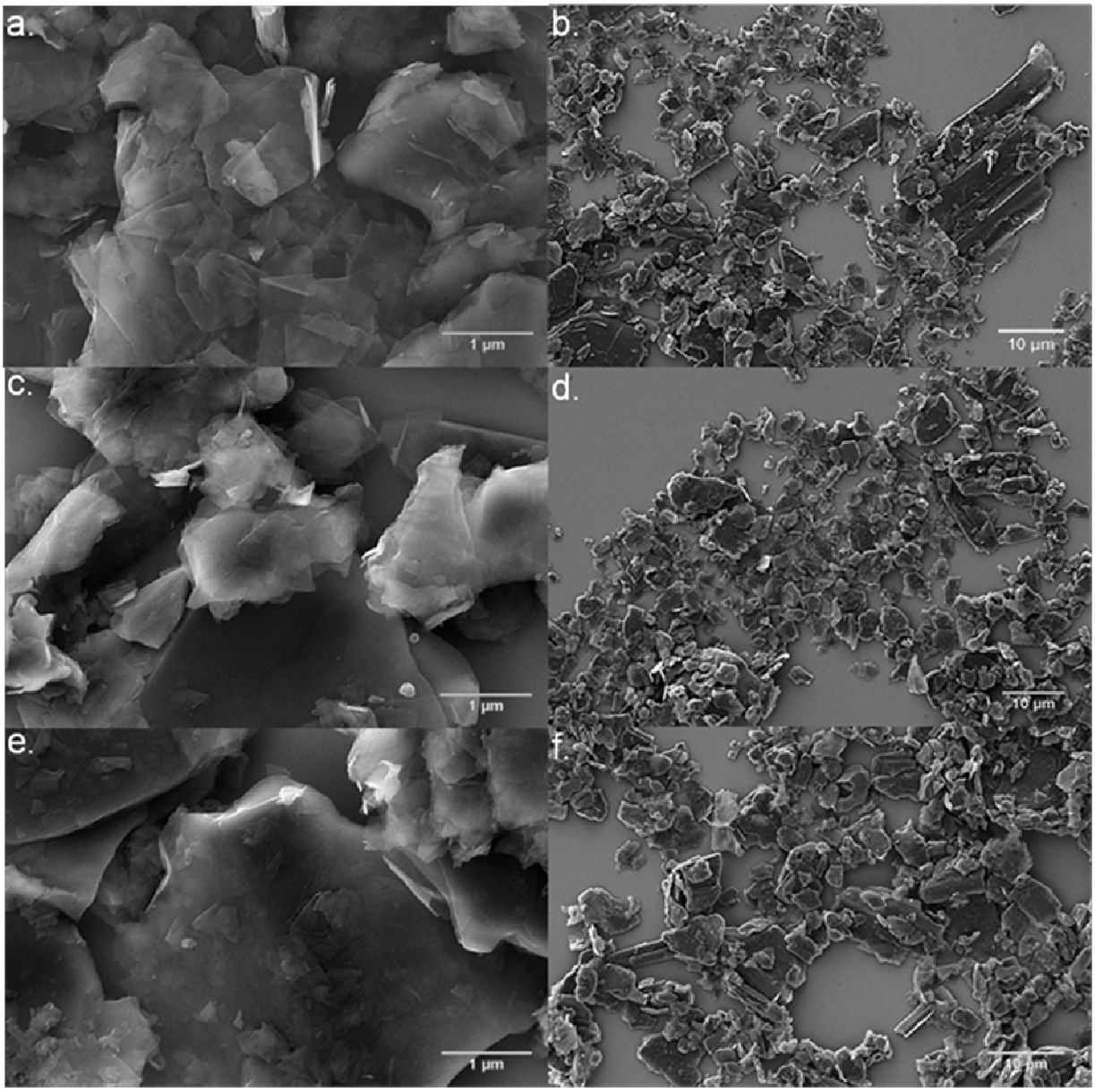

Figure 39. SEM images of samples a-b) G1, c-d) G2, and e-f) G3

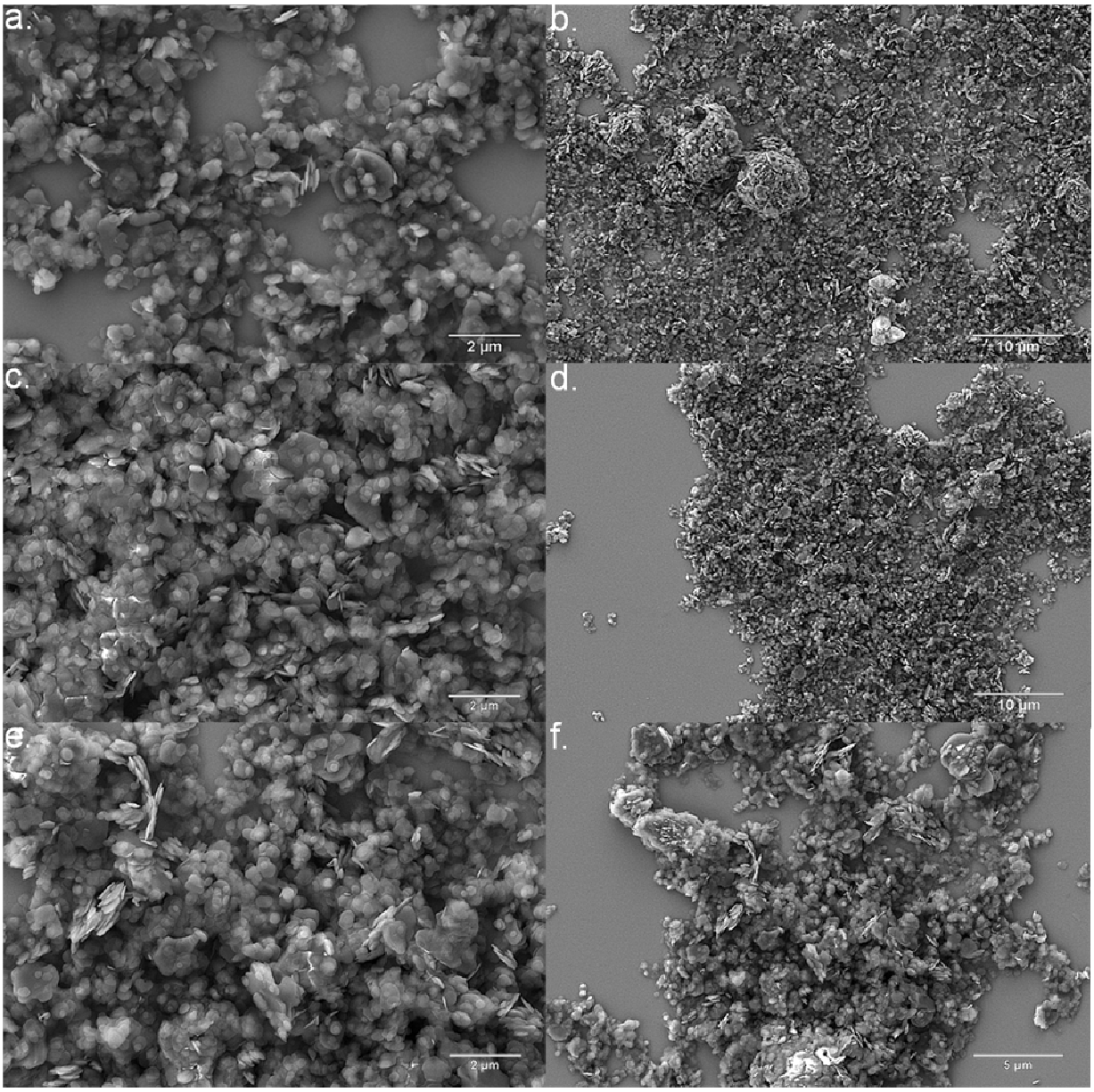

Figure 40. SEM images of samples a-b) BN1, c-d) BN2, and e-f) BN3

9. Optical (UV-Vis) Absorbance

Table B4: Calculated and reported molar absorptivity coefficients of sonication-assisted exfoliated 2-D layered powders

Sample	α_{λ} [a)]	α_{lit} [b)]
G1	434	2460[77], 3620[78]
MS1	1123	3400[85], 1517[87]
BN1	1970	2467[85]

[a)] Values are reported in units of mL/(mg*m), and calculated at the corresponding wavelengths. [b)] Values were reported in units of mL/(mg*m).

Table B5: Hansen solubility parameters of materials and solvents used in this work

Material[a)]	δ_D ($MPa^{1/2}$)	δ_P ($MPa^{1/2}$)	δ_H ($MPa^{1/2}$)
Graphite[b)]	15-21	3-17	2-18
MoS_2[c)]	17-19	6-12	4.5-8.5
BN[c)]	17-19	4-10	4-10
Solvent			
IPA[b)]	15.8	6.1	16.4
$CHCl_3$[b)]	17.8	3.1	5.7

[a)] The Hansen parameters are reported as ranges. [b)] Values were obtained from Ref. 41. [c)] Values were obtained from Ref. 42.

The solubility characteristics of two dimensional solutes were theoretically studied[185] and found to be consistent with both Hildebrand and Hansen solubility parameters, when accounting for solute dimensionality. The Hansen solubility parameters of the layered powders and the chosen solvents are listed in **Table B5**.

10. Dielectric Spectroscopy

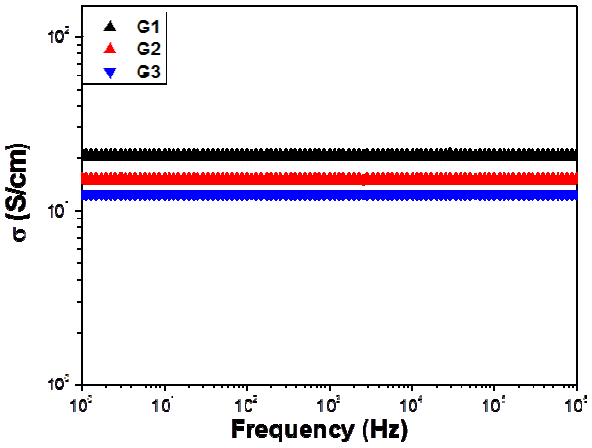

Figure B13: D.C. conductivities of exfoliated graphite samples

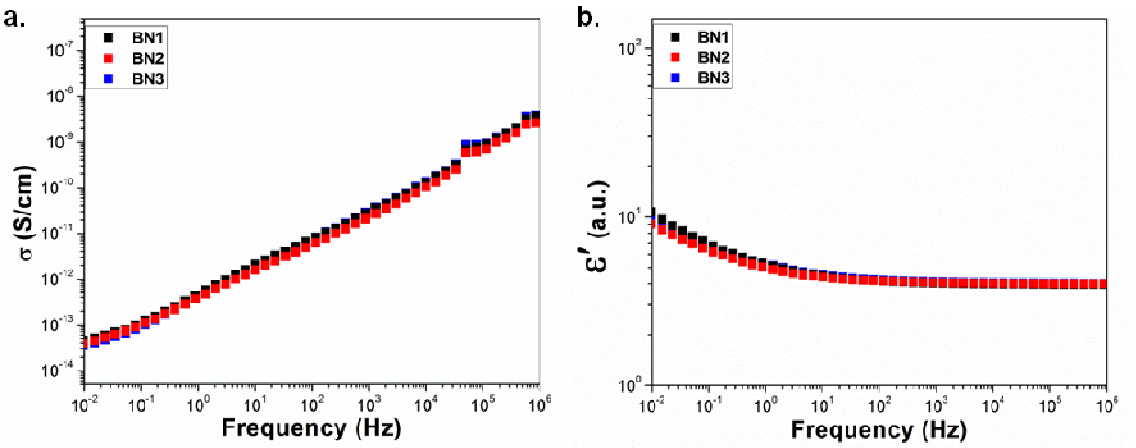

Figure B14: Dielectric spectroscopy results for a) D.C. conductivity and b) relative permittivity of BN1 (black), BN2 (red), and BN3 (blue)

11. BET (N_2 Adsorption)

Table B6: BET Analysis from N_2 adsorption

Sample[a)]	Surface Area (m^2/g)	Pore Volume (cm^3/g)	Average Pore Size (nm)
Graphite (precursor)	17.98	0.0506	11.49
G1	9.89	0.0374	15.24
G2	11.81	0.0437	12.84
MoS_2 (precursor)	10.36	0.0475	18.10
MS1	13.30	0.0501	14.53
MS2	11.29	0.0459	15.22
BN (precursor)	23.85	0.1180	18.67
BN1	24.43	0.1152	18.25
BN2	25.22	0.1411	17.95

[a)] Samples were synthesized in larger quantities, as described in the experimental section.

Results obtained from BET analysis were obtained with an error of ≈ ±0.01 m^2/g.

CHAPTER III
TAILORED PHOTOLUMINESCENCE AND STABILITY IN AQUEOUS DISPERSIONS OF FRAGMENTED MOS_2 PARTICLES

Abstract

Chemically fragmented molybdenum disulfide (MoS_2) particles were produced in large quantities using a facile liquid and redox-liquid exfoliation process. Aqueous suspensions from restacked, liquid and redox-liquid exfoliated particles were prepared, and the sedimentation of agglomerates observed to determine dispersed particle properties. During the sedimentation process, both of the aqueous dispersions of exfoliated MoS_2 particles displayed unique particle sizes, steric stability, and photoluminescence. The fragmented MoS_2 particles produced using redox-liquid exfoliation displayed sensitivity to pH due to favorable hydrogen bonding interactions. Both the liquid and redox-liquid fragmented particles were added separately at similar concentrations to aqueous poly(ethylene) glycol (PEG) solutions to form highly stable suspensions with increased photoluminescence, even during sedimentation.

Introduction

Since the discovery and isolation of monolayer graphene using a simple exfoliation method,[11, 12] research regarding two-dimensional layered materials has become a large focal point of materials science, chemistry, and physics. The production of graphene through chemical means has been detailed,[226] highlighting significance of chemically exfoliated graphenes in colloidal applications. The explosion of research interest in graphene has expanded to include inorganic graphene analogues,[13, 14, 16, 17, 35] which display different material properties. The exfoliation of layered transition metal dichalcogenides (TMDs), specifically MoS_2 and WS_2, are of particular interest given their unique

characteristics.[35, 57, 96] The applications of these materials are numerous as they display desirable characteristics for optoelectronics[37], lubricants[38], photocatalysis[97],and mechanical reinforcement.[39]

Bulk MoS_2 has an indirect band gap of ~1.2 eV while its monolayer form has a direct band gap of ~1.9 eV.[34, 36, 37] The change of the bandgap was understood by the semiconducting and catalytic behavior of nanoscale MoS_2 due to quantum confinement of 3-D crystallites,[195, 227] and the intrinsic 2-D confinement effects of monolayer MoS_2 respectively.[203, 207, 228, 229] These developments highlighted the significance of exfoliated 2-D MoS_2 and the capability to tailor photoluminescence of the exfoliated monolayer and few-layered MoS_2 sheets. A novel exfoliation method to obtain graphene was reported by simply sonicating graphite dispersions in solvent.[77] The ability to exfoliate graphite using the liquid exfoliation method was explored extensively[78, 80, 81, 135] and shown to be a viable method to chemically modify graphene.[89] This method was further used to obtain monolayer 2H-MoS_2,[85] and the interactions between solvent and 2H-MoS_2 determined based on solubility parameters.[86]

As the associated chemistry of MoS_2 has increased the viability of 2-D sheets for device applications, the capability to generate favorable structures and fabrication methods is still required.[56] As isolated graphene obtained from liquid-exfoliated graphite displayed no significant edge oxidation,[77] inclusion of antioxidant during the liquid-exfoliation of few-layered graphene allowed for the isolation of MWNTs.[154] However centrifugation and pretreatment of the sheets

was necessary prior to generating the MWNTs. Similarly, to increase yield and simplify the process, we previously fragmented MoS_2 powder in bulk using redox-liquid exfoliation (Srivastava, V.K., et al. *Advanced Functional Materials*, **2014 (Accepted)**). This method generated large quantities of fragmented MoS_2 with intercalated species which affected the macroscopic properties. In this work, aqueous and organic dispersions from restacked sheets of liquid and redox-liquid exfoliated MoS_2 were prepared to observe the colloidal properties and interactions. As sedimentation has been shown to occur due to re-aggregation of particles,[230] observations of this process on the changes in photo-optical and structural properties of aqueous dispersions was performed. Also since exfoliated MoS_2 has been used for inkjet deposition,[61, 231] we investigated the changes on solution properties upon the addition of poly(ethylene) glycol to the dispersions.

Experimental Section

Materials

Precursor MoS_2 (Sigma-Aldrich, < 2µm) powder and sodium bisulfite (Acros Organics, Analytical Grade) were used as received. Water (Submicron Filtered, HPLC Grade), 2-propanol (Certified ACS), hexane (HPLC grade) and dimethyl sulfoxide (Certified ACS Reagent Grade) were purchased from Fisher Scientific and used as received. Polyethylene glycol (PEG, average $M_n = 4000$) was purchased from Sigma-Aldrich and used as received. Nitric acid (Stock #35624, 1.0N Standard Solution) and ammonium hydroxide (Stock #35614, 1.0N Standard Solution) were purchased from Alfa Aesar and used as received. For

acidic and basic aqueous solutions, pH was measured using a VWR Symphony Ag/AgCl pH meter. The pH meter was calibrated from 3 points using Micro Essentials Standards. Dispersions were measured using Spectrosil Far UV Quartz 10 mm cuvettes (Starna Cells Inc.).

Preparation of Solvent and PEG Dispersions

Aqueous and organic dispersions of restacked MS1 and MS2 were made at concentrations of 0.1 mg/ml. These dispersions were generated using brief sonication (15 seconds) until agglomerated particles were no longer visible. The aqueous and organic dispersions were subsequently analyzed. PEG was added (concentration of 20 wt.% PEG/H_2O) to water (reference) and aqueous dispersions of MS1 and MS2 (0.1 mg/ml) and stirred until completely dissolved to form polymer/particle dispersions. The PEG reference solution and sample dispersions were sonicated (15 seconds) prior to measurements.

Characterization Methods of MoS_2 Dispersions

Optical absorbance (UV-Vis) was measured in the wavelength interval of 250-800 nm using a Thermo Scientific Evolution 600 UV-Vis Spectrometer. Dynamic laser-light scattering (DLLS) of aqueous dispersions to obtain particle size and zeta potential was determined using a NanoBrook ZetaPALS. Field emission scanning electron microscopy (FESEM) was performed using a Zeiss Auriga SEM at an operating voltage of 20 kV. Samples were prepared by casting a droplet onto a silicon wafer from aqueous dispersions after 6 hours of sedimentation without disturbing sedimented particles. Optical/laser-scanning

confocal (LSC) microscopy was performed using a Leica SP2 Microscope. The samples were prepared by casting a drop of the aqueous dispersions onto glass slides without disturbing the sedimented material. Images were obtained in transmission mode, and at excitation wavelengths of 543 (HeNe, ~0.5 mW) and 633 (HeNe, ~1 mW) nm using a HCX PL APO 63x1.20 objective. The photoluminescence (PL) spectra of aqueous solutions were measured using a PerkinElmer LS 55 Luminescence Spectrometer at an excitation wavelength of 532 nm. Sample photoluminescence was measured in the absorbance wavelength range of 540-900 nm at 1 hour intervals using a pulsed Xe lamp and automatic lamp shut off to minimize quenching.

Results and Discussion

Bulk Redox-Liquid Exfoliation of MoS_2 Powder

Liquid-exfoliation of MoS_2 has been performed on a large-scale using solvent,[88] mixed-solvent,[15] and aqueous/surfactant[61, 87] exfoliation conditions were used to produce high-concentrations of dispersed, exfoliated MoS_2 sheets. Despite the simplicity of these methods to obtain high-yields of exfoliated MoS_2 sheets, the non-volatile solvents and surfactants used can physisorb to the sheets and prove difficult to remove. Furthermore, the residual solvent or surfactant can greatly affect the properties of the exfoliated MoS_2 sheets, thus requiring centrifugation or other methods for isolation of desired sheets. Previously, using antioxidant, a redox-liquid exfoliation method of MoS_2 powder suggested the formation of an intercalated compound **(Figure 41)**.

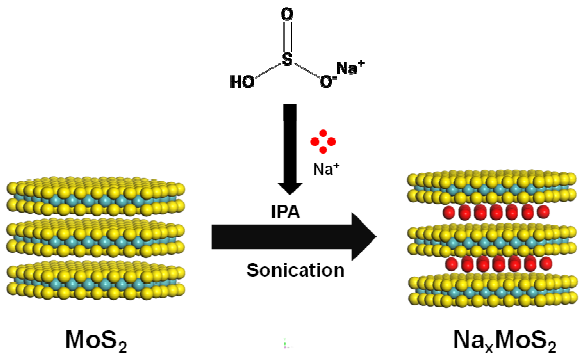

Figure 41. Illustration of the redox-liquid exfoliation process to produce sodium intercalated/exfoliated MoS_2 compounds

The influence of intercalated species on bulk characteristics would alter the dispersion characteristics of the fragmented MoS_2 layers. One major influence on dispersion stability is the sedimentation process due to re-aggregation attributed to insoluble phases and sample impurities of inorganic $Mo_6S_{4.5}I_{4.5}$ nanotubes.[230] A model for sedimentation was explained by an exponential decay, which was also applied to exfoliated graphite.[82] However this model was determined to apply for sedimentation over an extended period of time, greater than 100 hours. Therefore, we investigated the stability of the dispersions over a short time frame (6 hours) to observe the sedimentation process on dispersion stability, particle size, sensitivity to pH changes, and photoluminescence of the dispersions.

Optical Absorbance of Aqueous and Organic Dispersions

As the structure of aqueous dispersions of monolayer MoS_2 were distorted from the bulk 2-D hexagonal to 2-D rectangular unit cell,[232] dispersion behavior of the sheets would also be affected by this change. To observe the effects of the liquid-exfoliation conditions on the dispersions, samples were made at a single

concentration (0.1 mg/ml). Using UV-Vis spectroscopy, aqueous and organic dispersions of the recovered samples MS1 and MS2 powders were measured over a period of time of 6 hours. The solvents were chosen based on their largely differing solvent characteristics. The fixed wavelength of 670 nm corresponds to the first visible peak of fractionated exfoliated MoS_2 nanosheet dispersions,[86] due to the A excitonic peak which changed in intensity during sedimentation.[233] The recorded absorbance of aqueous and organic dispersions at this wavelength, which at same concentrations should minimize any variations due to Mie scattering,[85] are shown in **Figure 42**.

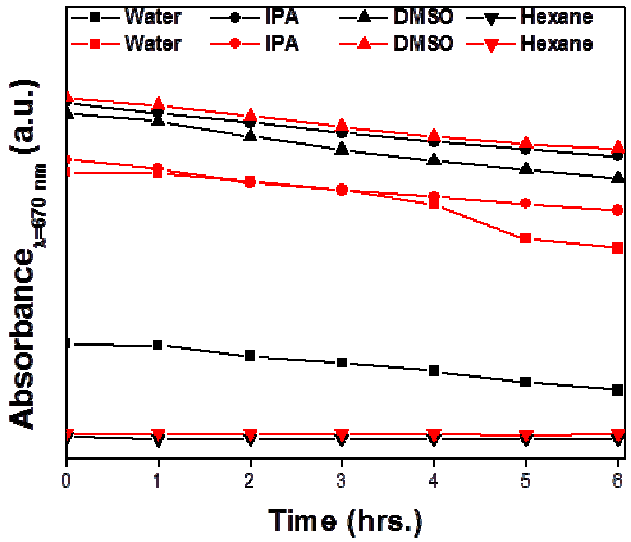

Figure 42. Optical absorbance at λ=670 nm of MS1 (black) and MS2 (red) in various solvents

Sample MS1 displayed poor dispersability in water, similar to the water solubility of $Mo_6S_{4.5}I_{4.5}$ nanowires.[230] Interestingly, dispersions in 2-propanol (IPA) and

dimethyl sulfoxide (DMSO) displayed high, but similar absorbance and stability during sedimentation which was unexpected as DMSO was shown to be a much better dispersing media.[85] However in agreement with our results, IPA was later determined to better disperse MoS_2. [86] Sample MS2 was much more readily dispersed in water, displaying similar absorbance and stability as the IPA dispersion (until ~ 4 hours). Sample MS1 showed better dispersion characteristics in IPA (polar protic solvent) than MS2, however the opposite was true for the DMSO (polar aprotic) dispersions. Not surprisingly both the restacked samples were poorly dispersed in hexane (nonpolar), a poor solvent for dispersing transition metal dichalcogenides.

To further understand the interactions between solvent and particles, the Hansen solubility parameters (HSP) can be used for dispersions. The reported range of HSP values was determined for liquid-exfoliated 2H-MoS_2 sheets.[85] Further investigation of the flake/solvent interaction between MoS_2 and various solvents yielded more definitive values for MoS_2,[86] which are displayed in **Table 2**.

Table 2. Hansen Solubility Parameters

Material/Solvent[a]	δ_D ($MPa^{1/2}$)	δ_P ($MPa^{1/2}$)	δ_H ($MPa^{1/2}$)
MoS_2	17.8	9.0	7.5
Water	15.5	16	42.3
DMSO	18.4	16.4	10.2
2-Propanol	15.8	6.1	16.4
Hexane	14.9	0	0

[a] The HSP for solvents were obtained from *Hansen Solubility Parameters: A User's Handbook (2nd Edition)*.

Based on the HSP values and our results, the increased dispersion in aqueous media for sample MS2 can be understood by comparing the HSP values for water and DMSO. Both MS1 and MS2 displayed excellent and nearly similar dispersability in DMSO and compared to water has nearly identical values for δ_D (dispersion) and δ_P (polarity) parameters. Therefore the difference in dispersion characteristics is attributed to the δ_H parameters for water (42.3 $MPa^{1/2}$) and DMSO (10.2 $MPa^{1/2}$). Considering the δ_H parameter for water is ~4 times greater than the value for DMSO, sample MS2 is greatly influenced by hydrogen bonding interactions. Therefore the influence of pH on particle sizes and steric stability should be greater on the aqueously dispersed MS2 sample, which was investigated during sedimentation.

Particle Sizes and Steric Stability of Aqueous Dispersions

Using dynamic laser light scattering, the particle sizes of the dispersed particles during the re-aggregation process were obtained. Previous work has highlighted the limitations of this method for measuring particle size distributions for dispersions of exfoliated MoS_2 sheets.[234] Therefore we reported the particle size of the dispersed intercalated/exfoliated sheets corresponding to the peak of highest intensity. The average particle size diameter during the sedimentation of the particles up to 6 hours is shown in **Figure 43**.

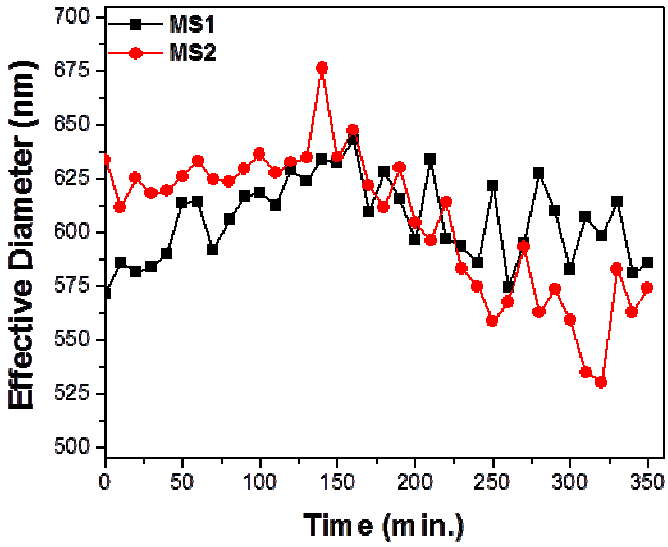

Figure 43. Average particle size of liquid and redox-liquid exfoliated MoS_2 nanosheets

Initially the average particle sizes of both dispersed samples were relatively the same. For both samples, as the particles begin to sediment, the average particle size appeared to increase possibly from formation of

aggregates. Interestingly, after about 5 hours, both samples show a decrease in dispersed particle size, and a larger decrease was observed for sample MS2. Considering the MS2 solution stability determined by optical absorbance, the decrease in average particle size after 5 hours likely results from sedimentation of larger flakes which did not occur for the MS1 solution. To further probe the aqueous stability of both colloids, zeta potential (ζ) and average particle size were both measured at various pH values to determine any influence based on surface charge.

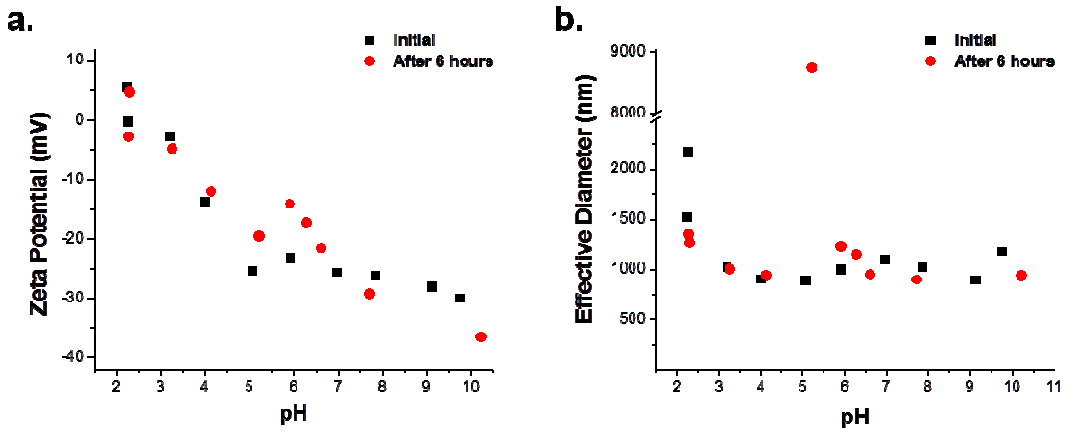

Figure 44. Relation of pH changes of sample MS1 during sedimentation to a) zeta potential and b) particle sizes

As MoS_2 has been studied for use as a hydrogen evolution reaction (HER) catalyst[97], investigation of dispersion stability due to pH change can give insight to the photocatalytic behavior of MoS_2.[235] The aqueous dispersion of sample MS1 was analyzed to determine the observed zeta potential (**Figure 44a)** is shown to decrease with increasing pH, as seen in monolayered MoS_2. [42] At a pH

of ≈ 2.3, the zeta potential was measured to be ~ 4.72 mV, indicating high instability at low pH values contrary to surfactant stabilized exfoliated MoS_2 which displayed zeta potentials ≥ (-)20 mV at low pH [87]. However from pH ≥ 5, the observed zeta potentials began decreasing to < (-)20-40 mV which have been attributed to moderate stability of the exfoliated MoS_2.[61, 87] However for these experiments, surfactants were used to help stabilize the solutions, therefore leading to these low zeta potential values. The point of zero charge (PZC, ζ = 0 mV) was observed to be near pH = ~2.4, likely due to negative surface charge retained on the exfoliated MoS_2 sheets which can occur during restacking and flocculation.[59] In **Figure 44b,** changes in pH appeared to have little effect on the average particle size, although lower pH did appear to increase dispersed particle size, suggesting the formation of larger aggregates during sedimentation.

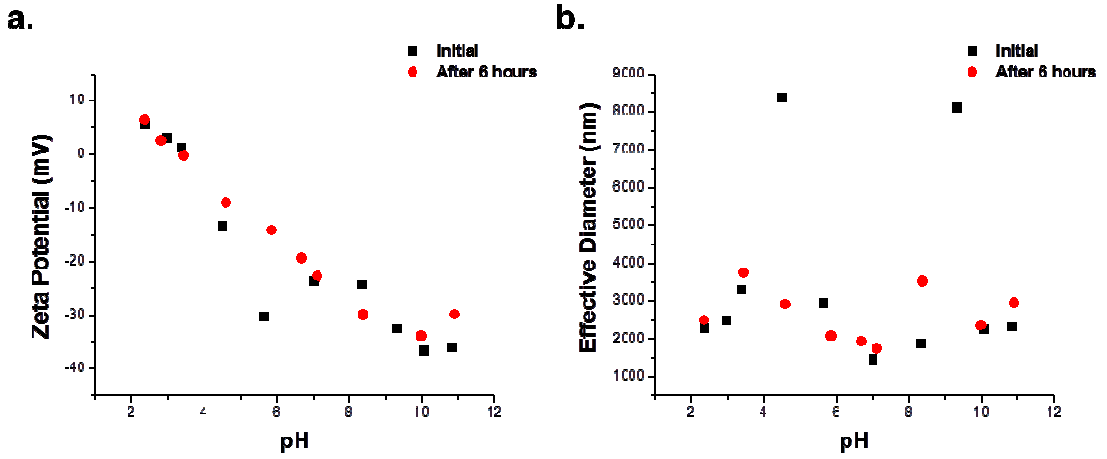

Figure 45. Relation of pH changes of sample MS2 during sedimentation to a) zeta potential and b) particle size

The measured zeta potentials of an aqueous dispersion of sample MS2 (**Figure 45a**) indicated the dispersion was highly unstable at low pH, considering when pH ≈ 2.4 the observed zeta potential was ~6.4 mV even after 6 hours of sedimentation. The PZC for this material, similar to exfoliated WS_2 layers[236], occurs at a slightly higher pH (~3.4) compared to sample MS1, indicating less negative charge which could be from residual "trapped" sodium ions. Also the most stabilized point (lowest zeta potential) for the aqueous dispersion of MS2 was observed at a pH ≈ 10. This result strongly indicated an increased susceptibility to pH compared to sample MS1, suggesting that decreased presence of protonic species forms more highly stable solutions. The increased stability could result from the formation of the 1T phase of MoS_2, which can form highly concentrated dispersions when sonicated in water [203]. Also the change from the 2H to 1T phase of MoS_2 was attributed to any positive charge from the intercalated water bilayer in the sample,[56] and thus considering the increased stability of MS2 in basic conditions, the results suggest the presence of intercalated/physisorbed cationic species. The particle sizes at various pH values (**Figure 45b**) changed significantly, as measured particle sizes of > 2 µm were observed outside of the range of pH = ~5.9-7.2. These values should not be possible given the precursor particle size, but could be a result of aggregated particles or simply even error in measurements as previously reported.[233, 234] Also as the particle sizes were determined based on spherical geometry, error would be expected,[234] and furthermore SEM images demonstrated the presence of

numerous layered, curved sheets (Srivastava, V.K., et al. *Advanced Functional Materials*, **2014 (In Review)**) which did not appear to conform to this shape.

FE-SEM and Optical/LSC Microscopy

Regarding the structural characteristics of the dispersed samples remaining after 6 hours of sedimentation, microscopic techniques were used to observe structures of the still dispersed particles. Using FE-SEM, the lateral dimensionality of the particles was observed and the obtained images **(Figure 46)** showed different structures of dispersed particles in both samples.

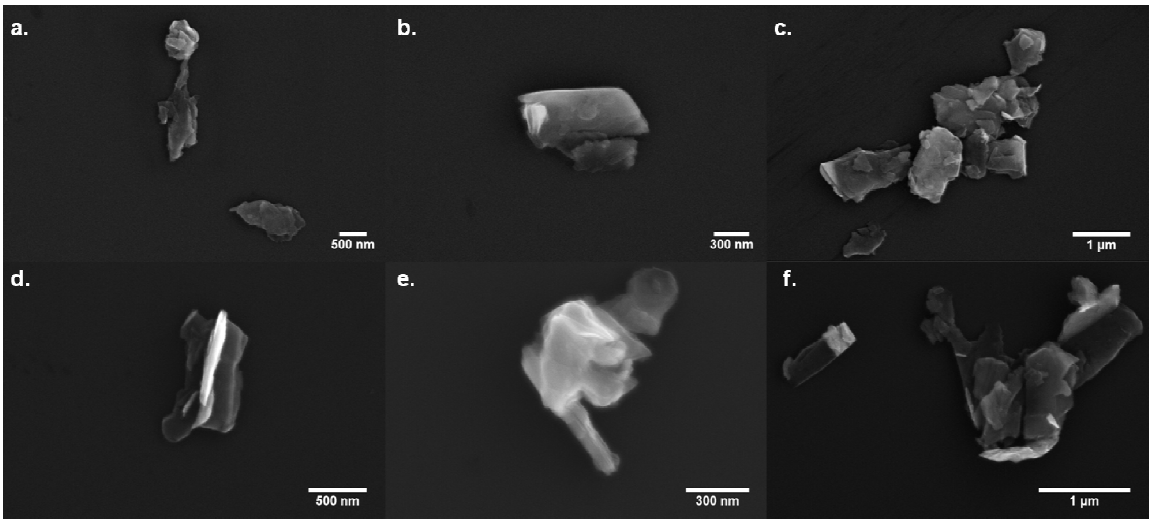

Figure 46. FE-SEM images of dispersed particles (after 6 hours sedimentation) from aqueous dispersions of a-c) MS1 and d-f) MS2

The images of sample MS1 **(Figure 4.5.a-c)** indicate the dispersed particles form aggregates consisting mainly of fragmented 3-D MoS_2 sheets with numerous layers. Lateral lengths appear to be primarily < 1µm, however some nanoscale sheets can be seen. Images of sample MS2 **(Figure 46d-f)** similarly show 3-D

sheets with numerous layers with lateral lengths < 1µm, however in **Figure 46d** sheets appear to scroll to form tubes at the edges. Also a tube-like structure can be seen in **Figure 46e**, consisting of numerous “walls” similar to a MWNT structure.

To further determine particle size and structure, optical/laser excited images from the aqueous dispersions was performed using optical/laser-scanning confocal microscopy. By imaging a droplet of “still-dispersed” particles, these images were obtained using a pseudo-*in situ* technique. Images were taken from optical transmission and confocal laser excitation wavelengths of ~2.28 and ~1.96 eV. From images taken of both samples (**Figure 47**), the remaining dispersed materials appeared quite different between MS1 and MS2.

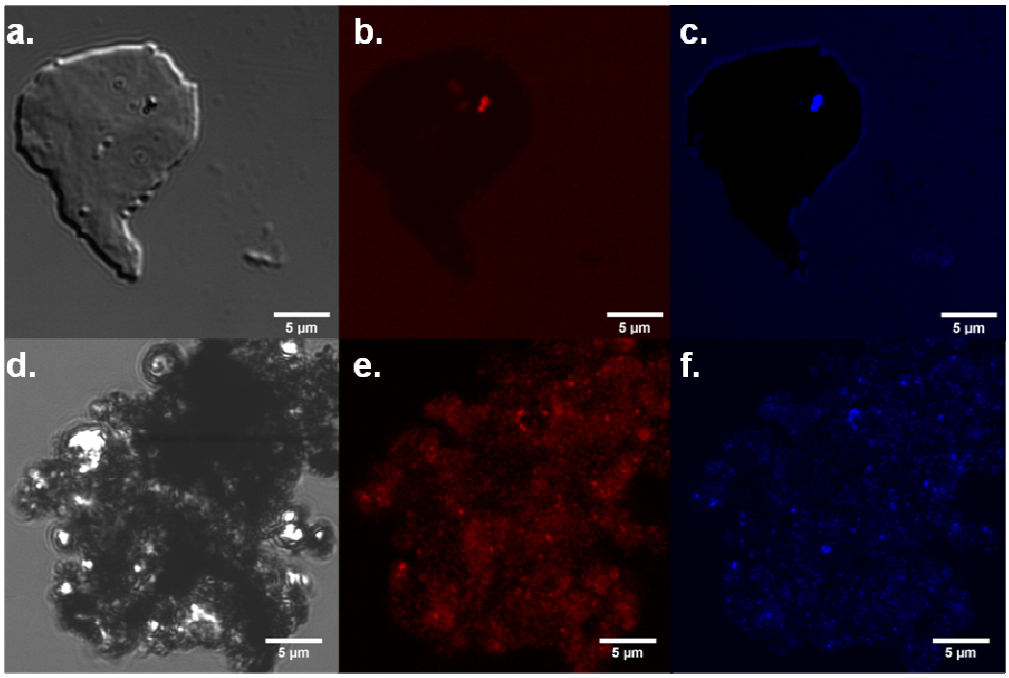

Figure 47. Images of particles from aqueous dispersions, after 6 hours sedimentation, obtained from optical transmittance (black/white) and LSCM excitation at ~2.28 eV (543 nm) (red) and ~1.96 eV (633 nm) (blue) of a-c) MS1 and d-f) MS2

The images of sample MS1 illustrated the presence of agglomerates in aqueous conditions, forming an aggregate larger than the particle size of the precursor powder (< 2 µm). When excited at ~2.28 eV (**Figure 47b)** and ~1.96 eV **(Figure 47c)**, only a single spot displayed photo-emission indicating the aggregated sheets contain numerous layers similar bulk MoS_2. Contrastingly, the aggregated particles of sample MS2 exhibited spherical and tube-like structures **(Figure 47d)**. This aggregate of microstructures displayed excellent photo-emission at ~2.28 eV **(Figure 4.7e)** and ~1.96 eV **(Figure 47f)**, possibly due to greater interlayer separation in the spherical/tube and intercalated structures compared

to the layered structures which would increase the band gap energy.[237] The redox-fragmentation of the bulk MoS_2 generated these structures which could be readily isolated by exploiting the water/particle interaction.

Photoluminescence (PL) of aqueous dispersions

The structures of the dispersed particles observed from microscopy images would affect the PL spectra of the dispersed MoS_2 sheets. For crystalline 2H-MoS_2, a decrease in layers has been shown to increase the band gap to ~1.9 eV for monolayers.[34] The aqueous dispersions were measured during the sedimentation process to determine dispersed particle PL intensities (**Figure 48**). The PL emission peaks were observed in the visible light region of ~1.70-2.05 eV, which correspond to the red shift of the luminescence peaks due to the excitation wavelength of 532 nm.[60, 238]

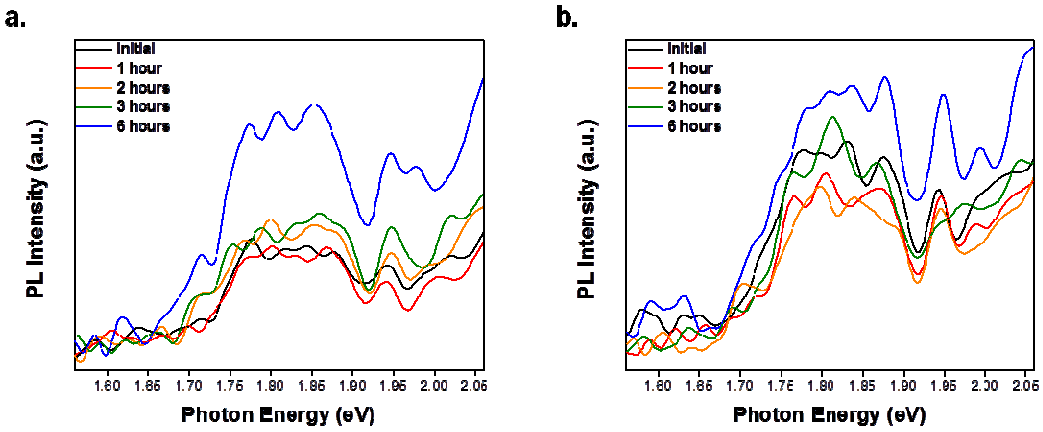

Figure 48. Normalized PL spectra during sedimentation from aqueous dispersions of a) MS1 and b) MS2

During sedimentation, PL of sample MS1 (**Figure 48a**) appeared to decrease but a maximum PL intensity was observed after 6 hours. As 1.5-3 nm (medium-sized) MoS_2 quantum dots are considered to emit visible light in this region,[238] primarily nanoscale sheets appeared to be stabilized after 6 hours. The aqueous dispersion of MS2 (**Figure 48b)** displayed lower PL intensities from ~1.70-2.05 eV with an overall broader peak from ~1.70-1.90 eV compared to MS1, suggesting larger sized sheets are dispersed. However PL peaks observed at ≤ ~1.94 eV for MS2 were not as broad as the corresponding peaks measured for MS1, indicating less nanoscale sheets but lower sample PDI. Also for sample MS2, a significant change in PL intensity for this emission range was observed between 3 to 6 hours of sedimentation. This observation is in agreement with our optical absorbance and particle size measurements of sample MS2, as absorbance and particle size began to decrease significantly after 3 hours.

Photoluminescence and Flow Behavior of MoS_2 Particle Dispersions in PEG/H_2O Solutions

Polymer dispersions of the fragmented MoS_2 products and PEG in water were made due to the excellent stabilization of semiconductor nanocrystals with PEG derivative polymers.[239] The optical absorbance of MS1/PEG and MS2/PEG solutions **(Appendix C, Figure 54)** showed the addition of PEG increased stability of the dispersed particles and decreased the rate of sedimentation even after 6 hours. Adsorption of polymers (chosen due to similar Hildebrand solubility parameters to MoS_2 powder) was successful for dispersing the layered MoS_2 powder in poor exfoliating solvents.[240] The Hildebrand solubility parameters for

PEG varies, as the molecular weight of the polymer can influence the solubility,[241] but the previously determined value of 18.9 $MPa^{1/2}$ for PEG (M_w= 4000)[242] was validated. This value is close to the Hildebrand solubility parameter range of 20-30 $MPa^{1/2}$ found previously for MoS_2 sheets.[85] Given the increased stabilization of the dispersed particles, during sedimentation the PL intensities of both MS1/PEG and MS2/PEG were collected **(Figure 49)** to determine the properties of the PEG dispersed particles.

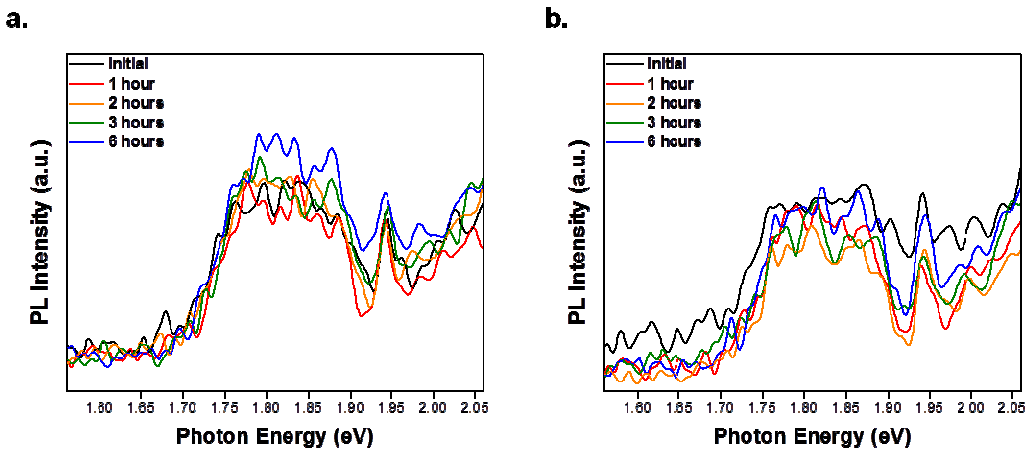

Figure 49. Normalized PL spectra during sedimentation in aqueous dispersions of a) MS1-PEG and b) MS2-PEG

The observed spectra demonstrated minimal effect on PL intensity from PEG, and only vary slightly from the results observed from the aqueous. Interestingly comparing the MS1/PEG and MS2/PEG solutions, sedimentation of particles resulted in higher PL intensity of MS1/PEG which differed from the observed PL of the aqueous particle dispersions. By determining the PL intensities at various photon energies during sedimentation **(Appendix B, Figure 53)**, a clear

difference between the aqueous particle dispersions and the aqueous particle/PEG dispersions emphasized the significance of dispersing media on particle properties.

Conclusions

A facile process to produce chemically fragmented MoS_2 particles in large quantities was performed to explore the colloidal properties in aqueous suspensions. The precursor MoS_2 powder was fragmented using a liquid and redox-liquid exfoliation method to generate two different fragmented products with significantly different behavior in aqueous conditions. The optical absorbance and steric stability of both fragmented samples demonstrated unique differences in solvent/particle interactions, dispersed particle sizes, and sensitivity of dispersion stability to pH. Images of dispersed particles after sedimentation showed structural differences, with redox-liquid exfoliation producing tubular structures and particles exhibiting better photo-emission. The addition of these fragmented particles to PEG/H_2O solutions decreased inherent viscosity, suggesting the ability to tailor particle characteristics for enhanced particle/polymer interaction. Therefore by simple chemical fragmentation of MoS_2 particles, the behavior of the particles can be modified to generate unique properties for applications requiring semiconductors, lubricants, catalysts, and high-strength materials.

Appendix C

Preparation of Bulk Fragmented MoS_2 Particles. The fragmented samples were prepared using a previously reported method (Srivastava, V.K., et al. *Advanced Functional Materials*, **2014 (Accepted)**). Precursor MoS_2 powder (200 mg) was sonicated in a concentrated solution (1.0 mg/ml) of sodium bisulfite/2-propanol. A control sample of MoS_2 powder dispersed in only 2-propanol was made for comparison. Both solutions were stirred briefly in glass amber jars, and then sonicated using a Fisher Scientific FS20H bath sonicator (~70W, 42 KHz) for 2 hours, while maintaining a constant water level at a temperature ≤ 30 ℃. The liquid exfoliated sample (**MS1**), and the redox-liquid exfoliated sample (**MS2**) were washed with excess methanol and filtered using a Hydrophilic PVDF Millicup Filter Unit with a pore size of 0.45 µm (0.47 mm, Millipore). Samples were dried and stored under vacuum and homogenized by physical mixing.

1. Photographs of Dispersions

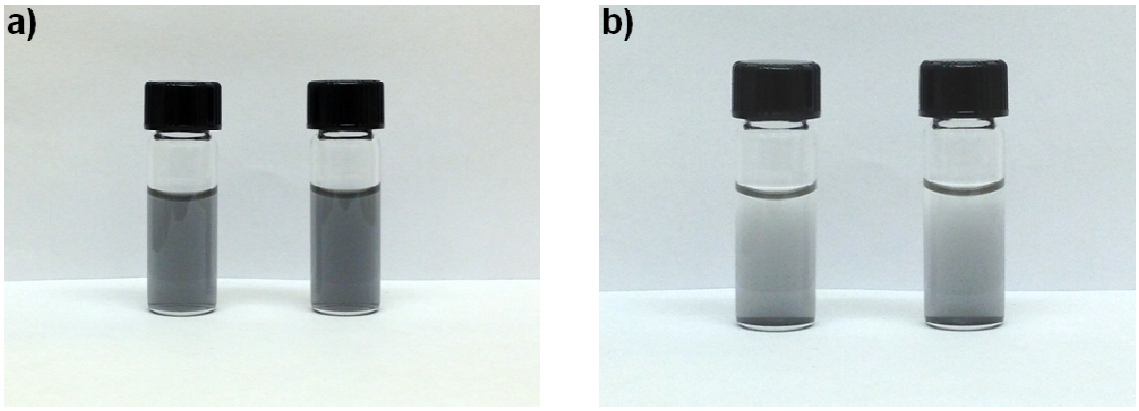

Figure 50. Photographs of aqueous dispersions of MS1 (left) and MS2 (right) during a) initial dispersion and b) after 6 hours sedimentation

2. Optical/Laser Scanning Confocal Microscopy

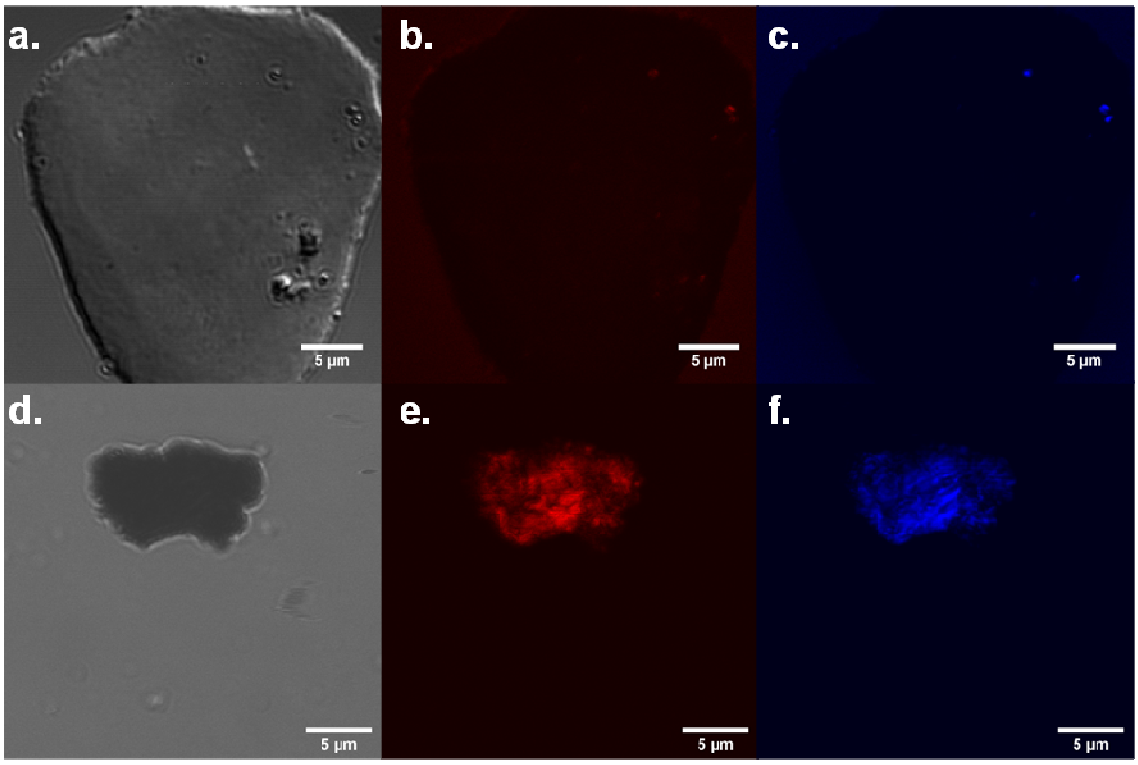

Figure 51. Images of particles from aqueous dispersions, after 6 hours sedimentation, obtained from optical transmittance (black/white) and LSCM excitation at ~2.28 eV (543 nm) (red) and ~1.96 eV (633 nm) (blue) of a-c) MS1 and d-f) MS2

3. Photoluminescence of Dispersions

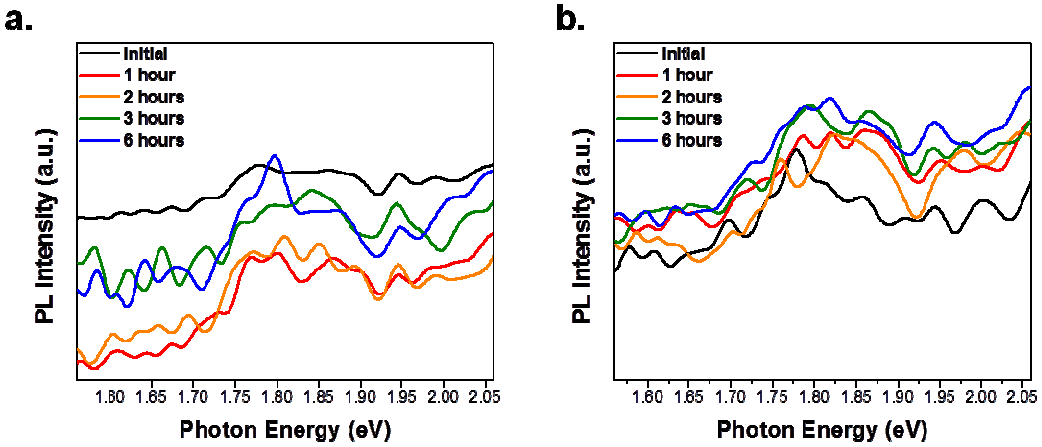

Figure 52. Normalized PL spectra from DMSO dispersions of a) MS1 and b) MS2

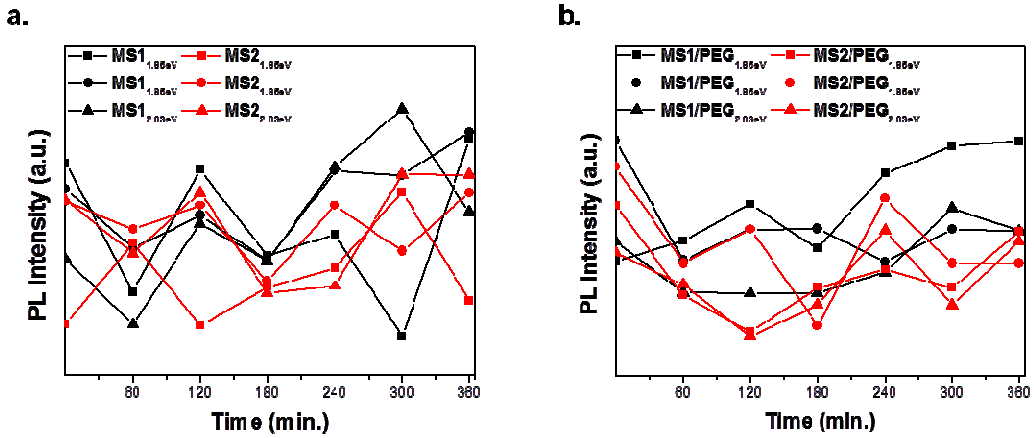

Figure 53. PL intensities at specific photon energies during the sedimentation process from aqueous dispersions of a) MS1 (black) and MS2 (red) and b) MS1/PEG (black) and MS2/PEG (red)

4. Optical Absorbance (UV-Vis) of Fragmented MoS_2/PEG solutions

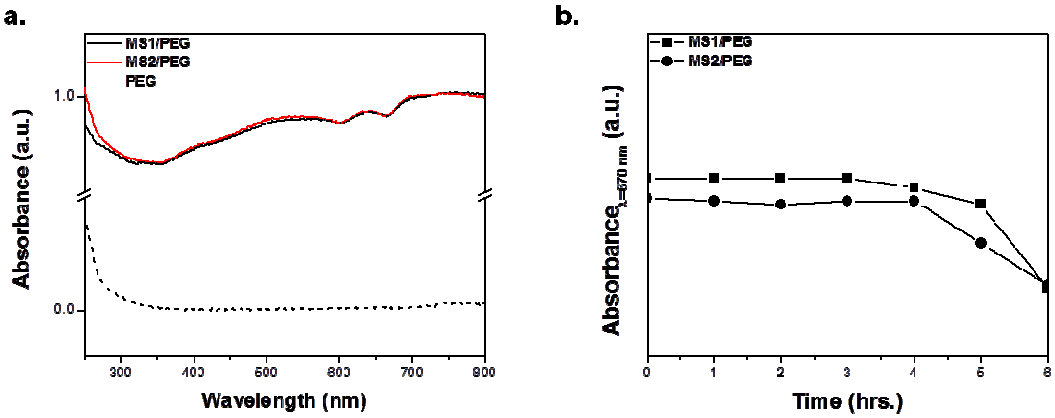

Figure 54. Optical absorbance plots of a) PEG solution (dashed line) and PEG-MS1 (black) and PEG-MS2 (red) dispersions (initial: solid line, after 6 hours: dotted lines), b) intensities at λ = 670 nm during the sedimentation process

CONCLUSION AND FUTURE WORK

Final Conclusion

Currently, research involving graphite and IGAs is expanding at a rapid pace. Techniques to isolate 2-D forms of these layered materials are still being developed including the liquid exfoliation method. However one major drawback of exfoliation methods is low yields of desirable materials. Incorporation of the 2-D and 3-D forms of these layered materials with various polymer matrices requires significant quantities, and has increased demand for new chemical routes for exfoliation and modification of the solid materials to enhance dispersion characteristics. Hence, we explored the use of liquid exfoliation of graphite, multilayered graphene, boron nitride, and molybdenum disulfide powders to obtain nearly quantitative yields of fragmented materials. Thorough analysis of chemical compositions, generated structures, and macroscopic properties of the obtained chemically fragmented powders demonstrated unique characteristics resulting from sonochemical processing. Solid-state and solution properties of the restacked powders should be further reflected in polymer composites. We are interested in developing tailored particles to increase dispersion in various polymer matrices, thereby providing a toolbox of particles for improving polymer properties.

The extensive experimental and applied work in this dissertation demonstrated a high-yielding chemical fragmentation process of bulk precursor powders. The use of low-boiling point solvents like $CHCl_3$ and IPA allows for easy removal of solvent after sonochemical fragmentation. From XPS data presented

in Chapter 1, the effects of sonochemical exfoliation appeared to generate chlorine functionalized graphite/multilayered graphene, and TEM images confirmed a variety of nested carbon nanostructures. As expected, the fragmentation process decreased the electrical conductivity of the powders due to induced oxygenation and poor contact between interlayer junctions. These processes are known to quench propagation of electrons through the sheets and between various sheets. Solution blending of dispersions was used to produce composites in a simple fashion. Also the thermal properties of rigid, polar/nonpolar polymer composites, containing various loadings of filler, suggested increased interaction with polar PMMA and significantly decreased interactions for nonpolar polymers like PS and PCHD.

Furthermore we extended the sonochemical fragmentation method to IGAs of h-BN and MoS_2 and systematically investigated the influence of chemical additives, specifically different antioxidants, using IPA as a dispersing medium. The introduction of antioxidant had limited effects on fragmented h-BN, however the properties of the fragmented graphite and MoS_2 samples changed. Redox-liquid fragmented graphite displayed better conductivity compared to the liquid fragmented sample, confirming that oxidation of sheet edges can be inhibited to preserve the sp^2 character of the sheets. Significant changes were observed for fragmented MoS_2 produced in the presence of sodium bisulfite. Results from various characterization methods, including XPS, ATR-FTIR, XRD, UV-Vis and TGA, suggested distinct preservation of MoS_2 composition and possible

intercalation of the material. The increase in thermal resistance (observed from TGA results) likely arose from removal of oxidized species thus preserving the inherent properties of MoS_2. Dielectric spectroscopy demonstrated unique behavior for sodium bisulfite fragmented MoS_2, which appeared to physisorb organic moieties. Aqueous dispersions of the fragmented MoS_2 particles displayed unique photoluminescence and lubricity in PEG solutions. The sonochemical fragmentation process appeared to significantly alter sedimentation which was reflected in the spectroscopic measurements. However further work to develop high-yielding filler chemistries to enhance composite properties in various polymers would be invaluable.

Future Work

As various particles and chemistries were explored using sonication to produce large quantities of fragmented filler materials, the subsequent detailed characterizations and analysis of properties gave insight into effective large-scale production. Given the novelty of the chemistry associated with these materials, almost infinite avenues of potential future research areas can be explored for developing polymer composites.

The major factor governing property enhancement in polymer composites is the interaction between the filler and polymer matrix. In order to utilize various functionalization chemistries, including both non-covalent and covalent, the general limitation in feasible methods results from large scale production for industrial applications. Generating particles of various sizes and shapes can

allow for tailored properties, whether from poor or excellent interfacial adhesions between fillers and polymers/solvent systems.

Considering all the necessary factors to produce large quantities of desirable materials for polymer composites, several potential routes can be undertaken for future work:

1. We observed significant changes in surface chemistries due to chemical reagents and solvents. The use of monomers as dispersing media could produce surface functionalized/intercalated moieties in the restacked samples. By choosing the exact (or chemically similar) monomer of the chosen host polymer, likely enhanced interaction would be observed. Chemical additives could be used to further enhance reactivity.

2. Simple sonication of the host polymer could generate functionalization due to degradation of the polymer. The dispersion characteristics could be compared to those using the host monomer, thereby providing critical information regarding the solubility parameters and solution blending conditions.

3. In Chapter 3, we noticed the effects of sonication conditions on photoluminescence and lubricity in PEG solutions. The differences in properties suggest the ability to tailor structures despite the variability from sonication itself. Optimization of conditions to produce tailored structures would be significant for a variety of applications.

4. As we have demonstrated, sonication created further defects in the materials and diminished some of the material properties. Comparing the resulting

properties and structures using other modification methods, such as ball milling, solid-state chemistries (oven annealing), and UV or microwave treatments, with sonication could offer insight to experiment design and conditions.

5. Finally, integration of various nanofillers in ppolymer composites would expand the toolbox of composite properties significantly. The determination of heterostructures and their intrinsic characteristics is considered the future in this field.[186] Developing protocols to enhance heterostructural dispersions in polymer systems could provide dual extremes of properties, as we observed the large insulatory behavior of fragmented h-BN and the good conductivity of fragmented graphene.

REFERENCES

1. Winey, K. I.; Vaia, R. A. Polymer Nanocomposites. *MRS Bull.* **2007**, *32*, 314-319.

2. F.M.P. The Manufacture of Artificial Graphite. *Nature* **1909**, *79*, 81-82.

3. Doyle, H. L. Colloidal Suspension of Graphite. *J. Phys. Chem.* **1913**, *17*, 390-401.

4. Bacon, R. Growth, Structure, and Properties of Graphite Whiskers. *J. Appl. Phys.* **1960**, *31*, 283-290.

5. Murayama, H.; Maeda, T. A Novel Form of Filamentous Graphite. *Nature* **1990**, *345*, 791-793.

6. Hiura, H.; Ebbesen, T. W.; Fujita, J.; Tanigaki, K.; Takada, T. Role of Sp(3) Defect Structures in Graphite and Carbon Nanotubes. *Nature* **1994**, *367*, 148-151.

7. Zhu, Y.; Murali, S.; Cai, W.; Li, X.; Suk, J. W.; Potts, J. R.; Ruoff, R. S. Graphene and Graphene Oxide: Synthesis, Properties, and Applications. *Adv. Mater.* **2010**, *22*, 3906-3924.

8. Compton, O. C.; Nguyen, S. T. Graphene Oxide, Highly Reduced Graphene Oxide, and Graphene: Versatile Building Blocks for Carbon-Based Materials. *Small* **2010**, *6*, 711-723.

9. Reina, A.; Jia, X. T.; Ho, J.; Nezich, D.; Son, H. B.; Bulovic, V.; Dresselhaus, M. S.; Kong, J. Large Area, Few-Layer Graphene Films on Arbitrary Substrates by Chemical Vapor Deposition. *Nano Lett.* **2009**, *9*, 30-35.

10. Sun, Z. Z.; Yan, Z.; Yao, J.; Beitler, E.; Zhu, Y.; Tour, J. M. Growth of Graphene from Solid Carbon Sources. *Nature* **2010**, *468*, 549-552.

11. Novoselov, K. S.; Geim, A. K.; Morozov, S. V.; Jiang, D.; Zhang, Y.; Dubonos, S. V.; Grigorieva, I. V.; Firsov, A. A. Electric Field Effect in Atomically Thin Carbon Films. *Science* **2004**, *306*, 666-669.

12. Geim, A. K.; Novoselov, K. S. The Rise of Graphene. *Nat. Mater.* **2007**, *6*, 183-191.

13. Rao, C. N. R.; Matte, H. S. S. R.; Maitra, U. Graphene Analogues of Inorganic Layered Materials. *Angew. Chem. Int. Ed.* **2013**, *52*, 13162-13185.

14. Rao, C. N. R.; Nag, A. Inorganic Analogues of Graphene. *Eur. J. Inorg. Chem.* **2010**, *2010*, 4244-4250.

15. Zhou, K. G.; Mao, N. N.; Wang, H. X.; Peng, Y.; Zhang, H. L. A Mixed-Solvent Strategy for Efficient Exfoliation of Inorganic Graphene Analogues. *Angew. Chem. Int. Ed.* **2011**, *50*, 10839-10842.

16. Rao, C. N. R.; Matte, H.; Subrahmanyam, K. S. Synthesis and Selected Properties of Graphene and Graphene Mimics. *Acc. Chem. Res.* **2013**, *46*, 149-159.

17. Novoselov, K. S.; Jiang, D.; Schedin, F.; Booth, T. J.; Khotkevich, V. V.; Morozov, S. V.; Geim, A. K. Two-Dimensional Atomic Crystals. *Proc. Natl. Acad. Sci. U.S.A.* **2005**, *102*, 10451-10453.

18. Golberg, D.; Bando, Y.; Huang, Y.; Terao, T.; Mitome, M.; Tang, C.; Zhi, C. Boron Nitride Nanotubes and Nanosheets. *ACS Nano* **2010**, *4*, 2979-2993.

19. Lin, Y.; Connell, J. W. Advances in 2d Boron Nitride Nanostructures: Nanosheets, Nanoribbons, Nanomeshes, and Hybrids with Graphene. *Nanoscale* **2012**, *4*, 6908-6939.

20. Pakdel, A.; Bando, Y.; Golberg, D. Nano Boron Nitride Flatland. *Chem. Soc. Rev.* **2014**, *43*, 934-959.

21. Haubner, R.; Wilhelm, M.; Weissenbacher, R.; Lux, B. Boron Nitrides — Properties, Synthesis and Applications. In *High Performance Non-Oxide Ceramics Ii*, Jansen, M., Ed. Springer Berlin Heidelberg: 2002; Vol. 102, pp 1-45.

22. Balmain, W. H. *J. Prakt. Chem.* **1842**, *27*, 422-430.

23. Corso, M.; Auwarter, W.; Muntwiler, M.; Tamai, A.; Greber, T.; Osterwalder, J. Boron Nitride Nanomesh. *Science* **2004**, *303*, 217-220.

24. Han, W. Q.; Wu, L. J.; Zhu, Y. M.; Watanabe, K.; Taniguchi, T. Structure of Chemically Derived Mono- and Few-Atomic-Layer Boron Nitride Sheets. *Appl. Phys. Lett.* **2008**, *93*.

25. Nag, A.; Raidongia, K.; Hembram, K.; Datta, R.; Waghmare, U. V.; Rao, C. N. R. Graphene Analogues of Bn: Novel Synthesis and Properties. *ACS Nano* **2010**, *4*, 1539-1544.

26. Li, L. H.; Chen, Y.; Behan, G.; Zhang, H. Z.; Petravic, M.; Glushenkov, A. M. Large-Scale Mechanical Peeling of Boron Nitride Nanosheets by Low-Energy Ball Milling. *J. Mater. Chem.* **2011**, *21*, 11862-11866.

27. Lin, Y.; Williams, T. V.; Connell, J. W. Soluble, Exfoliated Hexagonal Boron Nitride Nanosheets. *J. Phys. Chem. Lett* **2010**, *1*, 277-283.

28. Dickinson, R. G.; Pauling, L. The Crystal Structure of Molybdenite. *J. Am. Chem. Soc.* **1923**, *45*, 1466-1471.

29. Frindt, R. F. Single Crystals of Mos2 Several Molecular Layers Thick. *J. Appl. Phys.* **1966**, *37*, 1928-&.

30. Muller, A.; Diemann, E.; Branding, A.; Baumann, F. W.; Breysse, M.; Vrinat, M. New Method for the Preparation of Hydrodesulfurization Catalysts - Use of the Molybdenum Sulfur Cluster Compound (Nh4)2 Mo3ivs13. *Appl. Catal.* **1990**, *62*, L13-L17.

31. Liu, K. K.; Zhang, W. J.; Lee, Y. H.; Lin, Y. C.; Chang, M. T.; Su, C.; Chang, C. S.; Li, H.; Shi, Y. M.; Zhang, H.; Lai, C. S.; Li, L. J. Growth of Large-Area and Highly Crystalline Mos2 Thin Layers on Insulating Substrates. *Nano Lett.* **2012**, *12*, 1538-1544.

32. Zhan, Y. J.; Liu, Z.; Najmaei, S.; Ajayan, P. M.; Lou, J. Large-Area Vapor-Phase Growth and Characterization of Mos2 Atomic Layers on a Sio2 Substrate. *Small* **2012**, *8*, 966-971.

33. Lee, Y.-H.; Zhang, X.-Q.; Zhang, W.; Chang, M.-T.; Lin, C.-T.; Chang, K.-D.; Yu, Y.-C.; Wang, J. T.-W.; Chang, C.-S.; Li, L.-J.; Lin, T.-W. Synthesis of Large-Area Mos2 Atomic Layers with Chemical Vapor Deposition. *Adv. Mater.* **2012**, *24*, 2320-2325.

34. Mak, K. F.; Lee, C.; Hone, J.; Shan, J.; Heinz, T. F. Atomically Thin Mos2: A New Direct-Gap Semiconductor. *Phys. Rev. Lett.* **2010**, *105*.

35. Matte, H. S. S. R.; Gomathi, A.; Manna, A. K.; Late, D. J.; Datta, R.; Pati, S. K.; Rao, C. N. R. Mos2 and Ws2 Analogues of Graphene. *Angew. Chem. Int. Ed.* **2010**, *49*, 4059-4062.

36. Splendiani, A.; Sun, L.; Zhang, Y. B.; Li, T. S.; Kim, J.; Chim, C. Y.; Galli, G.; Wang, F. Emerging Photoluminescence in Monolayer Mos2. *Nano Lett.* **2010**, *10*, 1271-1275.

37. Wang, Q. H.; Kalantar-Zadeh, K.; Kis, A.; Coleman, J. N.; Strano, M. S. Electronics and Optoelectronics of Two-Dimensional Transition Metal Dichalcogenides. *Nat. Nanotech.* **2012**, *7*, 699-712.

38. Allam, I. M. Solid Lubricants for Applications at Elevated-Temperatures - a Review. *J. Mater. Sci.* **1991**, *26*, 3977-3984.

39. Lee, C.; Li, Q. Y.; Kalb, W.; Liu, X. Z.; Berger, H.; Carpick, R. W.; Hone, J. Frictional Characteristics of Atomically Thin Sheets. *Science* **2010**, *328*, 76-80.

40. Matte, H.; Maitra, U.; Kumar, P.; Rao, B. G.; Pramoda, K.; Rao, C. N. R. Synthesis, Characterization, and Properties of Few-Layer Metal Dichalcogenides and Their Nanocomposites with Noble Metal Particles, Polyaniline, and Reduced Graphene Oxide. *Z. Anorg. Allg. Chem.* **2012**, *638*, 2617-2624.

41. Zhou, K.; Jiang, S.; Bao, C.; Song, L.; Wang, B.; Tang, G.; Hu, Y.; Gui, Z. Preparation of Poly(Vinyl Alcohol) Nanocomposites with Molybdenum Disulfide (Mos2): Structural Characteristics and Markedly Enhanced Properties. *RSC Adv.* **2012**, *2*, 11695-11703.

42. Divigalpitiya, W. M. R.; Frindt, R. F.; Morrison, S. R. Inclusion Systems of Organic Molecules in Restacked Single-Layer Molybdenum Disulfide. *Science* **1989**, *246*, 369-371.

43. Hummers, W. S.; Offeman, R. E. Preparation of Graphitic Oxide. *J. Am. Chem. Soc.* **1958**, *80*, 1339-1339.

44. Gao, W.; Alemany, L. B.; Ci, L.; Ajayan, P. M. New Insights into the Structure and Reduction of Graphite Oxide. *Nat. Chem.* **2009**, *1*, 403-408.

45. Quintana, M.; Montellano, A.; Castillo, A. E. d. R.; Van Tendeloo, G.; Bittencourt, C.; Prato, M. Selective Organic Functionalization of Graphene Bulk or Graphene Edges. *Chem. Commun.* **2011**, *47*, 9330-9332.

46. Georgakilas, V.; Otyepka, M.; Bourlinos, A. B.; Chandra, V.; Kim, N.; Kemp, K. C.; Hobza, P.; Zboril, R.; Kim, K. S. Functionalization of Graphene: Covalent and Non-Covalent Approaches, Derivatives and Applications. *Chem. Rev.* **2012**, *112*, 6156-6214.

47. Kelly, K. F.; Billups, W. E. Synthesis of of Soluble Graphite and Graphene. *Acc. Chem. Res.* **2013**, *46*, 4-13.

48. Quintana, M.; Vazquez, E.; Prato, M. Organic Functionalization of Graphene in Dispersions. *Acc. Chem. Res.* **2013**, *46*, 138-148.

49. Economopoulos, S. P.; Rotas, G.; Miyata, Y.; Shinohara, H.; Tagmatarchis, N. Exfoliation and Chemical Modification Using Microwave Irradiation Affording Highly Functionalized Graphene. *ACS Nano* **2010**, *4*, 7499-7507.

50. Lin, Y.; Williams, T. V.; Cao, W.; Elsayed-Ali, H. E.; Connell, J. W. Defect Functionalization of Hexagonal Boron Nitride Nanosheets. *J. Phys. Chem. C* **2010**, *114*, 17434-17439.

51. Yu, J. H.; Huang, X. Y.; Wu, C.; Wu, X. F.; Wang, G. L.; Jiang, P. K. Interfacial Modification of Boron Nitride Nanoplatelets for Epoxy Composites with Improved Thermal Properties. *Polymer* **2012**, *53*, 471-480.

52. Sainsbury, T.; Satti, A.; May, P.; Wang, Z. M.; McGovern, I.; Gun'ko, Y. K.; Coleman, J. Oxygen Radical Functionalization of Boron Nitride Nanosheets. *J. Am. Chem. Soc.* **2012**, *134*, 18758-18771.

53. Sainsbury, T.; Satti, A.; May, P.; O'Neill, A.; Nicolosi, V.; Gun'ko, Y. K.; Coleman, J. N. Covalently Functionalized Hexagonal Boron Nitride Nanosheets by Nitrene Addition. *Chem. Eur. J.* **2012**, *18*, 10808-10812.

54. Simonov, K. A.; Vinogradov, N. A.; Ng, M. L.; Vinogradov, A. S.; Martensson, N.; Preobrajenski, A. B. Controllable Oxidation of H-Bn Monolayer on Ir(111) Studied by Core-Level Spectroscopies. *Surf. Sci.* **2012**, *606*, 564-570.

55. Whittingham, M. S. Chemistry of Intercalation Compounds - Metal Guests in Chalcogenide Hosts. *Prog. Solid State Chem.* **1978**, *12*, 41-99.

56. Chhowalla, M.; Shin, H. S.; Eda, G.; Li, L. J.; Loh, K. P.; Zhang, H. The Chemistry of Two-Dimensional Layered Transition Metal Dichalcogenide Nanosheets. *Nat. Chem.* **2013**, *5*, 263-275.

57. Huang, X.; Zeng, Z.; Zhang, H. Metal Dichalcogenide Nanosheets: Preparation, Properties and Applications. *Chem. Soc. Rev.* **2013**, *42*, 1934-1946.

58. Tsai, H. L.; Heising, J.; Schindler, J. L.; Kannewurf, C. R.; Kanatzidis, M. G. Exfoliated-Restacked Phase of Ws2. *Chem. Mater.* **1997**, *9*, 879-&.

59. Heising, J.; Kanatzidis, M. G. Exfoliated and Restacked Mos2 and Ws2: Ionic or Neutral Species? Encapsulation and Ordering of Hard Electropositive Cations. *J. Am. Chem. Soc.* **1999**, *121*, 11720-11732.

60. Wang, Y.; Ou, J. Z.; Balendhran, S.; Chrimes, A. F.; Mortazavi, M.; Yao, D. D.; Field, M. R.; Latham, K.; Bansal, V.; Friend, J. R.; Zhuiykov, S.; Medhekar, N. V.; Strano, M. S.; Kalantar-zadeh, K. Electrochemical Control of Photoluminescence in Two-Dimensional Mos2 Nanoflakes. *ACS Nano* **2013**, *7*, 10083-10093.

61. Yao, Y.; Tolentino, L.; Yang, Z.; Song, X.; Zhang, W.; Chen, Y.; Wong, C.-p. High-Concentration Aqueous Dispersions of Mos2. *Adv. Funct. Mater.* **2013**, *23*, 3577-3583.

62. Basavaraj, E.; Ramaraj, B.; Siddaramaiah. Polycarbonate/Molybdenum Disulfide/Carbon Black Composites: Physicomechanical, Thermal, Wear, and Morphological Properties. *Polym. Compos.* **2012**, *33*, 619-628.

63. Bissessur, R.; Liu, P. K. Y. Direct Insertion of Polypyrrole into Molybdenum Disulfide. *Solid State Ionics* **2006**, *177*, 191-196.

64. Golaz, B.; Tetouani, S.; Diomidis, N.; Michaud, V.; Mischler, S. Processing and Tribology of Thermoplastic Polyurethane Particulate Composite Materials. *J. Appl. Polym. Sci.* **2012**, *125*, 3745-3754.

65. Hu, K. H.; Hu, X. G.; Wang, J.; Xu, Y. F.; Han, C. L. Tribological Properties of Mos2 with Different Morphologies in High-Density Polyethylene. *Tribology Letters* **2012**, *47*, 79-90.

66. Kanatzidis, M. G.; Bissessur, R.; Degroot, D. C.; Schindler, J. L.; Kannewurf, C. R. New Intercalation Compounds of Conjugated Polymers - Encapsulation of Polyaniline in Mos2. *Chem. Mater.* **1993**, *5*, 595-596.

67. Kosidowski, L.; Powell, A. V. Naphthalene Intercalation into Molybdenum Disulfide. *Chem. Commun.* **1998**, 2201-2202.

68. Lin, B.-Z.; Ding, C.; Xu, B.-H.; Chen, Z.-J.; Chen, Y.-L. Preparation and Characterization of Polythiophene/Molybdenum Disulfide Intercalation Material. *Mater. Res. Bull.* **2009**, *44*, 719-723.

69. Jiang, S.-D.; Tang, G.; Bai, Z.-M.; Wang, Y.-Y.; Hu, Y.; Song, L. Surface Functionalization of Mos2 with Poss for Enhancing Thermal, Flame-Retardant and Mechanical Properties in Pva Composites. *RSC Adv.* **2014**, *4*, 3253-3262.

70. Suslick, K. S. Sonochemistry. *Science* **1990**, *247*, 1439-1445.

71. Didenko, Y. T.; Suslick, K. S. The Energy Efficiency of Formation of Photons, Radicals and Ions During Single-Bubble Cavitation. *Nature* **2002**, *418*, 394-397.

72. Xu, H. X.; Glumac, N. G.; Suslick, K. S. Temperature Inhomogeneity During Multibubble Sonoluminescence. *Angew. Chem. Int. Ed.* **2010**, *49*, 1079-1082.

73. Bang, J. H.; Suslick, K. S. Applications of Ultrasound to the Synthesis of Nanostructured Materials. *Adv. Mater.* **2010**, *22*, 1039-1059.

74. Cravotto, G.; Gaudino, E. C.; Cintas, P. On the Mechanochemical Activation by Ultrasound. *Chem. Soc. Rev.* **2013**, *42*, 7521-7534.

75. Xu, H.; Zeiger, B. W.; Suslick, K. S. Sonochemical Synthesis of Nanomaterials. *Chem. Soc. Rev.* **2013**, *42*, 2555-2567.

76. Guittonneau, F.; Abdelouas, A.; Grambow, B.; Huclier, S. The Effect of High Power Ultrasound on an Aqueous Suspension of Graphite. *Ultrason. Sonochem.* **2010**, *17*, 391-398.

77. Hernandez, Y.; Nicolosi, V.; Lotya, M.; Blighe, F. M.; Sun, Z.; De, S.; McGovern, I. T.; Holland, B.; Byrne, M.; Gun'ko, Y. K.; Boland, J. J.; Niraj, P.; Duesberg, G.; Krishnamurthy, S.; Goodhue, R.; Hutchison, J.; Scardaci, V.; Ferrari, A. C.; Coleman, J. N. High-Yield Production of Graphene by Liquid-Phase Exfoliation of Graphite. *Nat. Nanotech.* **2008**, *3*, 563-568.

78. Khan, U.; O'Neill, A.; Lotya, M.; De, S.; Coleman, J. N. High-Concentration Solvent Exfoliation of Graphene. *Small* **2010**, *6*, 864-871.

79. Lotya, M.; Hernandez, Y.; King, P. J.; Smith, R. J.; Nicolosi, V.; Karlsson, L. S.; Blighe, F. M.; De, S.; Wang, Z.; McGovern, I. T.; Duesberg, G. S.; Coleman, J. N. Liquid Phase Production of Graphene by Exfoliation of Graphite in Surfactant/Water Solutions. *J. Am. Chem. Soc.* **2009**, *131*, 3611-3620.

80. Hernandez, Y.; Lotya, M.; Rickard, D.; Bergin, S. D.; Coleman, J. N. Measurement of Multicomponent Solubility Parameters for Graphene Facilitates Solvent Discovery. *Langmuir* **2010**, *26*, 3208-3213.

81. Cravotto, G.; Cintas, P. Sonication-Assisted Fabrication and Post-Synthetic Modifications of Graphene-Like Materials. *Chemistry – A European Journal* **2010**, *16*, 5246-5259.

82. O'Neill, A.; Khan, U.; Nirmalraj, P. N.; Boland, J.; Coleman, J. N. Graphene Dispersion and Exfoliation in Low Boiling Point Solvents. *J. Phys. Chem. C* **2011**, *115*, 5422-5428.

83. Zhi, C.; Bando, Y.; Tang, C.; Kuwahara, H.; Golberg, D. Large-Scale Fabrication of Boron Nitride Nanosheets and Their Utilization in Polymeric Composites with Improved Thermal and Mechanical Properties. *Adv. Mater.* **2009**, *21*, 2889-2893.

84. Joensen, P.; Frindt, R. F.; Morrison, S. R. Single-Layer Mos2. *Mater. Res. Bull.* **1986**, *21*, 457-461.

85. Coleman, J. N.; Lotya, M.; O'Neill, A.; Bergin, S. D.; King, P. J.; Khan, U.; Young, K.; Gaucher, A.; De, S.; Smith, R. J.; Shvets, I. V.; Arora, S. K.; Stanton, G.; Kim, H.-Y.; Lee, K.; Kim, G. T.; Duesberg, G. S.; Hallam, T.; Boland, J. J.; Wang, J. J.; Donegan, J. F.; Grunlan, J. C.; Moriarty, G.; Shmeliov, A.; Nicholls, R. J.; Perkins, J. M.; Grieveson, E. M.; Theuwissen, K.; McComb, D. W.; Nellist, P. D.; Nicolosi, V. Two-Dimensional Nanosheets Produced by Liquid Exfoliation of Layered Materials. *Science* **2011**, *331*, 568-571.

86. Cunningham, G.; Lotya, M.; Cucinotta, C. S.; Sanvito, S.; Bergin, S. D.; Menzel, R.; Shaffer, M. S. P.; Coleman, J. N. Solvent Exfoliation of Transition Metal Dichalcogenides: Dispersibility of Exfoliated Nanosheets Varies Only Weakly between Compounds. *ACS Nano* **2012**, *6*, 3468-3480.

87. Smith, R. J.; King, P. J.; Lotya, M.; Wirtz, C.; Khan, U.; De, S.; O'Neill, A.; Duesberg, G. S.; Grunlan, J. C.; Moriarty, G.; Chen, J.; Wang, J. Z.; Minett, A. I.; Nicolosi, V.; Coleman, J. N. Large-Scale Exfoliation of Inorganic Layered Compounds in Aqueous Surfactant Solutions. *Adv. Mater.* **2011**, *23*, 3944-+.

88. O'Neill, A.; Khan, U.; Coleman, J. N. Preparation of High Concentration Dispersions of Exfoliated Mos2 with Increased Flake Size. *Chem. Mater.* **2012**, *24*, 2414-2421.

89. Xu, H.; Suslick, K. S. Sonochemical Preparation of Functionalized Graphenes. *J. Am. Chem. Soc.* **2011**, *133*, 9148-9151.

90. Shen, B.; Zhai, W. T.; Lu, D. D.; Wang, J.; Zheng, W. G. Ultrasonication-Assisted Direct Functionalization of Graphene with Macromolecules. *RSC Adv.* **2012**, *2*, 4713-4719.

91. Lin, Y.; Williams, T. V.; Xu, T. B.; Cao, W.; Elsayed-Ali, H. E.; Connell, J. W. Aqueous Dispersions of Few-Layered and Monolayered Hexagonal Boron Nitride Nanosheets from Sonication-Assisted Hydrolysis: Critical Role of Water. *J. Phys. Chem. C* **2011**, *115*, 2679-2685.

92. Zheng, J.; Zhang, H.; Dong, S.; Liu, Y.; Tai Nai, C.; Suk Shin, H.; Young Jeong, H.; Liu, B.; Ping Loh, K. High Yield Exfoliation of Two-Dimensional Chalcogenides Using Sodium Naphthalenide. *Nat Commun* **2014**, *5*.

93. Barboza, A. P. M.; Chacham, H.; Oliveira, C. K.; Fernandes, T. F. D.; Ferreira, E. H. M.; Archanjo, B. S.; Batista, R. J. C.; de Oliveira, A. B.; Neves, B. R. A. Dynamic Negative Compressibility of Few-Layer Graphene, H-Bn, and Mos2. *Nano Lett.* **2012**, *12*, 2313-2317.

94. Gao, G. H.; Gao, W.; Cannuccia, E.; Taha-Tijerina, J.; Balicas, L.; Mathkar, A.; Narayanan, T. N.; Liu, Z.; Gupta, B. K.; Peng, J.; Yin, Y. S.; Rubio, A.; Ajayan, P. M. Artificially Stacked Atomic Layers: Toward New Van Der Waals Solids. *Nano Lett.* **2012**, *12*, 3518-3525.

95. Kim, H.; Abdala, A. A.; Macosko, C. W. Graphene/Polymer Nanocomposites. *Macromolecules* **2010**, *43*, 6515-6530.

96. Osada, M.; Sasaki, T. Two-Dimensional Dielectric Nanosheets: Novel Nanoelectronics from Nanocrystal Building Blocks. *Adv. Mater.* **2012**, *24*, 210-228.

97. Osterloh, F. E. Inorganic Nanostructures for Photoelectrochemical and Photocatalytic Water Splitting. *Chem. Soc. Rev.* **2013**, *42*, 2294-2320.

98. Potts, J. R.; Dreyer, D. R.; Bielawski, C. W.; Ruoff, R. S. Graphene-Based Polymer Nanocomposites. *Polymer* **2011**, *52*, 5-25.

99. Ramanathan, T.; Abdala, A. A.; Stankovich, S.; Dikin, D. A.; Herrera-Alonso, M.; Piner, R. D.; Adamson, D. H.; Schniepp, H. C.; Chen, X.; Ruoff, R. S.; Nguyen, S. T.; Aksay, I. A.; Prud'homme, R. K.; Brinson, L. C. Functionalized Graphene Sheets for Polymer Nanocomposites. *Nat. Nanotech.* **2008**, *3*, 327-331.

100. Rao, C. N. R.; Matte, H.; Subrahmanyam, K. S.; Maitra, U. Unusual Magnetic Properties of Graphene and Related Materials. *Chemical Science* **2012**, *3*, 45-52.

101. Song, L.; Balicas, L.; Mowbray, D. J.; Capaz, R. B.; Storr, K.; Ci, L.; Jariwala, D.; Kurth, S.; Louie, S. G.; Rubio, A.; Ajayan, P. M. Anomalous Insulator-Metal Transition in Boron Nitride-Graphene Hybrid Atomic Layers. *Phys. Rev. B* **2012**, *86*.

102. Song, L.; Liu, Z.; Reddy, A. L. M.; Narayanan, N. T.; Taha-Tijerina, J.; Peng, J.; Gao, G. H.; Lou, J.; Vajtai, R.; Ajayan, P. M. Binary and Ternary Atomic Layers Built from Carbon, Boron, and Nitrogen. *Adv. Mater.* **2012**, *24*, 4878-4895.

103. Stankovich, S.; Dikin, D. A.; Dommett, G. H. B.; Kohlhaas, K. M.; Zimney, E. J.; Stach, E. A.; Piner, R. D.; Nguyen, S. T.; Ruoff, R. S. Graphene-Based Composite Materials. *Nature* **2006**, *442*, 282-286.

104. Sundaresan, A.; Rao, C. N. R. Implications and Consequences of Ferromagnetism Universally Exhibited by Inorganic Nanoparticles. *Solid State Commun.* **2009**, *149*, 1197-1200.

105. Verdejo, R.; Bernal, M. M.; Romasanta, L. J.; Lopez-Manchado, M. A. Graphene Filled Polymer Nanocomposites. *J. Mater. Chem.* **2011**, *21*, 3301-3310.

106. Winter, M.; Novák, P.; Monnier, A. Graphites for Lithium-Ion Cells: The Correlation of the First-Cycle Charge Loss with the Brunauer-Emmett-Teller Surface Area. *J. Electrochem. Soc.* **1998**, *145*, 428-436.

107. Xu, M.; Liang, T.; Shi, M.; Chen, H. Graphene-Like Two-Dimensional Materials. *Chem. Rev.* **2013**.

108. Zhou, J.; Wang, Q.; Sun, Q.; Jena, P. Electronic and Magnetic Properties of a Bn Sheet Decorated with Hydrogen and Fluorine. *Phys. Rev. B* **2010**, *81*.

109. Gong, L.; Kinloch, I. A.; Young, R. J.; Riaz, I.; Jalil, R.; Novoselov, K. S. Interfacial Stress Transfer in a Graphene Monolayer Nanocomposite. *Adv. Mater.* **2010**, *22*, 2694-2697.

110. May, P.; Khan, U.; O'Neill, A.; Coleman, J. N. Approaching the Theoretical Limit for Reinforcing Polymers with Graphene. *J. Mater. Chem.* **2012**, *22*, 1278-1282.

111. Khan, U.; May, P.; O'Neill, A.; Bell, A. P.; Boussac, E.; Martin, A.; Semple, J.; Coleman, J. N. Polymer Reinforcement Using Liquid-Exfoliated Boron Nitride Nanosheets. *Nanoscale* **2013**, *5*, 581-587.

112. Sakellariou, G.; Priftis, D.; Baskaran, D. Surface-Initiated Polymerization from Carbon Nanotubes: Strategies and Perspectives. *Chem. Soc. Rev.* **2013**, *42*, 677-704.

113. Sakellariou, G.; Ji, H. N.; Mays, J. W.; Baskaran, D. Enhanced Polymer Grafting from Multiwalled Carbon Nanotubes through Living Anionic Surface-Initiated Polymerization. *Chem. Mater.* **2008**, *20*, 6217-6230.

114. Priftis, D.; Petzetakis, N.; Sakellariou, G.; Pitsikalis, M.; Baskaran, D.; Mays, J. W.; Hadjichristidis, N. Surface-Initiated Titanium-Mediated Coordination Polymerization from Catalyst-Functionalized Single and Multiwalled Carbon Nanotubes. *Macromolecules* **2009**, *42*, 3340-3346.

115. Mutz, M.; Holley, D. W.; Baskaran, D.; Mays, J. W.; Dadmun, M. D. Impact of Nanoparticle Size and Shape on Selective Surface Segregation in Polymer Nanocomposites. *Polymer* **2012**, *53*, 5087-5096.

116. Priftis, D.; Sakellariou, G.; Baskaran, D.; Mays, J. W.; Hadjichristidis, N. Polymer Grafted Janus Multi-Walled Carbon Nanotubes. *Soft Matter* **2009**, *5*, 4272-4278.

117. Yoonessi, M.; Gaier, J. R. Highly Conductive Multifunctional Graphene Polycarbonate Nanocomposites. *ACS Nano* **2010**, *4*, 7211-7220.

118. Geim, A. K.; Novoselov, K. S. The Rise of Graphene. *Nat Mater* **2007**, *6*, 183-91.

119. Blake, P.; Brimicombe, P. D.; Nair, R. R.; Booth, T. J.; Jiang, D.; Schedin, F.; Ponomarenko, L. A.; Morozov, S. V.; Gleeson, H. F.; Hill, E. W.; Geim, A. K.; Novoselov, K. S. Graphene-Based Liquid Crystal Device. *Nano Lett.* **2008**, *8*, 1704-1708.

120. Booth, T. J.; Blake, P.; Nair, R. R.; Jiang, D.; Hill, E. W.; Bangert, U.; Bleloch, A.; Gass, M.; Novoselov, K. S.; Katsnelson, M. I.; Geim, A. K. Macroscopic Graphene Membranes and Their Extraordinary Stiffness. *Nano Lett.* **2008**, *8*, 2442-2446.

121. Meyer, J. C.; Geim, A. K.; Katsnelson, M. I.; Novoselov, K. S.; Booth, T. J.; Roth, S. The Structure of Suspended Graphene Sheets. *Nature* **2007**, *446*, 60-63.

122. Zhang, Y. B.; Tan, Y. W.; Stormer, H. L.; Kim, P. Experimental Observation of the Quantum Hall Effect and Berry's Phase in Graphene. *Nature* **2005**, *438*, 201-204.

123. Eda, G.; Fanchini, G.; Chhowalla, M. Large-Area Ultrathin Films of Reduced Graphene Oxide as a Transparent and Flexible Electronic Material. *Nat. Nanotech.* **2008**, *3*, 270-274.

124. Mattevi, C.; Eda, G.; Agnoli, S.; Miller, S.; Mkhoyan, K. A.; Celik, O.; Mastrogiovanni, D.; Granozzi, G.; Garfunkel, E.; Chhowalla, M. Evolution of Electrical, Chemical, and Structural Properties of Transparent and Conducting Chemically Derived Graphene Thin Films. *Adv. Funct. Mater.* **2009**, *19*, 2577-2583.

125. Park, S.; An, J.; Potts, J. R.; Velamakanni, A.; Murali, S.; Ruoff, R. S. Hydrazine-Reduction of Graphite- and Graphene Oxide. *Carbon* **2011**, *49*, 3019-3023.

126. Shin, H.-J.; Kim, K. K.; Benayad, A.; Yoon, S.-M.; Park, H. K.; Jung, I.-S.; Jin, M. H.; Jeong, H.-K.; Kim, J. M.; Choi, J.-Y.; Lee, Y. H. Efficient Reduction of Graphite Oxide by Sodium Borohydride and Its Effect on Electrical Conductance. *Adv. Funct. Mater.* **2009**, *19*, 1987-1992.

127. Stankovich, S.; Dikin, D. A.; Piner, R. D.; Kohlhaas, K. A.; Kleinhammes, A.; Jia, Y.; Wu, Y.; Nguyen, S. T.; Ruoff, R. S. Synthesis of Graphene-Based Nanosheets Via Chemical Reduction of Exfoliated Graphite Oxide. *Carbon* **2007**, *45*, 1558-1565.

128. Paredes, J. I.; Villar-Rodil, S.; Martinez-Alonso, A.; Tascon, J. M. D. Graphene Oxide Dispersions in Organic Solvents. *Langmuir* **2008**, *24*, 10560-10564.

129. Park, S.; An, J.; Jung, I.; Piner, R. D.; An, S. J.; Li, X.; Velamakanni, A.; Ruoff, R. S. Colloidal Suspensions of Highly Reduced Graphene Oxide in a Wide Variety of Organic Solvents. *Nano Lett.* **2009**, *9*, 1593-1597.

130. Lee, J. H.; Shin, D. W.; Makotchenko, V. G.; Nazarov, A. S.; Fedorov, V. E.; Kim, Y. H.; Choi, J.-Y.; Kim, J. M.; Yoo, J.-B. One-Step Exfoliation Synthesis of Easily Soluble Graphite and Transparent Conducting Graphene Sheets. *Adv. Mater.* **2009**, *21*, 4383-4387.

131. Widenkvist, E.; Boukhvalov, D. W.; Rubino, S.; Akhtar, S.; Lu, J.; Quinlan, R. A.; Katsnelson, M. I.; Leifer, K.; Grennberg, H.; Jansson, U. Mild Sonochemical Exfoliation of Bromine-Intercalated Graphite: A New Route Towards Graphene. *Journal of Physics D-Applied Physics* **2009**, *42*.

132. Bourlinos, A. B.; Georgakilas, V.; Zboril, R.; Steriotis, T. A.; Stubos, A. K. Liquid-Phase Exfoliation of Graphite Towards Solubilized Graphenes. *Small* **2009**, *5*, 1841-1845.

133. Bourlinos, A. B.; Georgakilas, V.; Zboril, R.; Steriotis, T. A.; Stubos, A. K.; Trapalis, C. Aqueous-Phase Exfoliation of Graphite in the Presence of Polyvinylpyrrolidone for the Production of Water-Soluble Graphenes. *Solid State Commun.* **2009**, *149*, 2172-2176.

134. Coleman, J. N. Liquid-Phase Exfoliation of Nanotubes and Graphene. *Adv. Funct. Mater.* **2009**, *19*, 3680-3695.

135. Coleman, J. N. Liquid Exfoliation of Defect-Free Graphene. *Acc. Chem. Res.* **2013**, *46*, 14-22.

136. Lotya, M.; King, P. J.; Khan, U.; De, S.; Coleman, J. N. High-Concentration, Surfactant-Stabilized Graphene Dispersions. *ACS Nano* **2010**, *4*, 3155-3162.

137. Cai, M. Z.; Thorpe, D.; Adamson, D. H.; Schniepp, H. C. Methods of Graphite Exfoliation. *J. Mater. Chem.* **2012**, *22*, 24992-25002.

138. Khan, U.; Porwal, H.; O'Neill, A.; Nawaz, K.; May, P.; Coleman, J. N. Solvent-Exfoliated Graphene at Extremely High Concentration. *Langmuir* **2011**, *27*, 9077-9082.

139. Khan, U.; O'Neill, A.; Porwal, H.; May, P.; Nawaz, K.; Coleman, J. N. Size Selection of Dispersed, Exfoliated Graphene Flakes by Controlled Centrifugation. *Carbon* **2012**, *50*, 470-475.

140. Hong, K. L.; Mays, J. W. 1,3-Cyclohexadiene Polymers. 1. Anionic Polymerization. *Macromolecules* **2001**, *34*, 782-786.

141. Bhatnagar, A.; Cheung, H. M. Sonochemical Destruction of Chlorinated-C1 and Chlorinated-C2 Volatile Organic-Compounds in Dilute Aqueous-Solution. *Environmental Science & Technology* **1994**, *28*, 1481-1486.

142. Wu, J. M.; Huang, H. S.; Livengood, C. D. Ultrasonic Destruction of Chlorinated Compounds in Aqueous-Solution. *Environ. Prog.* **1992**, *11*, 195-201.

143. Lim, M.; Son, Y.; Khim, J. Frequency Effects on the Sonochemical Degradation of Chlorinated Compounds. *Ultrason. Sonochem.* **2011**, *18*, 460-465.

144. Wang, S.; Tang, L. A. l.; Bao, Q.; Lin, M.; Deng, S.; Goh, B. M.; Loh, K. P. Room-Temperature Synthesis of Soluble Carbon Nanotubes by the Sonication of Graphene Oxide Nanosheets. *J. Am. Chem. Soc.* **2009**, *131*, 16832-16837.

145. Subrahmanyam, K. S.; Vivekchand, S. R. C.; Govindaraj, A.; Rao, C. N. R. A Study of Graphenes Prepared by Different Methods: Characterization, Properties and Solubilization. *J. Mater. Chem.* **2008**, *18*, 1517-1523.

146. Hontorialucas, C.; Lopezpeinado, A. J.; Lopezgonzalez, J. D. D.; Rojascervantes, M. L.; Martinaranda, R. M. Study of Oxygen-Containing Groups in a Series of Graphite Oxides - Physical and Chemical Characterization. *Carbon* **1995**, *33*, 1585-1592.

147. Flett, M. S. C. 216. The Characteristic Infra-Red Frequencies of the Carboxylic Acid Group. *Journal of the Chemical Society (Resumed)* **1951**, *0*, 962-967.

148. Neagle, W.; Rochester, C. H. Infrared Study of the Adsorption of Ethanoic Acid and Trifluoroethanoic Acid on Barium Sulphate. *Journal of the Chemical Society, Faraday Transactions 1: Physical Chemistry in Condensed Phases* **1989**, *85*, 429-439.

149. Krishna, C. M.; Kondo, T.; Riesz, P. Sonochemistry of Alcohol-Water Mixtures - Spin-Trapping Evidence for Thermal-Decomposition and Isotope-Exchange Reactions. *J. Phys. Chem.* **1989**, *93*, 5166-5172.

150. Misik, V.; Riesz, P. Free-Radical Formation by Ultrasound in Organic Liquids - a Spin-Trapping and Epr Study. *J. Phys. Chem.* **1994**, *98*, 1634-1640.

151. Pimenta, M. A.; Dresselhaus, G.; Dresselhaus, M. S.; Cancado, L. G.; Jorio, A.; Saito, R. Studying Disorder in Graphite-Based Systems by Raman Spectroscopy. *PCCP* **2007**, *9*, 1276-1291.

152. Ferrari, A. C. Raman Spectroscopy of Graphene and Graphite: Disorder, Electron-Phonon Coupling, Doping and Nonadiabatic Effects. *Solid State Commun.* **2007**, *143*, 47-57.

153. Jiang, W.; Nadeau, G.; Zaghib, K.; Kinoshita, K. Thermal Analysis of the Oxidation of Natural Graphite — Effect of Particle Size. *Thermochim. Acta* **2000**, *351*, 85-93.

154. Quintana, M.; Grzelczak, M.; Spyrou, K.; Calvaresi, M.; Bals, S.; Kooi, B.; Van Tendeloo, G.; Rudolf, P.; Zerbetto, F.; Prato, M. A Simple Road for the Transformation of Few-Layer Graphene into Mwnts. *J. Am. Chem. Soc.* **2012**, *134*, 13310-13315.

155. Xie, X.; Ju, L.; Feng, X. F.; Sun, Y. H.; Zhou, R. F.; Liu, K.; Fan, S. S.; Li, Q. L.; Jiang, K. L. Controlled Fabrication of High-Quality Carbon Nanoscrolls from Monolayer Graphene. *Nano Lett.* **2009**, *9*, 2565-2570.

156. Khan, U.; O'Neill, A.; Porwal, H.; May, P.; Nawaz, K.; Coleman, J. N. Size Selection of Dispersed, Exfoliated Graphene Flakes by Controlled Centrifugation. *Carbon* **2012**, *50*, 470-475.

157. Jin, M.; Kim, T. H.; Lim, S. C.; Duong, D. L.; Shin, H. J.; Jo, Y. W.; Jeong, H. K.; Chang, J.; Xie, S.; Lee, Y. H. Facile Physical Route to Highly Crystalline Graphene. *Adv. Funct. Mater.* **2011**, *21*, 3496-3501.

158. Krishnamoorthy, K.; Kim, G.-S.; Kim, S. J. Graphene Nanosheets: Ultrasound Assisted Synthesis and Characterization. *Ultrason. Sonochem.* **2013**, *20*, 644-649.

159. Li, J. L.; Peng, Q. S.; Bai, G. Z.; Jiang, W. Carbon Scrolls Produced by High Energy Ball Milling of Graphite. *Carbon* **2005**, *43*, 2830-2833.

160. Viculis, L. M.; Mack, J. J.; Kaner, R. B. A Chemical Route to Carbon Nanoscrolls. *Science* **2003**, *299*, 1361.

161. Chen, X. H.; Yang, H. S.; Wu, G. T.; Wang, M.; Deng, F. M.; Zhang, X. B.; Peng, J. C.; Li, W. Z. Generation of Curved or Closed-Shell Carbon Nanostructures by Ball-Milling of Graphite. *J. Cryst. Growth* **2000**, *218*, 57-61.

162. Huang, J. Y.; Yasuda, H.; Mori, H. Highly Curved Carbon Nanostructures Produced by Ball-Milling. *Chem. Phys. Lett.* **1999**, *303*, 130-134.

163. Warner, J. H.; Ru□mmeli, M. H.; Gemming, T.; Bu□chner, B.; Briggs, G. A. D. Direct Imaging of Rotational Stacking Faults in Few Layer Graphene. *Nano Lett.* **2008**, *9*, 102-106.

164. Wilson, N. R.; Pandey, P. A.; Beanland, R.; Young, R. J.; Kinloch, I. A.; Gong, L.; Liu, Z.; Suenaga, K.; Rourke, J. P.; York, S. J.; Sloan, J. Graphene Oxide: Structural Analysis and Application as a Highly Transparent Support for Electron Microscopy. *ACS Nano* **2009**, *3*, 2547-2556.

165. Robertson, A. W.; Warner, J. H. Hexagonal Single Crystal Domains of Few-Layer Graphene on Copper Foils. *Nano Lett.* **2011**, *11*, 1182-1189.

166. Iijima, S. Helical Microtubules of Graphitic Carbon. *Nature* **1991**, *354*, 56-58.

167. Zhu, W. Z.; Miser, D. E.; Chan, W. G.; Hajaligol, M. R. Characterization of Multiwalled Carbon Nanotubes Prepared by Carbon Arc Cathode Deposit. *Mater. Chem. Phys.* **2003**, *82*, 638-647.

168. Li, Z. Q.; Lu, C. J.; Xia, Z. P.; Zhou, Y.; Luo, Z. X-Ray Diffraction Patterns of Graphite and Turbostratic Carbon. *Carbon* **2007**, *45*, 1686-1695.

169. Natarajan, C.; Fujimoto, H.; Mabuchi, A.; Tokumitsu, K.; Kasuh, T. Effect of Mechanical Milling of Graphite Powder on Lithium Intercalation Properties. *J. Power Sources* **2001**, *92*, 187-192.

170. Roy, D.; Angeles-Tactay, E.; Brown, R. J. C.; Spencer, S. J.; Fry, T.; Dunton, T. A.; Young, T.; Milton, M. J. T. Synthesis and Raman Spectroscopic Characterisation of Carbon Nanoscrolls. *Chem. Phys. Lett.* **2008**, *465*, 254-257.

171. Wei, X. H.; Liu, L.; Zhang, J. X.; Shi, J. L.; Guo, Q. G. Mechanical, Electrical, Thermal Performances and Structure Characteristics of Flexible Graphite Sheets. *J. Mater. Sci.* **2010**, *45*, 2449-2455.

172. Jeong, H.-K.; Lee, Y. P.; Lahaye, R. J. W. E.; Park, M.-H.; An, K. H.; Kim, I. J.; Yang, C.-W.; Park, C. Y.; Ruoff, R. S.; Lee, Y. H. Evidence of Graphitic Ab Stacking Order of Graphite Oxides. *J. Am. Chem. Soc.* **2008**, *130*, 1362-1366.

173. Celzard, A.; Krzesinska, M.; Begin, D.; Mareche, J. F.; Puricelli, S.; Furdin, G. Preparation, Electrical and Elastic Properties of New Anisotropic Expanded Graphite-Based Composites. *Carbon* **2002**, *40*, 557-566.

174. Deprez, N.; McLachlan, D. S. The Analysis of the Electrical-Conductivity of Graphite Powders During Compaction. *Journal of Physics D-Applied Physics* **1988**, *21*, 101-107.

175. Woltornist, S. J.; Oyer, A. J.; Carrillo, J.-M. Y.; Dobrynin, A. V.; Adamson, D. H. Conductive Thin Films of Pristine Graphene by Solvent Interface Trapping. *ACS Nano* **2013**.

176. Paulson, S.; Helser, A.; Nardelli, M. B.; Taylor, R. M.; Falvo, M.; Superfine, R.; Washburn, S. Tunable Resistance of a Carbon Nanotube-Graphite Interface. *Science* **2000**, *290*, 1742-1744.

177. Khan, U.; O'Connor, I.; Gun'ko, Y. K.; Coleman, J. N. The Preparation of Hybrid Films of Carbon Nanotubes and Nano-Graphite/Graphene with Excellent Mechanical and Electrical Properties. *Carbon* **2010**, *48*, 2825-2830.

178. Nicolosi, V.; Vrbanic, D.; Mrzel, A.; McCauley, J.; O'Flaherty, S.; Mihailovic, D.; Blau, W. J.; Coleman, J. N. Solubility of Mo6s4.5i4.5 Nanowires. *Chem. Phys. Lett.* **2005**, *401*, 13-18.

179. Wajid, A. S.; Das, S.; Irin, F.; Ahmed, H. S. T.; Shelburne, J. L.; Parviz, D.; Fullerton, R. J.; Jankowski, A. F.; Hedden, R. C.; Green, M. J. Polymer-Stabilized Graphene Dispersions at High Concentrations in Organic Solvents for Composite Production. *Carbon* **2012**, *50*, 526-534.

180. Skaltsas, T.; Karousis, N.; Yan, H.-J.; Wang, C.-R.; Pispas, S.; Tagmatarchis, N. Graphene Exfoliation in Organic Solvents and Switching Solubility in Aqueous Media with the Aid of Amphiphilic Block Copolymers. *Journal of Materials Chemistry* **2012**, *22*, 21507-21512.

181. Ugarte, D. Curling and Closure of Graphitic Networks under Electron-Beam Irradiation. *Nature* **1992**, *359*, 707-709.

182. Li, B.; Zhong, W.-H. Review on Polymer/Graphite Nanoplatelet Nanocomposites. *J. Mater. Sci.* **2011**, *46*, 5595-5614.

183. Viculis, L. M.; Mack, J. J.; Mayer, O. M.; Hahn, H. T.; Kaner, R. B. Intercalation and Exfoliation Routes to Graphite Nanoplatelets. *J. Mater. Chem.* **2005**, *15*, 974-978.

184. Papirer, E.; Lacroix, R.; Donnet, J. B.; Nanse, G.; Fioux, P. Xps Study of the Halogenation of Carbon-Black .2. Chlorination. *Carbon* **1995**, *33*, 63-72.

185. Hughes, J. M.; Aherne, D.; Coleman, J. N. Generalizing Solubility Parameter Theory to Apply to One- and Two-Dimensional Solutes and to Incorporate Dipolar Interactions. *J. Appl. Polym. Sci.* **2013**, *127*, 4483-4491.

186. Geim, A. K.; Grigorieva, I. V. Van Der Waals Heterostructures. *Nature* **2013**, *499*, 419-425.

187. Georgakilas, V.; Bourlinos, A. B.; Zboril, R.; Steriotis, T. A.; Dallas, P.; Stubos, A. K.; Trapalis, C. Organic Functionalisation of Graphenes. *Chem. Commun.* **2010**, *46*, 1766-1768.

188. Jeong, S.; Han, J. H.; Jang, J.-t.; Seo, J.-w.; Kim, J.-G.; Cheon, J. Transformative Two-Dimensional Layered Nanocrystals. *J. Am. Chem. Soc.* **2011**, *133*, 14500-14503.

189. Ci, L.; Song, L.; Jin, C. H.; Jariwala, D.; Wu, D. X.; Li, Y. J.; Srivastava, A.; Wang, Z. F.; Storr, K.; Balicas, L.; Liu, F.; Ajayan, P. M. Atomic Layers of Hybridized Boron Nitride and Graphene Domains. *Nat. Mater.* **2010**, *9*, 430-435.

190. Nicolosi, V.; Chhowalla, M.; Kanatzidis, M. G.; Strano, M. S.; Coleman, J. N. Liquid Exfoliation of Layered Materials. *Science* **2013**, *340*, 1420-+.

191. Jeon, I. Y.; Shin, Y. R.; Sohn, G. J.; Choi, H. J.; Bae, S. Y.; Mahmood, J.; Jung, S. M.; Seo, J. M.; Kim, M. J.; Chang, D. W.; Dai, L. M.; Baek, J. B. Edge-Carboxylated Graphene Nanosheets Via Ball Milling. *Proc. Natl. Acad. Sci. U.S.A.* **2012**, *109*, 5588-5593.

192. Jeon, I.-Y.; Choi, H.-J.; Jung, S.-M.; Seo, J.-M.; Kim, M.-J.; Dai, L.; Baek, J.-B. Large-Scale Production of Edge-Selectively Functionalized Graphene Nanoplatelets Via Ball Milling and Their Use as Metal-Free Electrocatalysts for Oxygen Reduction Reaction. *J. Am. Chem. Soc.* **2012**, *135*, 1386-1393.

193. Frey, G. L.; Reynolds, K. J.; Friend, R. H.; Cohen, H.; Feldman, Y. Solution-Processed Anodes from Layer-Structure Materials for High-Efficiency Polymer Light-Emitting Diodes. *J. Am. Chem. Soc.* **2003**, *125*, 5998-6007.

194. Quintana, M.; Grzelczak, M.; Spyrou, K.; Kooi, B.; Bals, S.; Van Tendeloo, G.; Rudolf, P.; Prato, M. Production of Large Graphene Sheets by Exfoliation of Graphite under High Power Ultrasound in the Presence of Tiopronin. *Chem. Commun.* **2012**, *48*, 12159-12161.

195. Thurston, T. R.; Wilcoxon, J. P. Photooxidation of Organic Chemicals Catalyzed by Nanoscale Mos2. *J. Phys. Chem. B* **1999**, *103*, 11-17.

196. Shaffei, K. A.; Ayoub, M. M. H.; Ismail, M. N.; Badran, A. S. Kinetics and Polymerization Characteristics for Some Polyvinyl Acetate Emulsions Prepared by Different Redox Pair Initiation Systems. *Eur. Polym. J.* **1998**, *34*, 553-556.

197. Ershov, S.; Khelifa, F.; Dubois, P.; Snyders, R. Derivatization of Free Radicals in an Isopropanol Plasma Polymer Film: The First Step toward Polymer Grafting. *ACS Applied Materials & Interfaces* **2013**, *5*, 4216-4223.

198. Tauber, A.; Mark, G.; Schuchmann, H.-P.; von Sonntag, C. Sonolysis of Tert-Butyl Alcohol in Aqueous Solution. *J. Chem. Soc., Perkin Trans. 2* **1999**, *0*, 1129-1136.

199. Kranenburg, M.; Ciriano, M. V.; Cherkasov, A.; Mulder, P. Carbon−Oxygen Bond Dissociation Enthalpies in Peroxyl Radicals. *The Journal of Physical Chemistry A* **2000**, *104*, 915-921.

200. Barnard, J. A. The Pyrolysis of Isopropanol. *Trans. Faraday Soc.* **1960**, *56*, 72-79.

201. Ge, P.; Scanlon, M. D.; Peljo, P.; Bian, X.; Vubrel, H.; O'Neill, A.; Coleman, J. N.; Cantoni, M.; Hu, X.; Kontturi, K.; Liu, B.; Girault, H. H. Hydrogen Evolution across Nano-Schottky Junctions at Carbon Supported Mos2 Catalysts in Biphasic Liquid Systems. *Chem. Commun.* **2012**, *48*, 6484-6486.

202. Sheldon, R. A.; Arends, I.; Ten Brink, G. J.; Dijksman, A. Green, Catalytic Oxidations of Alcohols. *Acc. Chem. Res.* **2002**, *35*, 774-781.

203. Eda, G.; Yamaguchi, H.; Voiry, D.; Fujita, T.; Chen, M.; Chhowalla, M. Photoluminescence from Chemically Exfoliated Mos2. *Nano Lett.* **2011**, *11*, 5111-5116.

204. Delporte, P.; Meunier, F.; Phamhuu, C.; Vennegues, P.; Ledoux, M. J.; Guille, J. Physical Characterization of Molybdenum Oxycarbide Catalyst - Tem, Xrd and Xps. *Catal. Today* **1995**, *23*, 251-267.

205. Tsyganenko, A. A.; Can, F.; Travert, A.; Mauge, F. Ftir Study of Unsupported Molybdenum Sulfide - in Situ Synthesis and Surface Properties Characterization. *Appl. Catal., A* **2004**, *268*, 189-197.

206. Weber, T.; Muijsers, J. C.; vanWolput, H.; Verhagen, C. P. J.; Niemantsverdriet, J. W. Basic Reaction Steps in the Sulfidation of Crystalline Moo3 to Mos2 as Studied by X-Ray Photoelectron and Infrared Emission Spectroscopy. *J. Phys. Chem.* **1996**, *100*, 14144-14150.

207. Lee, C.; Yan, H.; Brus, L. E.; Heinz, T. F.; Hone, J.; Ryu, S. Anomalous Lattice Vibrations of Single- and Few-Layer Mos2. *ACS Nano* **2010**, *4*, 2695-2700.

208. Frey, G. L.; Tenne, R.; Matthews, M. J.; Dresselhaus, M. S.; Dresselhaus, G. Raman and Resonance Raman Investigation of Mos2 Nanoparticles. *Phys. Rev. B* **1999**, *60*, 2883-2892.

209. Chen, J. M.; Wang, C. S. Second Order Raman Spectrum of Mos2. *Solid State Commun.* **1974**, *14*, 857-860.

210. Yang, D.; Sandoval, S. J.; Divigalpitiya, W. M. R.; Irwin, J. C.; Frindt, R. F. Structure of Single-Molecular-Layer Mos2. *Phys. Rev. B* **1991**, *43*, 12053-12056.

211. Goloveshkin, A. S.; Bushmarinov, I. S.; Lenenko, N. D.; Buzin, M. I.; Golub, A. S.; Antipin, M. Y. Structural Properties and Phase Transition of Exfoliated-Restacked Molybdenum Disulfide. *J. Phys. Chem. C* **2013**, *117*, 8509-8515.

212. Houben, L.; Enyashin, A. N.; Feldman, Y.; Rosentsveig, R.; Stroppa, D. G.; Bar-Sadan, M. Diffraction from Disordered Stacking Sequences in Mos2 and Ws2 Fullerenes and Nanotubes. *J. Phys. Chem. C* **2012**, *116*, 24350-24357.

213. Ramakrishna Matte, H. S. S.; Gomathi, A.; Manna, A. K.; Late, D. J.; Datta, R.; Pati, S. K.; Rao, C. N. R. Mos2 and Ws2 Analogues of Graphene. *Angew. Chem. Int. Ed.* **2010**, *49*, 4059-4062.

214. Joensen, P.; Crozier, E. D.; Alberding, N.; Frindt, R. F. A Study of Single-Layer and Restacked Mos2 by X-Ray-Diffraction and X-Ray Absorption-Spectroscopy. *J. Phys. C: Solid State Phys.* **1987**, *20*, 4043-4053.

215. Berdinsky, A. S.; Chadderton, L. T.; Yoo, J. B.; Gutakovsky, A. K.; Fedorov, V. E.; Mazalov, L. N.; Fink, D. Structural Changes of Mos2 Nano-Powder in Dependence on the Annealing Temperature. *Applied Physics a-Materials Science & Processing* **2005**, *80*, 61-67.

216. Li, X. L.; Li, Y. D. Formation Mos2 Inorganic Fullerenes (Ifs) by the Reaction of Moo3 Nanobelts and S. *Chem. Eur. J.* **2003**, *9*, 2726-2731.

217. Krasheninnikov, A. V.; Banhart, F. Engineering of Nanostructured Carbon Materials with Electron or Ion Beams. *Nat. Mater.* **2007**, *6*, 723-733.

218. Isshiki, T.; Nishio, K.; Saijo, H.; Shiojiri, M.; Yabuuchi, Y.; Takahashi, N. High-Resolution Transmission Electron-Microscopy of Hexagonal and Rhombohedral Molybdenum-Disulfide Crystals. *Microsc. Res. Tech.* **1993**, *25*, 325-334.

219. Brivio, J.; Alexander, D. T. L.; Kis, A. Ripples and Layers in Ultrathin Mos2 Membranes. *Nano Lett.* **2011**, *11*, 5148-5153.

220. Balendhran, S.; Deng, J.; Ou, J. Z.; Walia, S.; Scott, J.; Tang, J.; Wang, K. L.; Field, M. R.; Russo, S.; Zhuiykov, S.; Strano, M. S.; Medhekar, N.; Sriram, S.; Bhaskaran, M.; Kalantar-zadeh, K. Enhanced Charge Carrier Mobility in Two-Dimensional High Dielectric Molybdenum Oxide. *Adv. Mater.* **2013**, *25*, 109-114.

221. Fivaz, R.; Mooser, E. Mobility of Charge Carriers in Semiconducting Layer Structures. *Phys. Rev.* **1967**, *163*, 743-755.

222. Kremer, F.; Schonhals, A. *Broadband Dielectric Spectroscopy*. Springer: Berlin, 2003.

223. Cataldo, F. A Study on the Thermal Stability to 1000°C of Various Carbon Allotropes and Carbonaceous Matter Both under Nitrogen and in Air. *Fullerenes, Nanotubes and Carbon Nanostructures* **2002**, *10*, 293-311.

224. Zhao, Y.; Wu, X.; Yang, J.; Zeng, X. C. Oxidation of a Two-Dimensional Hexagonal Boron Nitride Monolayer: A First-Principles Study. *PCCP* **2012**, *14*, 5545-5550.

225. Quinlan, R. A.; Cai, M.; Outlaw, R. A.; Butler, S. M.; Miller, J. R.; Mansour, A. N. Investigation of Defects Generated in Vertically Oriented Graphene. *Carbon* **2013**, *64*, 92-100.

226. Park, S.; Ruoff, R. S. Chemical Methods for the Production of Graphenes. *Nature Nanotechnology* **2009**, *4*, 217-224.

227. Wilcoxon, J. P.; Newcomer, P. P.; Samara, G. A. Synthesis and Optical Properties of Mos2 and Isomorphous Nanoclusters in the Quantum Confinement Regime. *J. Appl. Phys.* **1997**, *81*, 7934-7944.

228. Eda, G.; Fujita, T.; Yamaguchi, H.; Voiry, D.; Chen, M.; Chhowalla, M. Coherent Atomic and Electronic Heterostructures of Single-Layer Mos2. *ACS Nano* **2012**, *6*, 7311-7317.

229. Radisavljevic, B.; Radenovic, A.; Brivio, J.; Giacometti, V.; Kis, A. Single-Layer Mos2 Transistors. *Nat. Nanotech.* **2011**, *6*, 147-150.

230. Nicolosi, V.; Vrbanic, D.; Mrzel, A.; McCauley, J.; O'Flaherty, S.; McGuinness, C.; Compagnini, G.; Mihailovic, D.; Blau, W. J.; Coleman, J. N. Solubility of Mo6s4.5i4.5 Nanowires in Common Solvents: A Sedimentation Study. *J. Phys. Chem. B* **2005**, *109*, 7124-33.

231. Finn, D. J.; Lotya, M.; Cunningham, G.; Smith, R. J.; McCloskey, D.; Donegan, J. F.; Coleman, J. N. Inkjet Deposition of Liquid-Exfoliated Graphene and Mos2 Nanosheets for Printed Device Applications. *Journal of Materials Chemistry C* **2014**, *2*, 925-932.

232. Gordon, R. A.; Yang, D.; Crozier, E. D.; Jiang, D. T.; Frindt, R. F. Structures of Exfoliated Single Layers of Ws2, Mos2, and Mose2 in Aqueous Suspension. *Phys. Rev. B* **2002**, *65*.

233. Quinn, M. D. J.; Ngoc Han, H.; Notley, S. M. Aqueous Dispersions of Exfoliated Molybdenum Disulfide for Use in Visible-Light Photocatalysis. *ACS Applied Materials & Interfaces* **2013**, *5*, 12751-12756.

234. Lotya, M.; Rakovich, A.; Donegan, J. F.; Coleman, J. N. Measuring the Lateral Size of Liquid-Exfoliated Nanosheets with Dynamic Light Scattering. *Nanotechnology* **2013**, *24*.

235. Notley, S. M. High Yield Production of Photoluminescent Tungsten Disulphide Nanoparticles. *J. Colloid Interface Sci.* **2013**, *396*, 160-164.

236. Xu, B. H.; Lin, B. Z.; Chen, Z. J.; Li, X. L.; Wang, Q. Q. Preparation and Electrical Conductivity of Polypyrrole/Ws2 Layered Nanocomposites. *J. Colloid Interface Sci.* **2009**, *330*, 220-226.

237. Li, T. S.; Galli, G. L. Electronic Properties of Mos2 Nanoparticles. *J. Phys. Chem. C* **2007**, *111*, 16192-16196.

238. Stengl, V.; Henych, J. Strongly Luminescent Monolayered Mos2 Prepared by Effective Ultrasound Exfoliation. *Nanoscale* **2013**, *5*, 3387-3394.

239. Yu, W. W.; Chang, E.; Falkner, J. C.; Zhang, J. Y.; Al-Somali, A. M.; Sayes, C. M.; Johns, J.; Drezek, R.; Colvin, V. L. Forming Biocompatible and Nonaggregated Nanocrystals in Water Using Amphiphilic Polymers. *J. Am. Chem. Soc.* **2007**, *129*, 2871-2879.

240. May, P.; Khan, U.; Hughes, J. M.; Coleman, J. N. Role of Solubility Parameters in Understanding the Steric Stabilization of Exfoliated Two-

Dimensional Nanosheets by Adsorbed Polymers. *J. Phys. Chem. C* **2012**, *116*, 11393-11400.

241. Ozdemir, C.; Guner, A. Solubility Profiles of Poly(Ethylene Glycol)/Solvent Systems, I: Qualitative Comparison of Solubility Parameter Approaches. *Eur. Polym. J.* **2007**, *43*, 3068-3093.

242. Kawakami, M.; Egashira, M.; Kagawa, S. Measurements of Interactions between Polyethylene-Glycol and Organic-Compounds by Gas-Chromatographic Technique. *Bull. Chem. Soc. Jpn.* **1976**, *49*, 3449-3453.

243. Zhang, Y.; Gu, S.; Yan, B.; Ren, J. Solvent-Free Ionic Molybdenum Disulphide (Mos2) Nanofluids. *J. Mater. Chem.* **2012**, *22*, 14843-14846.

VITA

Vikram Kumar Srivastava was born on October 28th, 1986 in Dalton, Georgia. In May 2005, he graduated from Baylor School (Chattanooga, TN) and attended Emory University (Atlanta, GA). In May 2009, he graduated with a Bachelor's of Science in Chemistry, and the following July began his graduate school career specializing in Polymer Chemistry under the direction of Professor Jimmy W. Mays. On March 21st, 2014, he successfully defended his dissertation.